Mechanistic Insight into Next Generation Batteries
The Story of Li-oxygen and Zn-aqueous Batteries

Li, Zhaolong

DOI

Publication date
2019

Document Version
Final published version

Citation (APA)

Important note
To cite this publication, please use the final published version (if applicable).
Please check the document version above.

Mechanistic Insight into Next Generation Batteries

The Story of Li-oxygen and Zn-aqueous Batteries

Mechanistic Insight into Next Generation Batteries

Zhaolong Li

Zhaolong LI

李兆龙

TU Delft
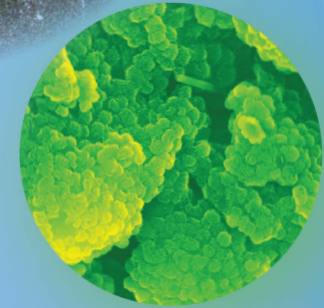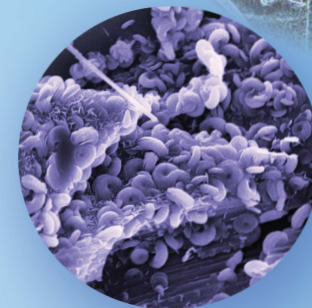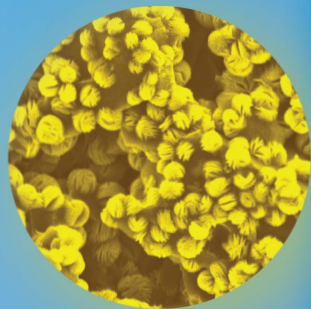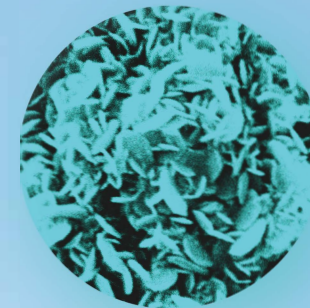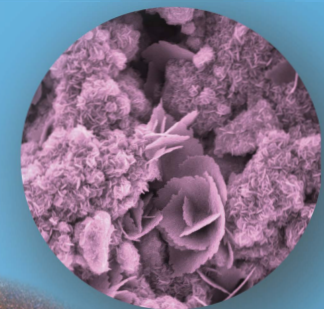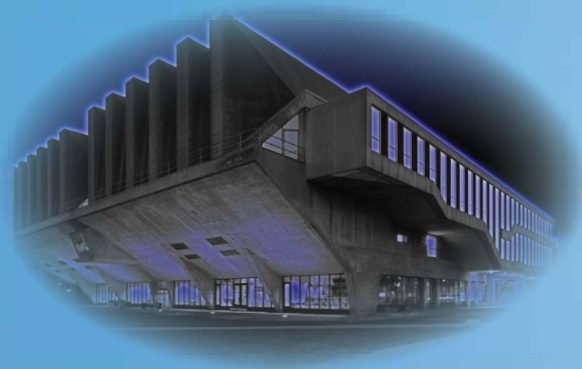
Propositions

Accompanying the dissertation titled

Mechanistic Insight into Next Generation Batteries:

The Story of Li-oxygen and Zn-aqueous Batteries

By

Zhaolong Li

1. Li-O_2 batteries will never achieve a practical volumetric energy density larger than that of Li-ion batteries.

2. The intrinsic properties of Li_2O_2 are responsible for the promise, but also for the failure of Li-O_2 batteries.

3. Aqueous batteries will replace stationary Li-ion batteries.

4. Charge balancing proton insertion/extraction reactions in aqueous batteries provides a route to high performance safe and cheap aqueous batteries.

5. The use of high-tech instrumentation for research creates Scientific Monopolies.

6. The success of future batteries requires that battery researchers develop a stronger environmental conscience.

7. Battery research should focus more on solving problems in existing batteries, rather than focussing on inventing new batteries.

8. Blue-sky thinking will lead to failure for most PhD students.

9. Two essential ingredients for a successful PhD are to recognize that there is more to life than your PhD and that you should repeat experiments.

10. A PhD should teach you to question yourself and your observations.

These propositions are considered as opposable and defendable, and have been approved as such by promotors Prof.dr.ir. M. Wagemaker, Prof. dr. F.M. Mulder and daily supervisor Dr. S. Ganapathy

Mechanistic Insight into Next Generation Batteries

The Story of Li-oxygen and Zn-aqueous Batteries

Dissertation

for the purpose of obtaining the degree of doctor

at Delft University of Technology

by the authority of the Rector Magnificus, Prof.dr.ir. T.H.J.J. van der Hagen,

chair of the Board for Doctorates

to be defended publicly on

Monday 23 September 2019 at 15:00 o'clock

by

Zhaolong Li

Master of Engineering in Composite Materials,

Wuhan University of Technology, China

born in Hubei, China

This dissertation has been approved by the promotors.

Composition of the doctoral committee:

Rector Magnificus	chairperson
Prof.dr.ir. M. Wagemaker	Delft University of Technology, promotor
Prof.dr. F.M. Mulder	Delft University of Technology, copromotor

……………………………………………………..

Independent members:

Prof.dr. Y.-S. Hu	Chinese Academy of Sciences, China
Prof.dr. M. Tromp	University of Groningen, the Netherlands
Prof.dr. M. Creatore	Eindhoven University of Technology, the Netherlands
Prof.dr. B. Dam	Delft University of Technology, the Netherlands
Dr. E.M. Kelder	Delft University of Technology, the Netherlands

To my family

Contents

Chapter 1 Introduction

(Image source: https://www.klimaatakkoord.nl/elektriciteit)

The renewable energy power sources become more dependent on the changeable weather and diurnal cycles, which need the reusable energy conversion devices smoothing the supply of energy reliable.

1.1 Rechargeable batteries for a sustainable energy future

The human energy consumption has led to global climate change and environmental pollution, caused by the emission of greenhouse gasses. To develop towards sustainable society, it is essential to move forward the use of renewable energy instead of fossil fuels. However, clean energy sources, such as solar, wind, hydro energy, etc. fluctuate over time with the changes in weather, the diurnal cycles, seasons, and geographic distribution.[1] To eliminate the intermittency of this renewable energy production, it is essential to employ low-cost and reusable electrical energy storage (EES) technologies as intermediary devices, allowing energy to be stored intermittently until they are required.[2,3] In addition, with the growing demand of EES devices for the rapidly develop of portable electronic product, in particular the urgent market for the electric vehicles (EV) as an alternative of fossil fuel powered transportation. The research of rechargeable batteries plays an important role in the sustainable future. Among the variety of EES technologies, rechargeable batteries, especially lithium-ion batteries (LIBs) represent excellent electricity storage devices for the integration of variety renewable electricity resources.[4]

1.2 The choice of Li-O$_2$ batteries

Typically, the battery system we use consists of several electrochemical units connected in series and/or in parallel to supply the designed voltage and capacity, respectively for different electric applications. A single battery electrochemical cell consists of a positive and negative electrode that are electronically insulated by a separator that is filled by an electrolyte solution containing dissociated salts, which is able to transfer the active ions between the two electrodes. The electrons flow through an external circuit (**Figure 1.1**). The amount of electrical energy delivered by the batteries is associated directly with the difference in electrode potentials and their charge storage capacities, which are dependent on the electrochemical reactions between the active ions and the electrodes. Hundreds of potential battery systems based on the electrochemical reaction couples have been proposed during the past centuries, leading to the most common secondary battery chemistries which are lead-acid and Ni-Cd batteries. However, their energy density is limited by the nature of the electrochemical reaction with its limited low voltage and some irreversible reactions. In 1991, the LIBs were first commercialized by Sony by using a graphite anode and a layered-oxide (LiCoO$_2$) cathode. The energy stored in this battery is about 180 Wh/kg at which is five times higher than that stored by lead-acid batteries (**Figure 1.1**), which led to a revolution in portable electric deveces.[5]
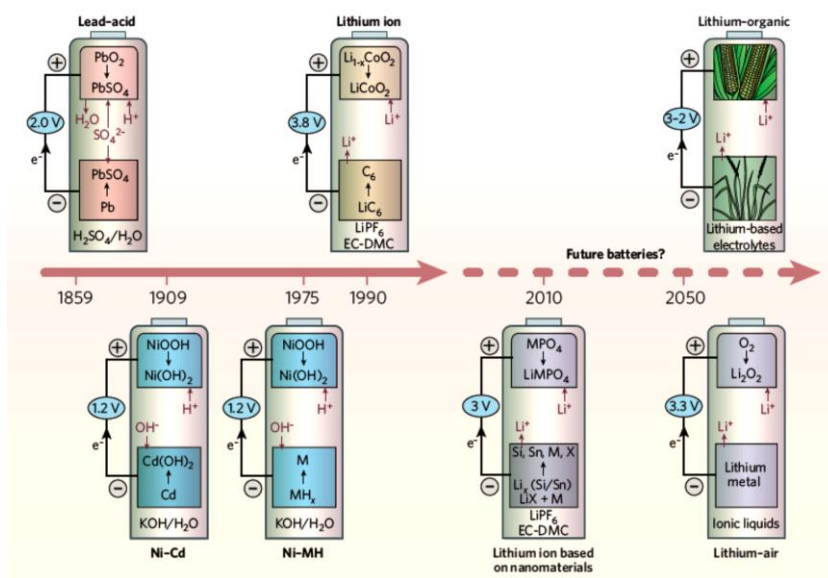
Figure 1.1. Battery chemistry history. Present-day battery technologies are being outpaced by the ever-increasing power demands from new applications. As well as being inherently safe, batteries of the future will have to integrate the concept of environmental sustainability.[5] Copyright 2008, Springer Nature.

However, LIBs based on graphite anodes and layered oxide cathodes have been reaching their maximum energy density, as limited by the intercalation chemistry.[7-9] This has motivated the ambitious push towards battery systems which operate 'beyond-intercalation chemistries'. One of the promising candidates is Li-O_2 batteries, which would potentially deliver a gravimetric energy density 3-4 times higher than the lithium-ion batteries. This is based on the abundance of oxygen gas outside of the battery, which is therefore sourced from atmosphere, and the high capacity of lithium metal, whereby oxygen is reduced to form lithium peroxide (Li$_2$O$_2$) ($2Li + O_2 \leftrightarrow Li_2O_2, 2.96\ V\ vs.\ Li/Li^+$).[10] Currently, four types of Li-O_2 batteries are being researched based on different electrolytes: aprotic (non-aqueous), aqueous, hybrid, and solid-state Li-O_2 batteries,[11] among which the aprotic Li-O_2 battery system has been the most intensively investigated (**Figure 1.2a**), and is a major topic of this thesis. The first successfully discharged Li-O_2 battery was developed by Abraham *et al.* in 1996,[12] and despite a slow start, rechargeability of Li-O_2 batteries has been demonstrated over the last ten years.[8,10,13,14] Typically, a rechargeable Li-O_2 battery contains Li metal as the anode, a porous conductive membrane containing carbon combined with a catalyst as the O_2-breathing cathode, and an electrolyte in the middle,[5] as shown in **Figure 1.2a**. In an aprotic electrolyte, on discharge the reaction process at the Li anode is relatively facile during discharge ($Li \rightarrow Li^+ + e^-$), while at the cathode the practical potential deviates from the

thermodynamic potential of the reaction. In an ideal reaction, only insoluble Li_2O_2 is formed on the cathode on discharge, progressing *via* the surface or solution mechanism, which is decided by parameters such as the overpotential, current density and the Gutmann donor number (DN) of the electrolyte (**Figure 1.2b**).[15-19] On charge, the Li_2O_2 will be electrochemically oxidized to Li^+ and O_2 on the cathode surface, the success of which is highly dependent on the Li_2O_2 morphology (amorphous/crystalline or defects) formed during discharge. In addition, other factors may influence the reversibility of the Li_2O_2 and cathode reaction, such as the deposition of parasitic products (Li_2CO_3, $LiOH$, etc.) from the electrolyte, oxygen species and electrode degradation. Although these complex reactions have been widely explored, a number of fundamental questions remain to be addressed. This is of the utmost significance to anticipate whether or not $Li-O_2$ batteries will be able to achieve practical capabilities and cycleability beyond current Li-ion batteries.
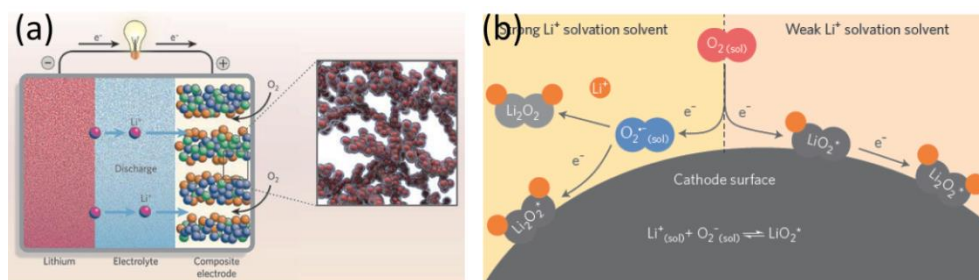
Figure 1.2. (a) A typical aprotic $Li-O_2$ battery component using Li metal as the anode and a porous cathode composed of large surface area carbon particles and catalyst particles, and an organic electrolyte consisting of dissolved lithium salt.[5] Copyright 2008, Springer Nature (b) Reduction mechanisms in a $Li-O_2$ battery at low overpotentials.[15] Copyright 2016, Springer Nature.

1.3 Understanding the basic electrochemical reaction in a $Li-O_2$ battery

1.3.1 O_2 reduction to Li_2O_2 on discharge

Recent research studying the mechanism of $Li-O_2$ batteries has provided increasing insight in how the Li_2O_2 product forms when reducing O_2 on discharge.[15,17,18] The formation of Li_2O_2 during discharge is strongly related to some competitive factors involving the effective current density and overpotential[20] and the solubility of LiO_2 intermediate in the electrolyte or absorption on the cathode surface[17]. Generally, the O_2 reduction process follows either a solution mechanism or surface mechanism (**Figure 1.2b**).[15]

As concluded from equations (1)-(4), the first step of the O_2 reduction reaction is an one-electron reduction to form LiO_2, either dissolved in the solution or absorbed on the

electrode surface. This process is governed by the competition between the LiO_2 solubility (**equation 1**) and the adsorption free energy of LiO_2* on the electrode (**equation 3**), which depends primarily on Gutmann donor number (DN) of the electrolyte describe as the solvation capability of the solvent molecules and the ionic dissociation strength.[19,21,22] If a solvent has a high DN to strongly solvate Li^+, then LiO_2 mainly dissolves in the electrolyte, which is followed by a disproportion reaction to generate micrometre-sized Li_2O_2 particles deposited on the electrode surface (**equation 2**).[17,23] On the other hand, low solvation energy leads to dominate LiO_2 deposition on the electrode surface, where it possesses a second electron reduction to form a Li_2O_2 film (**equation 4**).[15,17,23] In this process, the insulating Li_2O_2 film can only grow to 6-7 nm clogging the electrode surface, resulting in electrode passivation and leading to low capacities, low rates and early battery death.[24] In contrast, in high DN-solvents, the dominance of larger Li_2O_2 particles growth in solution leads to higher discharge capacities and relatively high rates.[17,25] However, the existing of the reduced oxygen radical (O_2^-) in the electrolyte, being strongly nucleophilic, attacks the carbon atoms of the solvent molecules or causes H-abstraction, hence resulting in parasitic reactions.[7,26,27] To avoid this, one strategy is to design a balanced porous cathode for Li-O_2 batteries, away from really high surface areas but with a high proportion of large pores to quickly store the Li_2O_2 particles during discharge.[15] Another approach is to find a low-DN solvent (weakly solvating) with additives in the electrolyte which form Li_2O_2 in solution to avoid the surface formation of LiO_2 and its disadvantages in order to achieve a high discharge capacity and rate.[18]

Solution mechanism:

$$Li^+ + O_2 + e^- \rightarrow Li^+_{(sol)} + O^-_{2\,(sol)} \tag{1}$$

$$2\left(Li^+_{(sol)} + O^-_{2\,(sol)}\right) \rightarrow Li_2O_2 \downarrow + O_2 \; or \; 2Li^+_{(sol)} + O^-_{2\,(sol)} + e^- \rightarrow Li_2O_2 \downarrow \tag{2}$$

Surface mechanism:

$$Li^+ + O_2 + e^- \rightarrow LiO_2^*; absorbed \; on \; the \; cathode \tag{3}$$

$$LiO_2^* + Li^+ + e^- \rightarrow Li_2O_2^* \; \; or \; \; 2LiO_2^* \rightarrow Li_2O_2^* + O_2 \tag{4}$$
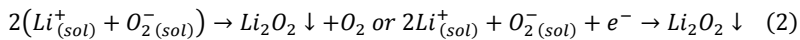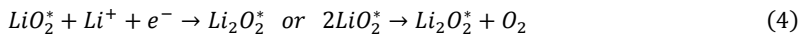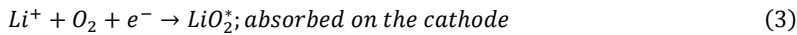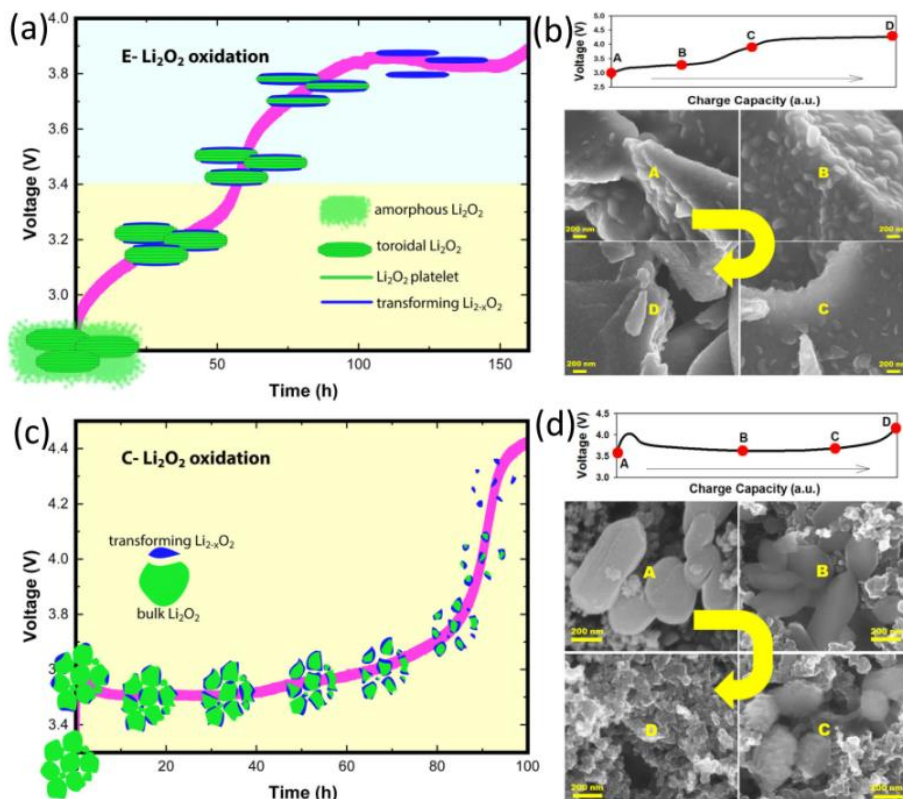
Figure 1.3. Schematic of the Li_2O_2 ((a) electrochemical formed in $Li-O_2$ batteries, E-Li_2O_2, and (c) commercial, C-Li_2O_2 and) oxidation mechanism during charge. (b) and (d) Scanning electron microscopy images (SEM) observed E-Li_2O_2 and C-Li_2O_2 morphology at different oxidation stages, respectively. The yellow arrows indicate increasing state of charge.[28] Reprinted with permission from ref. 28. Copyright 2014, American Chemical Society.

1.3.2 Li_2O_2 oxidation to O_2 on charge

The charging process of $Li-O_2$ batteries is related to the electrochemical oxidation of Li_2O_2 which is formed on the cathode surface during discharge. Typically, the voltage profile at the onset of charging (O_2 evolution) is slightly above the OCV at ~ 3.0 V as charging progresses.[7] Important factors that influence the charge potential are: (1) electrochemical oxidation part of the Li_2O_2 is possible at a low overpotential and a low rate; (2) the electron transfer upon charge becomes increasingly difficult because of the resistive properties of Li_2O_2 contributing to the voltage rise; (3) the largest contribution to the rising voltage is due to the accumulation of parasitic products that hinder the charge transfer.[9,20,24,29]
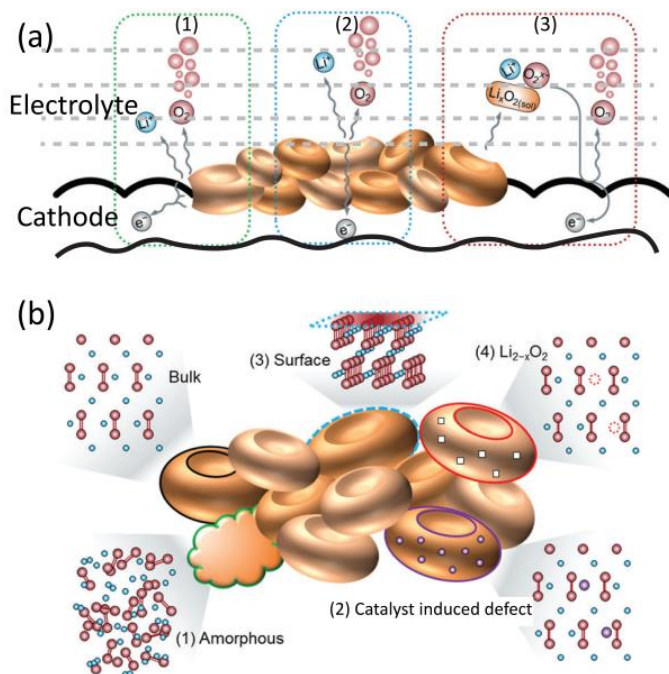
Figure 1.4. Schematic of the possible Li_2O_2 decomposition process from various Li_2O_2 structures. (a) Three possible reaction routes for electrochemical oxidation of Li_2O_2 distinguished as electrode/Li_2O_2, Li_2O_2/electrolyte, and electrode/electrolyte interface processes. (b) Four types of Li_2O_2 structure on the electrode surface representing four possible mechanisms for Li_2O_2 oxidation on charge.[7] Copyright 2017, Royal Society of Chemistry.

Studies of electrodes pre-loaded with crystalline Li_2O_2 (C-Li_2O_2) on charging of the Li-O_2 battery demonstrates that the surface chemistry of the cathode and electrolyte is crucial in determining the electron transfer efficiency through the insulating Li_2O_2, and also elucidated the role of passivating film formed on the electrode surface, which can either closure or facilitate charging.[15] Experimentally (**Figure 1.3c**), the charge profile of the C-Li_2O_2 on the cathode mainly exhibits a low voltage plateau (up to 90% of the total oxidation process at the voltage of 3.5 V vs. Li^+/Li),[28]. However, the charge profile of Li_2O_2 (E-Li_2O_2) formed electrochemically in Li-O_2 batteries only shows a low voltage at early stages of charge (~35% of the total oxidation process at the voltage below 3.5 V *vs.* Li^+/Li) and then the charge voltage plateau dramatically increases to 3.9 V (**Figure 1.3a**).[28] In contrast to C-Li_2O_2, the E-Li_2O_2 may be comprised of both Li_2O_2 and parasitic products arising from electrolyte degradation, probably accounting for the less than 100% yield of peroxide. During charge, the amorphous Li_2O_2 is removed first and the crystalline Li_2O_2 is proposed to decompose *via* the Li-deficient solid solution ($Li_{2-x}O_2$) at high potentials (**Figure 1.3a and b**). For C-Li_2O_2, the small actively oxidizing fraction results in a gradual

reduction of the Li_2O_2 crystallites from bulk to $Li_{2-x}O_2$ until their complete disappearance (**Figure 1.3c and d**). Even though the oxygen release mechanism is not clear on the charge of Li_2O_2, it is probable that $Li_{2-x}O_2$ can undergo disproportionation leading to O_2 evolution. Simulations indicate that, the O_2 evolution during the Li_2O_2 oxidation process occurs at many crystal facets with a low overpotenital (<0.2 V), which fits the experiment results very well.[30]

Three possible mechanisms for the oxidation Li_2O_2 to release O_2 have been proposed as shown in **Figure 1.4a**.[7] (1) The Li_2O_2 decomposition occurs at the electrode/Li_2O_2/electrolyte triple point, where Li ions and oxygen gas can be easily released from the Li_2O_2 surface into electrolyte and the e^- into the current collector (**Figure 1.4a**, route 1). (2) The Li-ions are released from the Li_2O_2/electrolyte interface, relying on electrons transport through the Li_2O_2 particles (**Figure 1.4a**, route 2). (3) Unlike the direct oxidation of Li_2O_2, the formed $Li_{2-x}O_2$ or Li^+-$O_2^{-/2-}$ ions pairs are dissolved from the Li_2O_2 into the electrolyte, which are electrochemically decomposed at the electrolyte/electrode interface to release the O_2 in the electrolyte and the electrons are transferred on the electrode surface (**Figure 1.4c**, route 3). However, because of the unfavourable dissolution energy of Li_2O_2 to produce $Li_{2-x}O_2$ or Li^+-$O_2^{-/2-}$ ions, route 3 is believed to be less dominant.[7]

The structure of the electrochemically formed Li_2O_2 may possess several defects, which also affects the oxidation behaviour and charge transport of Li_2O_2 on charge. Several studies have reported that the defect in Li_2O_2 could increase the conductivity of Li_2O_2. As shown in **Figure 1.4b**, four different defect scenarios may appear in electrochemically formed Li_2O_2. The amorphous Li_2O_2 phase (**Figure 1.4b** (1)) has been observed experimentally,[20,31] which has a higher ionic and electronic conductivity compared to crystalline Li_2O_2.[32] Defects in Li_2O_2 can be induced to form when a metal oxide catalyst contact with a Li_2O_2 particles (**Figure 1.4b** (2)).[33] The surfaces of the Li_2O_2 can possess metallic characteristics due to the presence of defects (**Figure 1.4b** (3)),[30,34] which implies that reducing the size of the discharge product, thereby increasing the surface area, may promote the charge transport kinetics in Li-O_2 batteries. Lithium deficient, $Li_{2-x}O_2$ (**Figure 1.4b** (4)) appears the most frequently observed type of defect in electrochemically formed Li_2O_2 on discharge and charge, which appears to facilitate the release of Li^+ ions and O_2 from solid Li_2O_2.[28,35] In conclusion, the presence of various type of defects in Li_2O_2 appear to have significant influence on the charge transport properties of Li_2O_2, and are thus important factors to consider in the decomposition reaction in Li-O_2 batteries.[36]

1.3.3 Parasitic reactions in Li-O₂ batteries

The electrochemical performance in a aprotic Li-O$_2$ battery depends on the reversible reaction at the electrode, $Li^+ + O_2 + e^- \leftrightarrow \frac{1}{2}Li_2O_2$. However, due to the highly reactive oxygen radical (O$_2^-$) generated during the discharge process, the cathode surface is typically clogged by products including Li$_2$CO$_3$, LiOH, Li-formate and Li-acetate resulting from competitive parasitic reactions.[7,9,15] These side products originate from the degradation of the electrolyte *via* the nucleophilic attack of the O$_2^-$ on the carbon atom of the solvent molecule or H-abstraction. These parasitic chemistries are also considered the prime obstacle towards stable reversible cycling of Li-O$_2$ batteries.

During the early development of Li-O$_2$ batteries, the search was on for an electrolyte stable against the nucleophilic attack from the O$_2^-$ species. Studies have revealed that acid-based electrolytes (ether-, sulfone-, and amide-; written as HA) are more stable compared to the carbonate based electrolytes, and have succeeded in predominantly yielding Li$_2$O$_2$.[7] However, even these so called stable electrolytes still participate in degradation reactions *via* the H-abstraction reaction between O$_2^-$ and the hydrogen atom in the solvent molecule, $HA + O_2^- \rightarrow A^- + HO_2$. The generation of HO$_2$ from HA eventually results in the formation of LiOH and Li-formate side products. This type of parasitic reactivity is highly related to the acidity of the acid-based solvent and the concentration of the O$_2^-$ in the electrolyte solution. It was found that a solvent molecule with weak acidity could strongly resist H-abstraction by oxygen radicals[7] The concentration of O$_2^-$ radicals can be affected by the solvating capability of the solvent in the electrolyte, which can be described by its donor number (DN) and acceptor number (AN). A solvent with low DN and AN can possesses a low concentration of O$_2^-$, possibly suppressing H-abstraction.[23] For instance, dimethoxyethane (DME) is reported, with strong acidity and low DN and AN properties, to be stable against oxygen radicals for over one week.[37,38] Nevertheless, as needed for the long cycling of Li-O$_2$ batteries, the search is on to find a stable electrolyte avoiding the generation of by-products which still remains a challenge.

1.3.4 Catalysts in Li-O₂ batteries

Typically, electrocatalysts in Li-O$_2$ batteries can be classified as soluble catalysts added to the electrolyte solution and solid catalysts added in the electrode. They can be further classified as oxygen reduction (ORR) catalysts and oxygen oxidation (OER) catalysts based on the role they perform during discharge and charge, respectively. As described previously, a solution mechanism for the formation of Li$_2$O$_2$ could improve the discharge performance of Li-O$_2$ batteries even in low DN electrolytes. Another approach is a redox

mediator (RM) as a soluble additive in the electrolyte, i.e. DBBQ added to a DME based electrolyte, resulting in an 80-fold increase of capacity compared to DME without DBBQ additive.[18] The solid catalysts added to the electrode usually aid against the decomposition of the organic electrolyte to build up a stable interface for Li_2O_2 deposition. Mostly, the use of solid catalysts is aimed at decreasing the charge overpotetial avoiding a high charge voltage, and thereby preventing side reaction between electrolyte and carbon cathode. On a conventional carbon based gas diffusion electrode, the large overpotential on charge induces further electrolyte decomposition and passivates the active oxygen cathode interface, depositing highly insulating Li_2CO_3 on the electrode surface, which increases the charge overpotential even further compromising the reversibility of the Li-O$_2$ batteries. Thus, the reduction of the charge overpotential is a key step in the further development of Li-O$_2$ batteries, allowing a higher efficiency and a better cycling stability. However, ideal Li_2O_2 oxidation during the OER does not involve O-O bond breaking, making the application of solid catalyst on charge ambiguous.

Whether solid catalysts have any effect on charge depends on the processes at the buried cathode/Li_2O_2 interface, which is still largely unclear. For example (as depicted in **Figure 1.4b**), the *in-situ* doping of the deposited Li_2O_2 with slightly soluble transition metal catalysts during discharge, promotes charging through enhanced polaron transport or vacancy transport with O$_2$ evolution at the Li_2O_2/electrolyte interface.[33,39] It is believed that when a metal or transition metal oxide is used in an oxygen diffusion electrode, it will introduce a stable Li_2O_2 deposition substrate and prevent side reactions leading to the improvement of battery performance. Peng Z. *et al.* have explored an Au porous electrode as the oxygen cathode in an aprotic Li-O$_2$ battery, demonstrating impressive performance, forming highly reversible Li_2O_2 upon cycling at lower charge voltage and displaying faster kinetics, but the electrocatalysis mechanism on charge at the Au cathode is unclear.[40] Ru and RuO oxygen cathodes have also frequently been reported to demonstrate extraordinary ability to reduce the charge overpotential during OER thereby improving energy efficiency and cycle stability.[41,42] However, the real mechanism behind the improved electrochemical performance has not fully understand yet.

Applying an oxidation soluble redox mediator (RM) is another way to effectively reduce charge overpotential of Li-O$_2$ batteries. During charge, the RM first gets oxidized on the oxygen cathode to form an oxidized species (RM$^+$), which then chemically oxidizes the Li_2O_2 to evolve O$_2$. According to this mechanism, the selection of the RM catalyst is based on the ionization energy that catalyst with highest occupied molecular orbital (HOMO) energy levels of the RM that must be suitable for the Li_2O_2 decomposition energy and oxidation potential of the electrolyte solvent.[43] Recent research has found that in the presence of LiI and H_2O additives to the electrolyte, LiOH rather than Li_2O_2 is formed which

can also be cycled electrochemically at lower charge overpotentials.[44] If this decomposition mechanism results in oxygen evolution, it would bring forward a new reversible mechanism, which is however currently under debate as it has been proposed to be thermodynamically unfavourable and it has been suggested that I$^-$ is oxidised rather than LiOH.[45-47]

1.4 The fundamental Li-O$_2$ battery research in this thesis

Summarized in the introduction, the key issue for reversible energy storage in Li-O$_2$ batteries is the efficient Li$_2$O$_2$ generation and decomposition. In these processes, the structure of the cathode, the selection of the electrolyte, the suitable catalyst and RM, and the parasitic product all influence the ORR and OER. Aiming to understand the reaction mechanism in Li-O$_2$ batteries, we developed and applied *operando* X-ray diffraction to explore the structure evolution of Li$_2$O$_2$ with additives in the solution and catalyst on the cathode.

In **Chapter 2**, we report *operando* X-ray diffraction measurements where Rietveld refinement reveals the evolution of the anisotropic crystallite shapes of Li$_2$O$_2$ and LiOH during formation and decomposition. The results demonstrate that Li$_2$O$_2$ forms *via* a nucleation and growth mechanism, whereas the decomposition appears to start at the smallest Li$_2$O$_2$ crystallite sizes due to their larger exposed surfaces. In the presence of LiI, platelet shaped LiOH crystallites form by a particle-by-particle nucleation and growth process and at the end of discharge, H$_2$O depletion results in sub stoichiometric Li(OH)$_{1-x}$, which preferentially decomposes during charge. Thereby, this *operando* study brings forward the impact of the presence of H$_2$O and LiI on the discharge product in Li-O$_2$ batteries.

In **Chapter 3 & 4**, we present a significant and conceptual step forward by controlling the growth of the Li$_2$O$_2$ discharge product by means of NiO (**Chapter 3**) and Fe$_2$O$_3$ (**Chapter 4**) embedded in a carbon matrix, which acts as seed crystal for the reversible Li$_2$O$_2$ growth. This is shown to drastically influence the Li$_2$O$_2$ morphology, both primary and secondary particle shape and size, which is responsible for the improved cycle life. It is especially noteworthy that large reversible capacities are achieved upon potential limited cycling when Fe$_2$O$_3$/CNT materials are used as the cathode in Li-O$_2$ batteries, therefore utilizing the full cathode capacity, unlike all studies using carbon based cathodes up to date. Thereby, a novel, general applicable strategy is introduced providing control over the growth of the discharge products. We believe these fundamental findings are highly relevant to solid state material sciences, as well as being timely, and important for the next generation batteries.

1.5 Rechargeable zinc aqueous batteries

Although Li-ion batteries, with their high energy and power densities, have gained great market penetration, their cost, safety, and longevity are of concern for large-scale applications.[48-50] Aqueous rechargeable batteries are promising alternatives for large-scale applications, which favour low-cost, operational safety, facile manufacture, environmental benignity, and high ionic conductivity based on water electrolytes.[51] Among them, Zn-based aqueous systems are particularly attractive because of their low cost, abundance, low redox potential and high volumetric capacity of zinc.[52]

From the variety of zinc anode based battery systems (Zn-Mn, Ni-Zn, and Zn-air batteries), the alkaline Ni-Zn and Zn-MnO$_2$ batteries are prominent primary battery chemistries.[53] With the advent of rechargeable batteries, they face stiff competition and their use, gradually declines. Efforts were made to develop rechargeable aqueous zinc batteries in alkaline electrolytes.[54] Unfortunately, these attempts were plagued by poor cycle life due to the formation of zinc dendrites and irreversible discharge species in the alkaline electrolyte.[52] In Ni-Zn alkaline batteries, the Zn anode follows a dissolution/precipitation reaction: $Zn + 4OH^- \leftrightarrow Zn(OH)_4^{2-} + 2e^- \leftrightarrow ZnO + 2OH^- + 2H_2O + 2e^-$. The Ni cathode undergoes a proton intercalation/extraction reaction: $NiOOH + H_2O + e^- \leftrightarrow Ni(OH)_2 + OH^-$.[55] In alkaline Zn-MnO$_2$ batteries, the Zn anodic reactions are the same as Ni-Zn batteries, and the MnO$_2$ cathodic reactions are $MnO_2 + H_2O + e^- \leftrightarrow MnOOH + OH^-$.[56] Since the Zn is thermodynamically unstable in the concentrated KOH (alkaline) electrolyte, the anode is spontaneously under the attack, which leads to a strong self-discharge throughout the life of the battery.[56] During this corrosion process, the surface of the cathode and anode can also create an electrochemical short circuit between the active sites which cause the irreversible capacity loss. In addition, the corrosion of the Zn anode leads to Zn consumption and significant H$_2$ accumulation in the batteries, again leading to the capacity fading and battery rupture.[55,56] To circumvent these limitations associated with using an alkaline electrolyte, aqueous ZIBs using mild neutral or slightly acidic electrolyte have been investigated and appear to be very promising. Shoji *et al*. first reported an aqueous Zn-MnO$_2$ battery with slightly acidic zinc sulphate (ZnSO$_4$) electrolyte,[57] decreasing the corrosion of Zn anode from electrolyte and exhibiting rechargeable capacity, which demonstrated new opportunities for the development of rechargeable zinc-ion batteries. From literature it is seen that the manganese based, and vanadium based cathode materials in combination with the ZnSO$_4$, and Zn(CF$_3$SO$_3$)$_2$ electrolytes are the most commonly explored to date.[52,58] However, the development of the insertion host for aqueous ZIBs is still in its open stage and in-depth understanding of the insertion/extraction process is required.

1.5.1 Energy storage mechanisms in mild aqueous zinc battery systems

Unlike the well-known lithium-ion based energy storage chemistries (e.g. insertion, conversion, and alloying reaction mechanism), the reaction mechanisms in aqueous ZIBs systems are not yet well understood. In aqueous $Zn-MnO_2$ systems, three different reaction mechanisms have been proposed, as shown in **Figure 1.5**: Zn^{2+} insertion/extraction[59-61], H^+/Zn^{2+} combined reaction[62], and a chemical conversion reaction.[63]
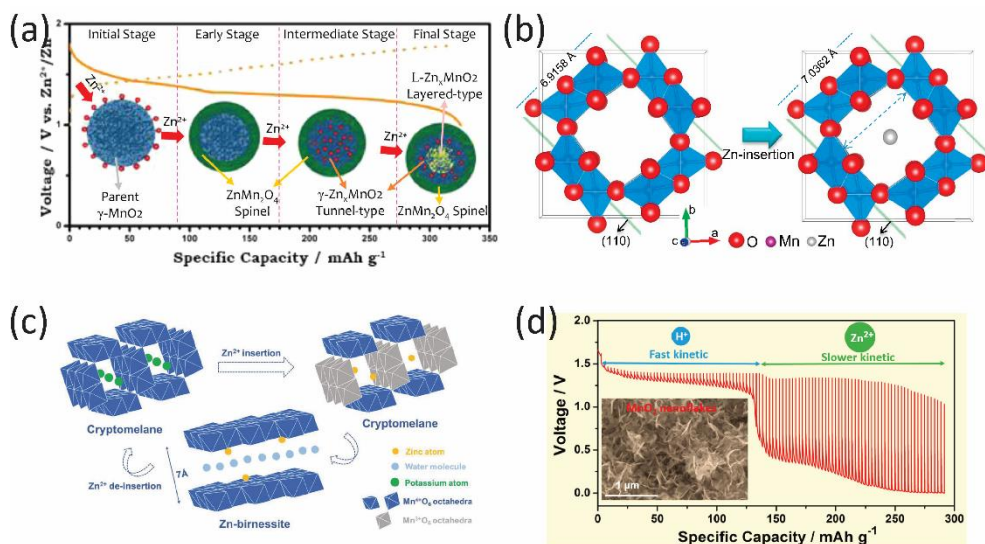
Figure 1.5. Typical examples of different reactions mechanisms in aqueous ZIBs based on manganese cathode materials. (a) Schematic illustration of Zn^{2+} insertion process in $γ-MnO_2$ cathode.[59] Reprinted with permission from ref. 59. Copyright 2015, American Chemical Society. (b) Schematic illustration of Zn^{2+} insertion into tunnel structure $α-MnO_2$ which cause the expansion of tunnel and the interplanar spacing change of adjacent (110) planes.[60] Copyright 2015, Elsevier. (c) Schematic illustration of phase transition between Zn-birnessite and $α-MnO_2$.[58,64] Copyright 2018, Wiley. (d) Galvanostatic intermittent titration technique (GITT) profile of $ε-MnO_2$ cathode, indicating two different reaction processes in aqueous ZIBs.[62] Reprinted with permission from ref. 62. Copyright 2017, American Chemical Society.

Wei C. *et el.* reported the electrochemical performances of MnO_2 with different tunnel structures (α-, β-, γ-, and δ-) in aqueous ZIBs using a $ZnSO_4$ electrolyte, wherein it was found that the larger tunnel structure is favourable for Zn^{2+} ion storage.[61] Further research revealed a detailed Zn^{2+} insertion mechanism for the $γ-MnO_2$ cathode in ZIBs that undergoes several phase transformation processes (**Figure 1.5a**): In the early stage of Zn^{2+} insertion, the tunnel-type $γ-MnO_2$ partially transforms to spinel-type $ZnMn_2O_4$; Then, in the intermediate stage with continuous Zn^{2+} insertion, transformation to the tunnel-type

γ-Zn_xMnO_2 occurs; Finally, as the Zn^{2+} is fully inserted into the tunnels, the layered-type γ-Zn_xMnO_2 phase emerges.[59] During this Zn^{2+} insertion process, the manganese ion redox is gradually reduced from Mn^{4+} to Mn^{3+}/Mn^{2+}. α-MnO_2 with a partial tunnel structure is another widely studied cathode material for aqueous ZIBs. The interplanar spacing of the (110) plane was calculated to expanded from 6.915 to 7.036 Å during Zn^{2+} insertion (**Figure 1.5b**) resulting in a 3.12% change of the unit cell volume.[60] However, another study reported that the Zn^{2+} insertion mechanism in α-MnO_2 involves a phase transition between the tunnelled structure and layered (Zn-buserite) MnO_2 polymorph structure.[64] This is shown in **Figure 1.5c**, with the insertion of Zn^{2+}, Mn^{4+} is reduced to Mn^{3+}, and the bridge-like double chains of $Mn^{3+}O$ units are gradually formed because of the Mn^{2+} dissolution reaction. Afterwards, the Zn-birnessite is formed by the loss of intercalated zinc ions and water molecules from the layers of buserite.[58] ε-MnO_2 with a nanoflake structure was reported to follow a combined H^+/Zn^{2+} insertion and extraction mechanism.[62] Galvanostatic intermittent titration technique (GITT) measurements were carried out to verify the two-step reaction process (**Figure 1.5d**): a fast kinetic and a slower kinetic reaction. In the first step, the MnO_2 was transformed to MnOOH *via* the H^+ insertion reaction, and in the second step, the MnO_2 was transformed to $ZnMn_2O_4$ *via* the Zn^{2+} insertion reaction. Apart from the Zn^{2+} insertion/extraction mechanism in aqueous ZIBs system with the MnO_2 cathode, a very different chemical conversion mechanism was also proposed based on the reversible precipitation/dissolution of zinc hydroxide sulfate ($Zn_4(OH)_6SO_4 \cdot nH_2O$) and the conversion reaction between MnOOH and MnO_2.[63] This chemical conversion reaction was deduced to be triggered by pH changes of the electrolyte during the discharge/charge process. The $Zn_4(OH)_6SO_4 \cdot 5H_2O$ phase was confirmed as the surface product on the cathode after discharge, and the formation of MnOOH was also identified after discharge. According to the results, the reversible discharge/charge behaviour between MnO_2 and MnOOH/ $Zn_4(OH)_6SO_4 \cdot 5H_2O$ can be described by equations (5)-(7) [63]:

$$H_2O \leftrightarrow H^+ + OH^- \qquad\qquad (5)$$

$$MnO_2 + H^+ + e^- \leftrightarrow MnOOH \qquad\qquad (6)$$

$$\tfrac{1}{2}Zn^{2+} + OH^- + \tfrac{1}{6}ZnSO_4 + \tfrac{x}{6}H_2O \leftrightarrow \tfrac{1}{6}ZnSO_4[Zn(OH)_2]_3 \cdot xH_2O \quad (7)$$
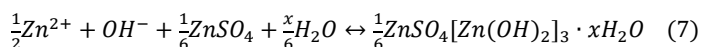
Although various MnO_2 polymorphs have gained momentum as cathode candidates for aqueous ZIBs, they suffer from the drawback that any generated dissolvable Mn^{2+} can lead to active material loss and capacity fading during the phase transition as Zn^{2+} is inserted. Studies have reported that the $MnSO_4$ additive in the electrolyte can suppress the dissolution of Mn^{2+} ions.[62,63] However, the intrinsically poor

electrical conductivity of MnO_2 should also be considered as a drawback towards the development of better ZIBs systems. Hence, it is of vital importance to develop other material to abundant the choice of Zn^{2+} host cathode material for aqueous ZIBs. Vanadium-based cathode materials have attracted lots of attention for ZIBs, showing higher energy densities and better capacity retention than MnO_2 based cathode.[65-72] **Figure 1.6** shows three different Zn ion storage mechanisms for aqueous ZIBs during discharge/charge based on three different vanadium oxide cathodes. Kundu *et al.* reported a vanadium oxide bronze ($Zn_{0.25}V_2O_5 \cdot nH_2O$) as a cathode for a ZIBs, which undergoes Zn^{2+} insertion/extraction accompanied by a water intercalation/deintercalation mechanism.[65] As shown in **Figure 1.6a**, the $Zn_{0.25}V_2O_5 \cdot nH_2O$ interlayer was slightly expanded due to water intercalation after immersed in aqueous electrolyte. The water molecules were expelled by Zn^{2+} ions inserted into the $Zn_{0.25}V_2O_5 \cdot nH_2O$ interlayer during discharge. However, different results were reported for the $V_2O_5 \cdot nH_2O$ cathode, as shown in **Figure 1.6b**.[71] The interlayer distance was reduced after immersing the charged state electrode in the aqueous electrolyte, probably caused by the formation of hydrogen bonds after water molecules inserted into the interlayer. During discharge, the interlayer distance increased because of the Zn^{2+} intercalation and the phase transition reaction. It was claimed that the interlayer water shield the effective charge of Zn^{2+} and increase the discharge distance between Zn^{2+} and the neighbouring O^{2-}, promoting an extremely high rate discharge/charge performance. According to the observation, the water molecules is claimed play a critical role in this reversible process including buffering Zn^{2+} ions, lowering the activation energy for charge transfer and expanding/contracting the oxide layered structure facile the Zn^{2+} inserted/extracted.
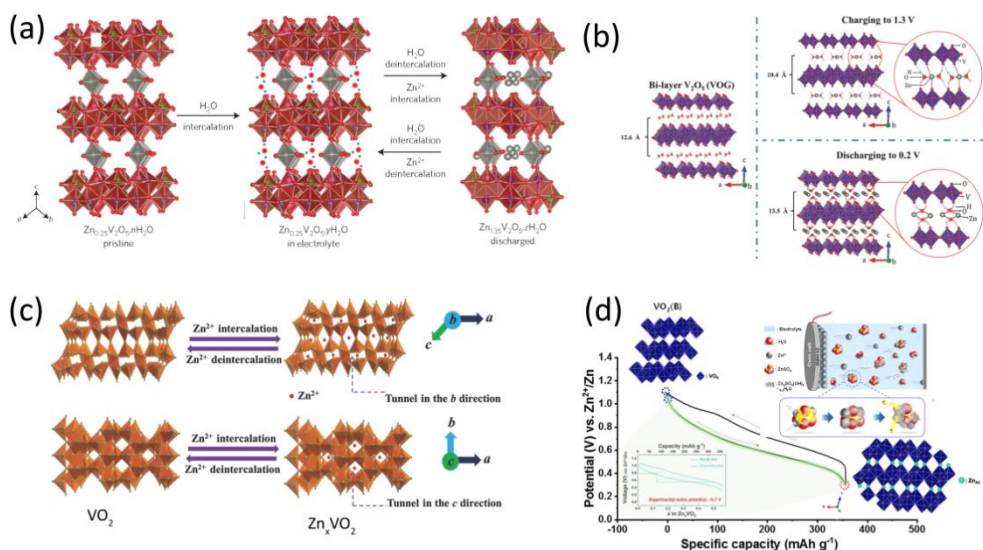
Figure 1.6. Examples of reaction mechanism for Zn ions storage in ZIBs with different V- based cathodes. (a) and (b) Schematic illustration of Zn^{2+} insertion/extraction process in $Zn_{0.25}V_2O_5 \cdot nH_2O$[65] (Copyright 2016, Springer Nature) and $V_2O_5 \cdot nH_2O$[71] (Copyright 2017. Wiley) aided by the structure water during discharge/charge. (c) and (d) Two different Zn ion storage mechanism of ZIBs with VO_2 cathode.[68,72] Copyright 2018, Wiley. Copyright 2018, American Chemical Society.

VO_2 is another suitable cathode for aqueous ZIBs, exhibiting a high reversible capacity and a high rate capability by the intense charge repulsion of bivalent Zn^{2+}. Ding *et al.* reported a simple Zn^{2+} ion insertion/extraction mechanism for VO_2 nanofibers (**Figure 1.6c**) which exhibited little structural changes upon Zn^{2+} intercalation.[72] It was speculated that the VO_2 nanofiber structure possessed unique tunnel transport pathway with big sizes (0.82 and 0.5 nm^2 along the b- and c-axes) showing little crystalline structure change when Zn^{2+} ions are inserted, enabling high reversible capacity and excellent rate capability. Park *et al.* also reported Zn^{2+} intercalation mechanism due to the open-structure of VO_2 in a $ZnSO_4$ aqueous electrolyte (**Figure 1.6d**).[68] However, they also observed the formation of $Zn_4(OH)_6SO_4 \cdot 5H_2O$ surface products during discharge, which was claimed to be responsible for the capacity fading during cycling. According to the observations in aqueous $Zn-MnO_2$ batteries,[63] it seemed that the $Zn_4(OH)_6SO_4 \cdot nH_2O$ surface product is highly reversible and is mainly attribute to the energy conversion process. This makes the role of $Zn_4(OH)_6SO_4 \cdot nH_2O$ in vanadium based cathode in aqueous ZIBs a topic of debate, and its formation and decomposition mechanism requires better understanding. Moreover, the recent research has found that both MnO_2 and vanadium oxide cathodes are also dominant proton intercalation materials compared to the oxides that undergo exclusive

Zn^{2+} storage.[73] The reversible formation/decomposition of the $Zn_4(OH)_6SO_4 \cdot nH_2O$ precipitate on the cathode surface company with reversible proton insertion/extraction in oxides. The formation of $Zn_4(OH)_6SO_4 \cdot nH_2O$ is speculated by the deposition reaction of Zn^{2+} and the electrolyte anion with OH^- (originates from water splits). This energy storage mechanism in aqueous ZIBs can be described as a $Zn_4(OH)_6SO_4 \cdot nH_2O$ buffering leads to the continuous removal of OH^- precipitate on the electrode surface and H^+ insertion/extraction in the oxide crystallite structure, thereby maintaining a mildly acidic value in the electrolyte.[73]

1.6 Understanding the reaction mechanism of the aqueous Zn/VO₂ battery in this thesis

Rechargeable aqueous ZIBs are considered to be very promising for cheap stationary energy storage. The challenge is to develop cheap electrodes that are able to combine a high power density with a long cycle life, which demands facile charge transport and small structural changes respectively.

Recently vanadium oxides have been reported as promising Zn-ion electrodes, however, pending issues are potential proton co-insertion, sluggish Zn-ion transport and large structural changes upon Zn-ion insertion. Here we report on a fundamental shift in the reaction mechanism from Zn-ion insertion towards proton insertion in VO_2 nanorods driven by the salt anion solvation and stability of the solid phases. Proton insertion is demonstrated to occur for the $ZnSO_4$ aqueous electrolyte, where concurrent $Zn_4(OH)_6SO_4 \cdot 5H_2O$ deposition on the VO_2 surface occurs. This reaction mechanism is highly reversible due to the limited structural distortion of the VO_2 lattice on proton insertion and the high proton mobility appears responsible for the relatively good rate performances. A key finding is that these results imply a competition between proton and Zn-ion insertion, which can be controlled by the choice of the salt. The proton insertion into the VO_2 creates the minor structural change facilitating the stability of the electrode during repeat cycles. However, the companied formation of the $Zn_4(OH)_6SO_4 \cdot nH_2O$ surface compounds changes the kinetic behaviour of proton insertion process, which needs further understand the advantages and disadvantages. Thus with respect to its performance, this proposed mechanism for Zn/VO2 aqueous batteries opening a new route towards designing aqueous zinc-ion stationary batteries.

References

1. Braff, W. A.; Mueller, J. M.; Trancik, J. E. *Nat. Clim. Chang.* **2016**, *6*, 964.

2. Yang, Z.; Zhang, J.; Kintner-Meyer, M. C. W.; Lu, X.; Choi, D.; Lemmon, J. P.; Liu, J. *Chem. Rev.* **2011**, *111*, 3577.

3. Evans, A.; Strezov, V.; Evans, T. J. *Renew. Sust.* Energy *Rev.* **2012**, *16*, 4141.

4. Dunn, B.; Kamath, H.; Tarascon, J. M. *Science* **2011**, *334*, 928.

5. Armand, M.; Tarascon, J. M. *Nature* **2008**, *451*, 652.

6. Tarascon, J. M.; Armand, M. *Nature* **2001**, *414*, 359.

7. Lim, H.-D.; Lee, B.; Bae, Y.; Park, H.; Ko, Y.; Kim, H.; Kim, J.; Kang, K. *Chem. Soc. Rev.* **2017**, *46*, 2873.

8. Bruce, P. G.; Freunberger, S. A.; Hardwick, L. J.; Tarascon, J. M. *Nat. Mater.* **2012**, *11*, 19.

9. Mahne, N.; Fontaine, O.; Thotiyl, M. O.; Wilkening, M.; Freunberger, S. A. *Chem. Sci.* **2017**, *8*, 6716.

10. Geng, D.; Ding, N.; Hor, T. S. A.; Chien, S. W.; Liu, Z.; Wuu, D.; Sun, X.; Zong, Y. *Adv. Energy Mater.* **2016**, *6,* 1502164

11. Girishkumar, G.; McCloskey, B.; Luntz, A. C.; Swanson, S.; Wilcke, W. *J. Phys. Chem. Lett.* **2010**, *1*, 2193.

12. Abraham, K. M.; Jiang, Z. *J. Electrochem. Soc.* **1996**, *143*, 1.

13. Black, R.; Adams, B.; Nazar, L. F. *Adv. Energy Mater.* **2012**, *2*, 801.

14. Luntz, A. C.; McCloskey, B. D. *Chem. Rev.* **2014**, *114*, 11721.

15. Aurbach, D.; McCloskey, B. D.; Nazar, L. F.; Bruce, P. G. *Nat. Energy* **2016**, *1*, 16128.

16. Horstmann, B.; Gallant, B.; Mitchell, R.; Bessler, W. G.; Shao-Horn, Y.; Bazant, M. Z. *J. Phys. Chem. Lett.* **2013**, *4*, 4217.

17. Johnson, L.; Li, C.; Liu, Z.; Chen, Y.; Freunberger, S. A.; Ashok, P. C.; Praveen, B. B.; Dholakia, K.; Tarascon, J.-M.; Bruce, P. G. *Nat. Chem.* **2014**, *6*, 1091.

18. Gao, X.; Chen, Y.; Johnson, L.; Bruce, P. G. *Nat. Mater.* **2016**, *15*, 882.

19. Laoire, C. O.; Mukerjee, S.; Abraham, K. M.; Plichta, E. J.; Hendrickson, M. A. *J. Phys. Chem. C* **2010**, *114*, 9178.

20. Adams, B. D.; Radtke, C.; Black, R.; Trudeau, M. L.; Zaghib, K.; Nazar, L. F. *Energy Environ. Sci.* **2013**, *6*, 1772.

21. Gutmann, V. *Coordination Chem. Rev.* **1976**, *18*, 225.

22. Henderson, W. A. *J. Phys. Chem. B* **2006**, *110*, 13177.

23. Aetukuri, N. B.; McCloskey, B. D.; García, J. M.; Krupp, L. E.; Viswanathan, V.; Luntz, A. C. *Nat Chem* **2015**, *7*, 50.

24. Luntz, A. C.; Viswanathan, V.; Voss, J.; Varley, J. B.; Nørskov, J. K.; Scheffler, R.; Speidel, A. *J. Phys. Chem. Lett.* **2013**, *4*, 3494.

25. Burke, C. M.; Pande, V.; Khetan, A.; Viswanathan, V.; McCloskey, B. D. *Proc. Natl. Acad. Sci.* **2015**, *112*, 9293.

26. Bryantsev, V. S.; Giordani, V.; Walker, W.; Blanco, M.; Zecevic, S.; Sasaki, K.; Uddin, J.; Addison, D.; Chase, G. V. *J. Phys. Chem. A* **2011**, *115*, 12399.

27. Bryantsev, V. S.; Blanco, M. *J. Phys. Chem. Lett.* **2011**, *2*, 379.

28. Ganapathy, S.; Adams, B. D.; Stenou, G.; Anastasaki, M. S.; Goubitz, K.; Miao, X.-F.; Nazar, L. F.; Wagemaker, M. *J. Am. Chem. Soci.* **2014**, *136*, 16335.

29. Lu, Y.-C.; Shao-Horn, Y. *J. Phys. Chem. Lett.* **2013**, *4*, 93.

30. Hummelshøj, J. S.; Luntz, A. C.; Nørskov, J. K. *J. Chem. Phys.* **2013**, *138*, 034703.

31. Yilmaz, E.; Yogi, C.; Yamanaka, K.; Ohta, T.; Byon, H. R. *Nano Lett.* **2013**, *13*, 4679.

32. Tian, F.; Radin, M. D.; Siegel, D. J. *Chem. Mater.* **2014**, *26*, 2952.

33. Radin, M. D.; Monroe, C. W.; Siegel, D. J. *Chem. Mater.* **2015**, *27*, 839.

34. Radin, M. D.; Rodriguez, J. F.; Tian, F.; Siegel, D. J. *J. Amer. Chem. Soc.* **2012**, *134*, 1093.

35. Gallant, B. M.; Mitchell, R. R.; Kwabi, D. G.; Zhou, J.; Zuin, L.; Thompson, C. V.; Shao-Horn, Y. *J. Phys. Chem. C* **2012**, *116*, 20800.

36. Gerbig, O.; Merkle, R.; Maier, J. *Adv. Mater.* **2013**, *25*, 3129.

37. Khetan, A.; Pitsch, H.; Viswanathan, V. *J. Phys. Chem. Lett.* **2014**, *5*, 2419.

38. Khetan, A.; Luntz, A.; Viswanathan, V. *J. Phys. Chem. Lett.* **2015**, *6*, 1254.

39. Lu, Y.-C.; Gallant, B. M.; Kwabi, D. G.; Harding, J. R.; Mitchell, R. R.; Whittingham, M. S.; Shao-Horn, Y. *Energy Environ. Sci.* **2013**, *6*, 750.

40. Peng, Z.; Freunberger, S. A.; Chen, Y.; Bruce, P. G. *Science* **2012**, *337*, 563.

41. Su, D. W.; Dou, S. X.; Wang, G. X. *J. Mater. Chem. A* **2015**, *3*, 18384.

42. Li, F.; Tang, D.-M.; Zhang, T.; Liao, K.; He, P.; Golberg, D.; Yamada, A.; Zhou, H. *Adv. Energy Mater.* **2015**, *5*, 1500294.

43. Lim, H.-D.; Lee, B.; Zheng, Y.; Hong, J.; Kim, J.; Gwon, H.; Ko, Y.; Lee, M.; Cho, K.; Kang, K. *Nat. Energy* **2016**, *1*, 16066.

44. Liu, T.; Leskes, M.; Yu, W.; Moore, A. J.; Zhou, L.; Bayley, P. M.; Kim, G.; Grey, C. P. *Science* **2015**, *350*, 530.

45. Shen, Y.; Zhang, W.; Chou, S.-L.; Dou, S.-X. *Science* **2016**, *352*, 667.

46. Viswanathan, V.; Pande, V.; Abraham, K. M.; Luntz, A. C.; McCloskey, B. D.; Addison, D. *Science* **2016**, *352*, 667.

47. Burke, C. M.; Black, R.; Kochetkov, I. R.; Giordani, V.; Addison, D.; Nazar, L. F.; McCloskey, B. D. *ACS Energy Lett.* **2016**, *1,* 747.

48. Zubi, G.; Dufo-López, R.; Carvalho, M.; Pasaoglu, G. *Renew. Sust. Energy Revi.* **2018**, *89*, 292.

49. Schmidt, O.; Hawkes, A.; Gambhir, A.; Staffell, I. *Nat. Energy* **2017**, *2*, 17110.

50. Grey, C. P.; Tarascon, J. M. *Nat. Mater.* **2017**, *16*, 45.

51. Kim, H.; Hong, J.; Park, K.-Y.; Kim, H.; Kim, S.-W.; Kang, K. *Chem. Rev.* **2014**, *114*, 11788.

52. Fang, G.; Zhou, J.; Pan, A.; Liang, S. *ACS Energy Lett.* **2018**, *3*, 2480.

53. Winter, M.; Brodd, R. J. *Chem. Rev.* **2004**, *104*, 4245.

54. Cheng, F. Y.; Chen, J.; Gou, X. L.; Shen, P. W. *Adv. Mater.* **2005**, 17, 2753.

55. Parker, J. F.; Chervin, C. N.; Pala, I. R.; Machler, M.; Burz, M. F.; Long, J. W.; Rolison, D. R. *Science* **2017**, *356*, 415.

56. Faegh, E.; Omasta, T.; Hull, M.; Ferrin, S.; Shrestha, S.; Lechman, J.; Bolintineanu, D.; Zuraw, M.; Mustain, W. E. *J. Electrochem. Soc.* **2018**, *165*, A2528.

57. Shoji, T.; Hishinuma, M.; Yamamoto, T. *J. Appl. Electrochem.* **1988**, *18*, 521.

58. Song, M.; Tan, H.; Chao, D.; Fan, H. J. *Adv. Funct. Mater.* **2018**, *28*, 1802564.

59. Alfaruqi, M. H.; Mathew, V.; Gim, J.; Kim, S.; Song, J.; Baboo, J. P.; Choi, S. H.; Kim, J. *Chem. Mater.* **2015**, *27*, 3609.

60. Alfaruqi, M. H.; Gim, J.; Kim, S.; Song, J.; Jo, J.; Kim, S.; Mathew, V.; Kim, J. *J. Power Sources* **2015**, *288*, 320.

61. Wei, C.; Xu, C.; Li, B.; Du, H.; Kang, F. *J. Phys. Chem. Solids* **2012**, *73*, 1487.

62. Sun, W.; Wang, F.; Hou, S.; Yang, C.; Fan, X.; Ma, Z.; Gao, T.; Han, F.; Hu, R.; Zhu, M.; Wang, C. *J. Am. Chem. Soc.* **2017**, *139*, 9775.

63. Pan, H.; Shao, Y.; Yan, P.; Cheng, Y.; Han, K. S.; Nie, Z.; Wang, C.; Yang, J.; Li, X.; Bhattacharya, P.; Mueller, K. T.; Liu, J. *Nat. Energy* **2016**, *1*, 16039.

64. Lee, B.; Lee, H. R.; Kim, H.; Chung, K. Y.; Cho, B. W.; Oh, S. H. *Chem. Commun.* **2015**, *51*, 9265.

65. Kundu, D.; Adams, B. D.; Duffort, V.; Vajargah, S. H.; Nazar, L. F. *Nat. Energy* **2016**, *1*, 16119.

66. Alfaruqi, M. H.; Mathew, V.; Song, J.; Kim, S.; Islam, S.; Pham, D. T.; Jo, J.; Kim, S.; Baboo, J. P.; Xiu, Z.; Lee, K.-S.; Sun, Y.-K.; Kim, J. *Chem. Mater.* **2017**, *29*, 1684.

67. He, P.; Quan, Y.; Xu, X.; Yan, M.; Yang, W.; An, Q.; He, L.; Mai, L. *Small* **2017**, 1702551.

68. Park, J.-S.; Jo, J. H.; Aniskevich, Y.; Bakavets, A.; Ragoisha, G.; Streltsov, E.; Kim, J.; Myung, S.-T. *Chem. Mater.* **2018**, *30*, 6777.

69. Wan, F.; Zhang, L.; Dai, X.; Wang, X.; Niu, Z.; Chen, J. *Nat. Commun.* **2018**, *9*, 1656.

70. Wei, T.; Li, Q.; Yang, G.; Wang, C. *J. Mater. Chem. A* **2018**, *6*, 8006.

71. Yan, M.; He, P.; Chen, Y.; Wang, S.; Wei, Q.; Zhao, K.; Xu, X.; An, Q.; Shuang, Y.; Shao, Y.; Mueller, K. T.; Mai, L.; Liu, J.; Yang, J. *Adv. Mater.* **2018**, *30*, 1703725.

72. Ding, J.; Du, Z.; Gu, L.; Li, B.; Wang, L.; Wang, S.; Gong, Y.; Yang, S. *Adv. Mater.* **2018**, *30*, 1800762.

73. Oberholzer, P.; Tervoort, E.; Bouzid, A.; Pasquarello, A.; Kundu, D. *ACS Appl. Mater. Interfaces* **2019**, *11*, 674.

Chapter 2

Understanding the Electrochemical Formation and Decomposition of Li₂O₂ and LiOH with *Operando* X-ray Diffraction

This chapter is based on:
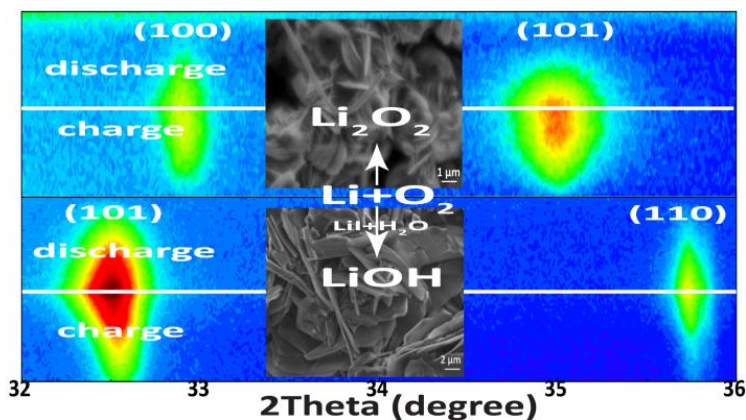
Operando XRD combined with Retivel refinement has been taken to reveal the detail crystalline structure evolution of the products for Li-O_2 battery during cycling in DME and DME-LiI electrolyte, respectively. With the additive of LiI and H_2O, LiOH rather than Li_2O_2 become the dominant products in Li-O_2 battery, which also shows completely different morphology.

Abstract

The lithium air, or Li-O$_2$, battery system is a promising electrochemical energy storage system owing to its very high theoretical specific energy, as required by automotive applications. Fundamental research has resulted in much progress in mitigating detrimental (electro)chemical processes, however the detailed structural evolution of the crystalline Li$_2$O$_2$ and LiOH discharge products, held at least partially responsible for the limited reversibility and poor rate performance, is hard to measure *operando* under realistic electrochemical conditions. The present study uses Rietveld refinement of *operando* X-ray diffraction data during a complete charge-discharge cycle to reveal the detailed structural evolution of Li$_2$O$_2$ and LiOH crystallites in DME and DME-LiI electrolytes, respectively. The anisotropic broadened reflections confirm and quantify the platelet crystallite shape of Li$_2$O$_2$ and LiOH and shows how the average crystallite shape evolves during discharge and charge. Li$_2$O$_2$ is shown to form *via* a nucleation and growth mechanism, whereas the decomposition appears to start at the smallest Li$_2$O$_2$ crystallite sizes due to their larger exposed surface. In the presence of LiI, platelet LiOH crystallites are formed by a particle-by-particle nucleation and growth process and at the end of discharge H$_2$O depletion is suggested to result in sub stoichiometric Li(OH)$_{1-x}$, which appears preferentially decomposed during charge. O*perando* XRD proves the cyclic formation and decomposition of the LiOH crystallites in the presence of LiI over multiple cycles, and the structural evolution provides key information for understanding and improving these highly relevant electrochemical systems.

2.1 Introduction

The rechargeable non-aqueous Li-O$_2$ battery has been widely investigated motivated by its extremely high theoretical energy density amounting to 3500 Wh/kg for the overall battery reaction $2Li + O_2 \underset{\text{charge}}{\overset{\text{discharge}}{\rightleftarrows}} Li_2O_2$.[1] In the past ten years,[2-4] significant progress has been realized in understanding the complex chemistry that governs the functioning of this battery system.[5-12] This has resulted in several strategies to improve the performance of Li-O$_2$ batteries.[3, 4, 13-15] One deals with the reactivity of the porous carbon based gas diffusion electrode with the electrolyte and the Li$_2$O$_2$ discharge product. This was mitigated by the use of non-carbon porous electrodes made of gold,[3] titanium carbide,[4] metallic Ti$_4$O$_7$,[14] to name a few, or by the alternative strategy of coating the porous carbon substrate with a non-carbon based material.[15] Another important step forward has been establishing the relationship between the electrolyte solvent donor number (DN) and the morphology of the peroxide that forms.[7] The high solubility of the intermediate LiO$_2$ product in high DN electrolytes leads to a solution mediated Li$_2$O$_2$ growth mechanism, resulting in toroids of Li$_2$O$_2$ responsible for large discharge capacities. In contrast, low DN electrolytes lead to a surface growth mechanism of Li$_2$O$_2$, resulting in thin Li$_2$O$_2$ films of restricting the capacity and reversibility.[7] Johnson *et al.* have pointed out that for DME, having an intermediate DN, both pathways for the O$_2$ reduction occur simultaneously at a high voltage.[7] Thereby the performance of the Li-O$_2$ battery is mainly governed by the generation and decomposition mechanism of Li$_2$O$_2$ which itself is a poor ionic and electronic conductor.[16] In addition, the oxygen species involved in the oxygen reduction reaction (ORR) and in the inverse oxygen evolution reaction (OER) are highly reactive with the organic environment and traces of moisture, leading to the formation of parasitic products like-Li$_2$CO$_3$, LiOH, and CO$_2$ having a negative impact on the Li-O$_2$ battery performance.[16-20]

Recent studies have shown that trace amounts of H$_2$O can enhance the formation of Li$_2$O$_2$ and thereby improve the performance of Li-O$_2$ batteries.[21-23] The water in the electrolytes catalyses the reaction at the cathode, typically through the presence of ruthenium and manganese nanoparticles on carbon black, to form Li$_2$O$_2$ and LiOH during discharge.[22] The formation of LiOH occurs *via* the reaction of Li$_2$O$_2$ with H$_2$O[23] and decomposition appears possible below 3.2 V with ruthenium-based catalysts,[22, 23] making LiOH an interesting cyclic discharge product for Li-O$_2$ batteries. Highly cyclic crystalline LiOH formation was achieved by adding lithium iodide (LiI) to a DME/Li$^+$ electrolyte in combination with a graphene oxide electrode, both with and without the addition of H$_2$O.[24] The soluble LiI redox mediator was shown to reduce the overpotential of the charge

process, suggesting an iodine mediated decomposition mechanism.[25] If this decomposition mechanism results in oxygen evolution, it would make a new reversible mechanism of Li-O$_2$ battery, which is currently under debate as it has been proposed to be thermodynamically unfavourable[26] and it has been suggested that I$^-$ is oxidised rather than LiOH.[27] Burke, C.M. et al. have recently reported that the LiOH crystallite was formed by 4e$^-$ reduction process with the addition of LiI and H$_2$O in the DME electrolyte on discharge, however, the decomposition of LiOH crystallite was primarily attributed to iodo-oxygen electrochemistry rather than reversible oxygen evolution.[28]

Evidently, the performance of aprotic Li-O$_2$ batteries is directly determined by the reversible formation mechanism of the discharge products, either being Li$_2$O$_2$ or LiOH. Therefore, studying the nature and the evolution of the discharge products, preferably under realistic *operando* conditions is paramount for future design of mechanisms and materials aiming at an improved performance.

In previous work[29] *operando* X-ray diffraction (XRD) was used to study the decomposition of Li$_2$O$_2$ in a TEGDME electrolyte, showing that the decomposition mechanism *via* a sub-stoichiometric Li$_{2-x}$O$_2$ proceeds during charge, in agreement with density functional theory (DFT predictions),[30] and that thinner platelet crystallites decompose preferentially. The decomposition of individual Li$_2$O$_2$ grains, by *operando* nano-beam synchrotron XRD, showed a slow concurrent Li$_2$O$_2$ decomposition *via* the more reactive (001) facets.[31] More *operando* XRD studies have explored the time-dependent formation and decomposition of Li$_2$O$_2$ crystallites by comparing the changes of Li$_2$O$_2$ peak area and the full width at half maximum (FWHM), revealing the character of the Li$_2$O$_2$ crystallites during (dis)charge.[32, 33] However, no detailed insight exists for the formation of the Li$_2$O$_2$ crystallites during discharge. Moreover, little is known about the *operando* formation and decomposition of LiOH presently under debate[25-27] and how the presence of the LiI redox mediator and water affects the structure of the formed species.

In the present work, *operando* XRD is used to reveal the detailed structural evolution during a complete (dis)charge cycle of Li$_2$O$_2$ and LiOH in DME and DME/LiI electrolytes respectively. Detailed Rietveld refinement of the crystalline Li$_2$O$_2$ and LiOH formation and decomposition brings forward a model for the growth and decomposition process giving novel insights in these relevant battery systems.

2.2 Materials and methods

Cathode Preparation. The cathodes were prepared by coating a slurry of activated carbon (Kuraray Chemicals) and a lithiated Nafion binder on carbon paper (Spectracarb). The

activated carbon was mixed with a Nafion binder (~5% in a mixture of lower aliphatic alcohols and water, Aldrich) with a mass ratio of about 60:40 in a milling bowl, and subsequently an amount of N-Methyl-2-pyrrolidone (NMP) (Sigma-Aldrich, anhydrous, 99.5%) was added to adjust the viscosity of the slurry. The mixture was milled for two hours at 100 rpm. The slurry was coated on a sheet of carbon paper and the coated activated carbon sheets were dried at 100 ˚C for 24 hours in a vacuum oven to remove surface adsorbed water after which disks of Ø12.7 mm were punched out. The final carbon loading on the carbon paper was determined to be 3.0 – 4.0 mg.

Electrolytes. Two different electrolyte solutions were used, each consisting of a 1,2 dimethoxy ethane (DME) (Sigma-Aldrich, >99.5%) solvent which was further dried for several days over freshly activated molecular sieves (type 4 Å) (Sigma-Aldrich) and lithium bis(trifluoromethane sulfonyl)imide salt (LiTFSI, 99.95%, Aldrich), dried in a vacuum oven at 80 ˚C for 24 hours. One electrolyte consisted of a solution of 0.5 M LiTFSI dissolved in DME, while the other consisted of a solution of 0.05 M LiI and 0.5 M LiTFSI dissolved in DME. These electrolytes will be referred to as the DME and the DME-LiI electrolytes. All the electrolyte preparations were carried out in an argon filled glovebox (H_2O and O_2 content of <1 ppm). Based on the liquid chromatogram test, there is still a large amount of water (~4000 ppm) in the electrolyte during the battery test.

Operando XRD cell. A home designed and constructed Li-O₂ battery was used for the *operando* X-ray diffraction measurements as described in detail elsewhere.[29]

Electrochemistry. The Li-O₂ battery, comprising the cathode, a glass microfiber separator (Whatman) soaked with the electrolyte, and a lithium metal anode, was assembled in the *operando* XRD battery in an argon filled glovebox. The battery was subsequently connected to O_2 (Linde, 99.9999%) under a pressure of 0.5 bar where it was allowed to equilibrate for 3 hours before it was tested. Electrochemical cycling tests were performed with a MACCOR 4000 battery cycler.

X-ray diffraction (XRD) Measurements. XRD measurements were performed using a PANalytical X'Pert Pro PW3040/60 diffractometer with Cu Kα radiation operating at 45 kV and 40 mA in an angular 2θ ranging from 31 to 65˚. Scans of about 30 minutes each were recorded for the batteries during a complete (dis)charge cycle with a current density of 0.3 mA/cm^2. Refinement of the diffraction data was carried out using the Rietveld method as implemented in the FullProf program. To more accurately fit the zero-position (effectively positioned at a different height in the cathode) of the Li₂O₂ diffraction pattern, peaks arising from the current collector as well as carbon paper were excluded from the fits.

Scanning Electron Microscopy (SEM). Electrodes were imaged at different stages of (dis)charge. Electrodes were rinsed with dry tetrahydrofuran (THF) prior to analysis, and samples were prepared in an argon-filled glovebox, using a stainless steel holder as the substrate and double-sided carbon tape as the contact point between the electrode and holder. Samples were transferred into the SEM (JEOL JSM-6010LA) under anaerobic conditions, and images were taken using an accelerating voltage of 5 kV.

2.3 Results and discussions

2.3.1 Electrochemical properties and discharge product morphology

Figure 2.1a depicts the (dis)charge curves obtained for the DME and DME-LiI electrolytes at a current density of 0.3 mA/cm^2. For both electrolytes a typical discharge plateau is observed around 2.7 V. The gradual decrease, resulting from an increasing overpotential, most likely reflects the increasing thickness of the insulating discharge products raising the electrode's resistance. For the DME and DME-LiI electrolytes, a capacity of ~ 2000 mAh/g and ~ 4000 mAh/g can be obtained, respectively when discharging to the cut-off voltage of 2.2 V *vs.* Li/Li$^+$. During charge (OER) the voltage profile steadily increases towards a voltage plateau at 4.4 V for the DME electrolyte whereas a continuously increasing voltage is observed for the DME-LiI electrolyte between 3.5 V and 4.5 V which has been attributed to the electrochemical oxidation of LiI.[25]

 Ex-situ XRD measurements were carried out to identify the discharge products for the two different electrolytes. **Figure 2.1b** presents the XRD patterns of the cathodes discharged to a 2.2 V cut-off voltage at a current density of 0.3 mA/cm^2 in the DME and DME-LiI electrolytes. Compared to the XRD pattern of the pristine electrode, new diffraction peaks appear at around 33˚, 35°, 41°, 49°, and 59° for the cathode discharged in the DME electrolyte, which can be attributed to the crystalline Li$_2$O$_2$ phase. In the cathode discharged in the DME-LiI electrolyte the diffraction peaks at 32.5˚, 35.6˚, 49˚, 51.5˚, 56˚, and 62˚ can be indexed to crystalline LiOH, the formation of which is attributed to the presence of LiI and H$_2$O in the electrolyte.
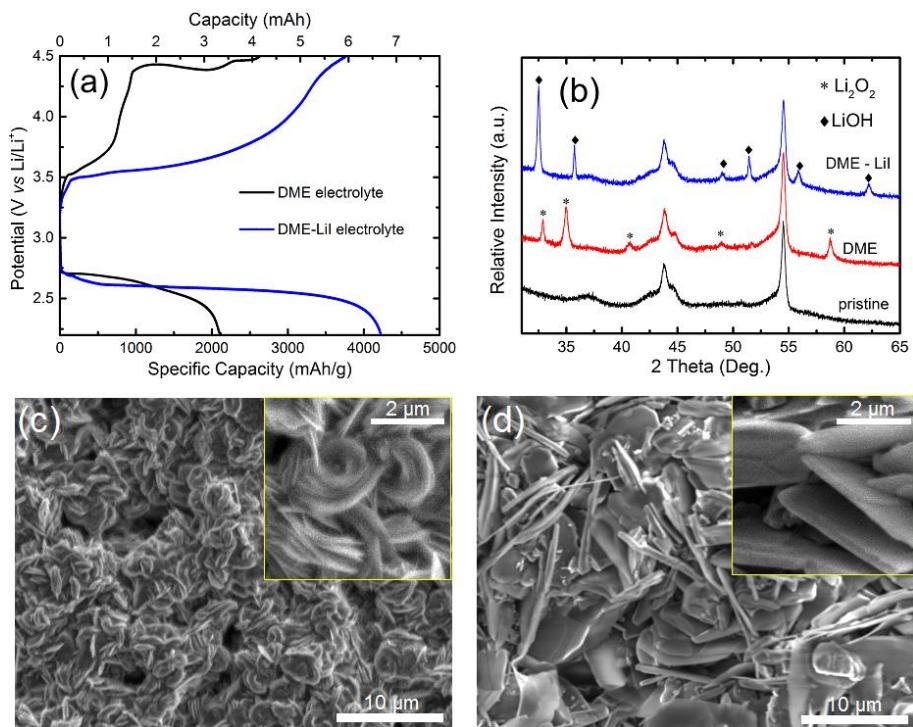
Figure 2.1. (a) Galvanostatic (dis)charge profiles for the operando Li-O₂ batteries with DME and DME-LiI electrolytes in a 2.2 to 4.5 V voltage window versus Li/Li$^+$ at a current density of 0.3 mA/cm^2. (b) XRD patterns of a pristine cathode and the cathodes at the end of discharge, with a 2.2 V cut-off voltage, in the DME and DME-LiI electrolytes, respectively. (c), (d) SEM images for the cathodes measured after discharge in DME and DME-LiI electrolytes respectively, at a current density of 0.3 mA/cm^2.

The morphology of the discharge products in the DME and DME-LiI electrolytes is shown in the SEM images in **Figures 2.1c and d. Figure 2.1c** shows the two types of primary aggregates observed for Li₂O₂ in the DME electrolyte discharged down to 2.2 V. A fraction of the Li₂O₂ particles aggregate with several parallel plates, resulting in a loosely stacked layer-by-layer toroid-like structure, and others stack more tightly to assemble into toroids. In addition, many individual Li₂O₂ platelets are observed, distributed throughout the remaining space on the carbon cathode surface. The diameter of the platelet layers, stacked in toroids is about 2.0 μm, and the thickness is between 0.5 and 0.8 μm. Prior reports have described Li₂O₂ toroids as consisting of stacked platelets with a range of shapes and sizes in ether electrolytes.[34-39] Experimental studies performed at different current densities in a DME electrolyte by Aetukuri *et al.*[35] suggested that this was due to varying levels of water contamination in the cells and different discharge currents. Griffith *et al.*[36] described a particle-growth mechanism, in which nucleation progresses *via* a ring-shaped primary structure, rather than *via* a linear or hemispherical primary structure. In

our work, the trace water left in the DME electrolyte and in the O$_2$ supplemental system may be responsible for the formation of toroidal Li$_2$O$_2$. Recently, a number of studies have explored the formation of toroidal Li$_2$O$_2$,[34-37, 40, 41] however, there appears to be no clear consensus on the crystallite growth and aggregation mechanism.
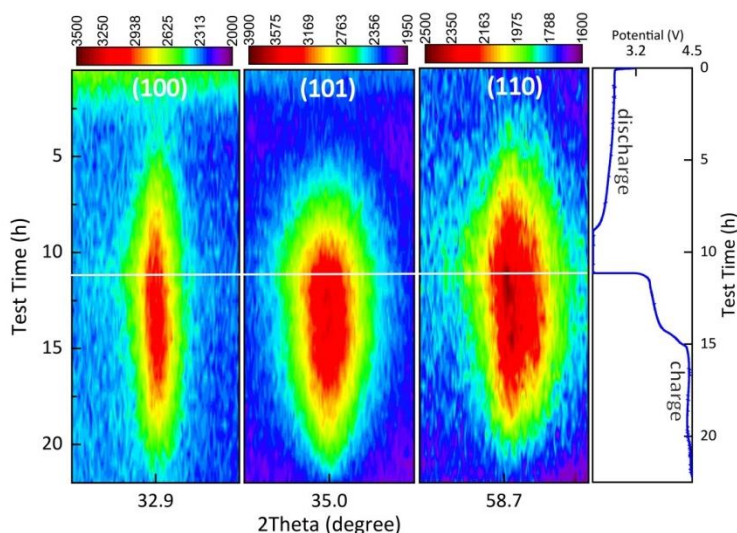
Figure 2.2. Left: Two-dimensional contour plots of the operando XRD patterns showing the 2θ region between 32.4-33.4°, 34.5-35.5°, and 58.2-59.2°, during a complete (dis)charge cycle demonstrating the Li$_2$O$_2$ formation (by the {100}, {101}, and {110} Li$_2$O$_2$ indexed reflections) and decomposition in the Li-O$_2$ battery. Right: (Dis)charge profile of the electrochemical performance in Li-O$_2$ battery. The Li-O$_2$ battery was tested by using the DME based electrolyte at a current density of 0.3 mA/cm^2.

Figure 2.1d shows the discharge product morphology of the cathode discharged in the DME-LiI electrolyte representing thick LiOH plates. The length of the LiOH plates reaches up to tens of micrometers and the thickness is in the range of 100 – 200 nm. These LiOH plates, forming on the activated carbon surface, are distinctly different from the glassy film LiOH morphology[42] on the carbon electrode during the ORR process and from the "flowerlike" agglomerated LiOH particles[25] formed on the reduced graphene oxide cathode in Li-O$_2$ batteries.

2.3.2 *Operando* XRD of Li$_2$O$_2$ formation and decomposition in DME electrolyte

Operando XRD patterns were collected for the DME electrolyte during a complete (dis)charge cycle at a current density of 0.3 mA/cm^2. The two-dimensional contour XRD plot in the 2θ region of 32.4-33.4°, 34.5-35.5°, and 58.2-59.2° in **Figure 2.2** shows the evolution of the Li$_2$O$_2$ {100}, {101}, and {110} reflections demonstrating the gradual

formation and decomposition of Li$_2$O$_2$. The {101} reflection is significantly broader than the {100} reflection, indicating anisotropic broadening of the Li$_2$O$_2$ reflections in the {00l} crystal plane direction. Although it is not possible to distinguish between size and strain broadening, given the limited 2θ data range, we assume the broadening to be the consequence of size broadening because electrochemically formed Li$_2$O$_2$ is known to form toroidal aggregates[37] consisting of stacked Li$_2$O$_2$ crystalline platelets, with the plate normal in the {00l} direction.
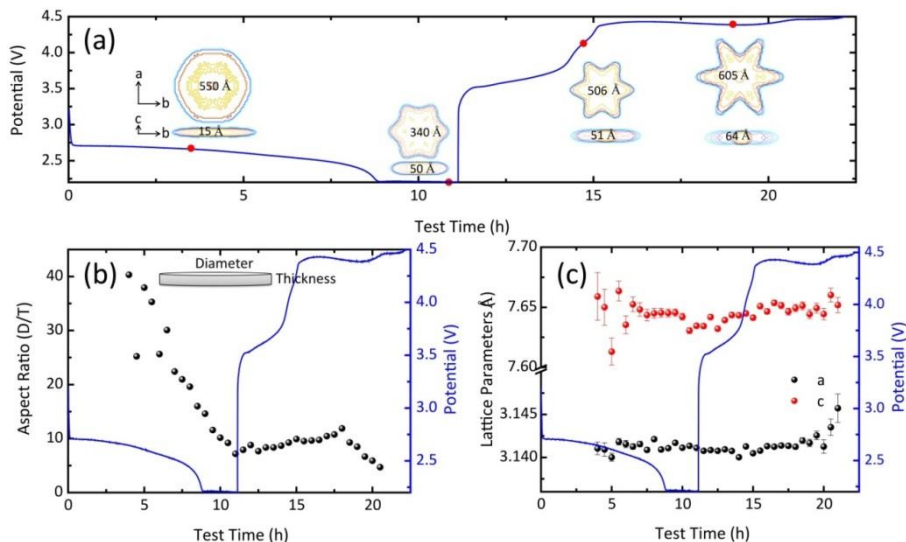
Figure 2.3. (a) The evolution of Li$_2$O$_2$ crystallite shape and (b) of the aspect ratio of the Li$_2$O$_2$ crystallite shape (diameter in the ab-plane/thickness in the c-direction), and (c) Li$_2$O$_2$ lattice parameters, resulting from Rietveld refinement during the full Galvanostatic (dis)charge cycle in the DME electrolyte. In each figure the blue line represents the voltage curve during the (dis)charge cycle at a current density of 0.3 mA/cm^2.

The integrated and normalized area as a function of discharge time for the {100} and {101} reflections of Li$_2$O$_2$ (supporting information **Figure S2.2**) show a linear increase of the peak area during discharge. However, during charge it decreases *via* two different stages, as reported previously.[29] During the initial stage of charge the integrated area decays very slowly, indicating preferential oxidation of the surface species (LiO$_2$* ,O$_2^-$*) and/or an amorphous lithium component at the lower voltage regime (2.8 – 3.4 V),[32] the latter possibly comprising of an amorphous Li$_2$O$_2$ species, or of both amorphous Li$_2$O$_2$ and side products arising from electrolyte degradation such as formate, that can be oxidized at relatively low potentials without a catalyst.[43] In the second stage the integrated Li$_2$O$_2$ peak areas exhibit a linear decrease, indicating the oxidation of the crystalline fraction of Li$_2$O$_2$.

Assuming that the observed anisotropic broadening of the XRD reflections is solely due to the crystallite size, the XRD patterns were refined with the FullProf program using a Thompson-Cox-Hastings pseudo-Voigt profile function based on spherical harmonics (SPH) to fit the anisotropic size broadening.[44] The broadening of each reflection translates in an apparent crystallite size in the direction perpendicular to the planes specified by the miller indices, shown for a number of reflections in the supporting information **Figure S2.3**. The large apparent size in the {100} direction, coincident with the *a*-lattice parameter, compared to the {004} reflection, coincident with the c-lattice parameter, is in agreement with platelet shaped Li$_2$O$_2$ crystallites reported.[37] When the crystallites are assumed to be platelets, cylinders with a large D/T (diameter/thickness) aspect ratio, the average apparent size of the Li$_2$O$_2$ plates in the {00l} direction represents the thickness of the plates, and the average apparent size in the {hk0} direction, multiplied by 3π/8, represents the average diameter of the cylinders.[45] The evolution of the aspect ratio during the complete (dis)charge cycle is shown in **Figure 2.3b**. Finally, by taking into account the size broadening of all observed reflections a detailed crystallite shape can be determined, images of which are shown in **Figure 2.3a** at different stages during the complete (dis)charge cycle.

During the discharge process the D/T aspect ratio, shown in **Figure 2.3b**, decreases drastically indicating that on average the platelets become more isotropic in shape. During charge the aspect ratio increases slightly, whereas at the end of charge it decreases again. The evolution of the average crystallite shape, shown in **Figure 2.3a**, demonstrates that the decrease in D/T aspect ratio during discharge is both due to an increase in average crystallite thickness and a decrease in average diameter. It should be realized that the crystallite dimensions, derived from the broadening of the XRD reflections, represent average values. Therefore the observed decrease in platelet width during discharge most likely does not indicate that the crystallite diameter decreases during Li$_2$O$_2$ formation. It suggests that during discharge the Li$_2$O$_2$ platelets that form, progressively are more isotropic shaped, having a smaller diameter thereby decreasing the average diameter. Similar, the increasing platelet thickness and diameter during charge, during decomposition of the Li$_2$O$_2$ crystallites, implies that thin and small platelets are decomposed first during charge, consistent with previous work.[29]

The evolution of the Li$_2$O$_2$ lattice parameters during the full (dis)charge cycle are given in **Figure 2.3c**. The *a*-lattice parameter is practically constant during the Li$_2$O$_2$ formation and decomposition, whereas the *c*-lattice parameter is 7.659 ± 0.020 Å at the beginning of discharge after which it decreases towards 7.634 ± 0.002 Å near the end of the discharge process. Because Li$_2$O$_2$ platelets with a thickness in the order of nanometers

show an expansion in the average *c*-lattice parameter due to surface relaxation,[29, 45] the decreasing *c*-lattice parameter during discharge is consistent with the progressive formation of thicker, more isotropic platelets, consistent with the evolution of the crystallite shape in **Figures 2.3a and b**. During charge, the *c*-lattice parameter is initially constant at 7.643 ± 0.002 Å before it increases slightly to 7.651 ± 0.063 Å towards the end of charge. As suggested previously, the increase of *c*-lattice parameters during charge may be caused by the decomposition of Li$_2$O$_2$ taking place *via* substoichiometric Li$_{2-x}$O$_2$ intermediates.[29]
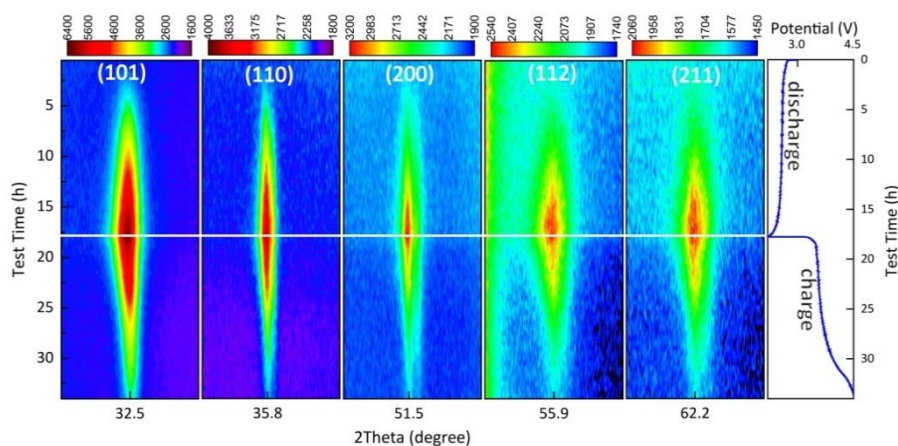
Figure 4. Left: Two-dimensional contour plots of the operando XRD patterns showing the 2θ region between 31.5-33.5°, 34.8-36.8°, 50.5-52.5°, 54.9-56.9°, and 61.2-63.2°, during a complete (dis)charge cycle demonstrating the LiOH formation ({101}, {110}, {200}, {112}, and {211} reflections) and decomposition. Right: (Dis)charge profile of the electrochemical performance in Li-O$_2$ battery. The Li-O$_2$ battery was tested by using the DME-LiI based electrolyte at a current density of 0.3 mA/cm^2.

Previously, detailed Rietveld refinement of *operando* XRD data were obtained during charge, revealed the decomposition mechanism.[29] At present, the formation of Li$_2$O$_2$ during discharge is additionally studied by *operando* XRD. Moreover, the better signal to noise ratio and better time resolution obtained allows a more detailed refinement of the anisotropic broadening of the XRD reflections during a full discharge-charge cycle, giving insight into the evolution of the crystallite shape. Based on the evolution of Li$_2$O$_2$ apparent crystallite shape and the aspect ratio D/T, the Li$_2$O$_2$ crystallites follow a distinct formation and decomposition mechanism. As is well known, the toroidal Li$_2$O$_2$ particles consist of arrays of platelet-like Li$_2$O$_2$ crystallites.[37] During discharge, the thinner Li$_2$O$_2$ crystallites, having a more anisotropic shape, form at the initial stages, whereas progressive discharging results in more isotropic shaped Li$_2$O$_2$ crystallites. Concurrently, several Li$_2$O$_2$ crystallites aggregate to form toroidal Li$_2$O$_2$ particles.[42] In the

meantime, small Li$_2$O$_2$ crystallites with a less anisotropic shape are also formed. During charge, the relatively thin Li$_2$O$_2$ anisotropic crystallites are oxidized first, followed by the thicker and more isotropic Li$_2$O$_2$ crystallites.

2.3.3 *Operando* XRD of LiOH formation and decomposition in DME-LiI electrolyte

Figure 2.4 presents the two-dimensional contour plots of the *operando* XRD patterns in the 2θ regions 31.5-33.5°, 34.8-36.8°, 50.5-52.5°, 54.9-56.9°, and 61.2-63.2°, collected for the DME-LiI electrolyte during a complete (dis)charge cycle at a current density of 0.3 mA/cm^2. The evolution of the {101}, {110}, {200}, {112}, and {211} reflections demonstrates the formation and decomposition of LiOH crystallites during discharge and charge respectively, also supported by the linear increase (discharge) and decrease (charge) of the integrated area of the LiOH {101}, {110} and {200} reflections shown in the supporting information **Figure S2.5**.
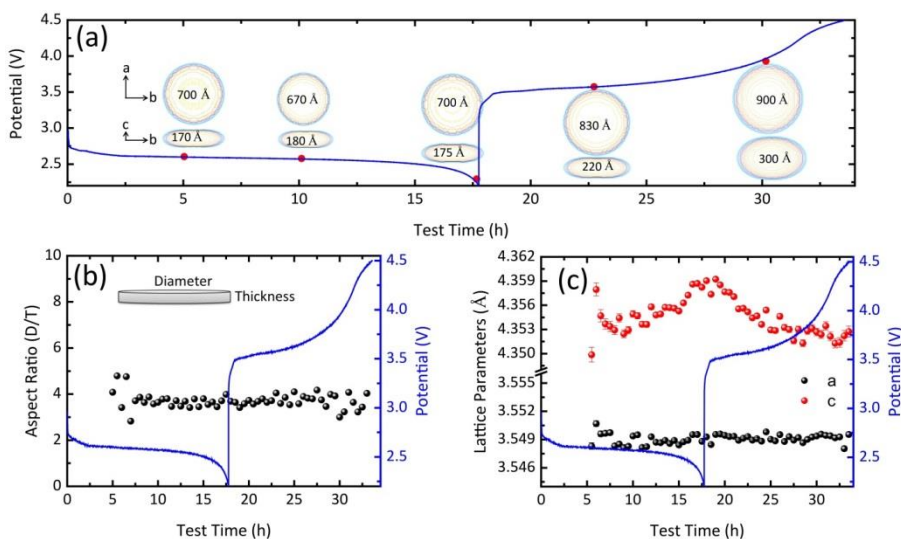
Figure 2.5. (a) The evolution of LiOH crystallite shape, (b) the aspect ratio of the LiOH crystallite shape (diameter in the ab-plane/thickness in the c-direction), and (c) the LiOH lattice parameters, resulting from Rietveld refinement during the full Galvanostatic (dis)charge cycle in the DME electrolyte. In each figure the blue line represents the voltage curve during the full Galvanostatic (dis)charge cycle in the DME electrolyte at a current density of 0.3 mA/cm^2.

The XRD reflections from the crystalline LiOH show considerable anisotropic broadening as clearly observed from **Figure 2.4,** where the {101} reflection appears much broader compared to the {110} and {200} reflections. Analysis of the anisotropic

broadening using FullProf as described in the previous section results in platelet shaped LiOH crystallites with the platelet normal aligned with the c-lattice parameter, very similar to the Li$_2$O$_2$ crystallites. SEM images of LiOH (**Figure 2.1d**) show large grains, suggesting layered stacks of thin crystalline LiOH plates.

The evolution of the crystallite shape during the complete (dis)charge cycle is shown **Figure 2.5a**, and the evolution of the resulting D/T (diameter/thickness) aspect ratio, shown in **Figure 2.5b**. Consistent with the constant width of the XRD reflections during discharge, the aspect ratio and crystallite shape remains constant during discharge. This indicates that the average crystallite shape and size does not evolve during discharge, indicating continuous nucleation and growth of LiOH crystallites with a constant crystallite size distribution. This suggests a particle-by-particle nucleation and growth process, rather than concurrent growth of LiOH crystallites, where the latter would lead to an increase in average crystallite size. In contrast, **Figure 2.5a** shows that during charge the average crystallite dimensions increase significantly, see also supporting information **Figure S2.6**. Thereby the crystallite size evolution is highly asymmetric with respect to charge and discharge, indicating at a very different growth and decomposition mechanism. Since LiOH decomposition should reduce the crystallite size, and realizing the XRD results represent average crystallite sizes, this may be explained by preferential decomposition of the smallest LiOH crystallites which will increase the average crystallite size.

The evolution of the LiOH lattice parameters during discharge and charge are shown in **Figure 2.5c**. The *a*-lattice parameter remains practically constant during the complete discharge and charge cycle. In contrast, the *c*-parameter increases near the end of discharge and decreases at the early stages of charge after which it remains relatively stable until the end of charge. The crystallite size in the *c*-direction, parallel to the platelet normal, is on average approximately 20 nm during charge and discharge. For nanostructured metal oxides crystallite dimensions in the nano-range typically result in expansion of the lattice parameters, attributed to an increase in the surface energy due to larger exposed surfaces. As a consequence the *c*-lattice parameter in the vicinity of the surface typically expands.[45, 46] Because the average crystallite size does not change significantly during discharge, the increase in the *c*-lattice parameter must have a different origin than the crystallite size. One possibility is the presence of Li$^+$ or OH$^-$ vacancies, where the latter appears more relevant as the effect of OH$^-$ vacancies has been studied in Mg(OH)$_2$ and LiOH.[47, 48] In a LiOH crystal, the Li$^+$ ions are located around the apexes of a square which slightly fold downwards along a diagonal under the O atom of the OH$^-$ ion.[49] It is therefore likely that the presence of vacancies will affect the lattice parameters anisotropically. To investigate the dependence of the lattice parameters on the presence

of vacancies, DFT calculations were performed on a 2 × 2 × 2 supercell of LiOH by removing one hydrogen atom, lithium atom, and OH ion from the supercell resulting in H, Li and OH vacancies respectively (supporting information **Figure S2.7**). Relaxation of the supercell with a single hydrogen vacancy in the OH layer results in an increase of the *a*-lattice parameter and a decrease in the *c*-lattice parameter (supporting information **Table S2.1**). Upon relaxation of the supercell with either a Li or a OH vacancy, both structures show an increase in the *c*-lattice parameter (Li, ~1.12%; OH, ~2.60%, Table S1). However, the supercell shows a decrease in *a*-lattice parameter (~0.79%) for a Li vacancy and an increase (~1.05%) for a OH vacancy. Moreover, according to the DFT calculations[50, 51] the formation energy of Li, H, and OH$^-$ vacancies are -1.399, -0.317, and -1.578 eV, respectively, suggesting that the OH$^-$ vacancies are relatively stable in LiOH (supporting information **Theoretical Calculation** and **Table S2.1**). Hence, the observed increase in the LiOH *c*-lattice parameter and the slight increase in *a*-lattice parameter at the end of discharge seen in **Figure 2.5c** may be a consequence of the formation of OH vacancies in the LiOH lattice. This may be rationalized as follows; during the initial stages of discharge, H$_2$O will be relatively abundant resulting in the formation of LiOH crystallites with a low amount of OH vacancies. At the later stage of discharge most of the H$_2$O can be anticipated to be consumed, most likely the origin of the formation of OH sub-stoichiometric Li(OH)$_{1-x}$ crystallites, explaining the observed increase in *c*-lattice parameter. During the initial stages of charge the *c*-lattice parameter decreases, suggesting that the OH-vacancy rich Li(OH)$_{1-x}$ material is preferentially decomposed.

To investigate the cyclic formation of LiOH over multiple cycles, *operando* XRD was performed for the battery based on the DME-LiI electrolyte during three (dis)charge cycles, restricted to a capacity of 1.5 mAh at a current density of 0.3 mA/cm^2. The electrochemical curves for 3 cycles are shown in **Figure 2.6a** and the two-dimensional contour plots of the *operando* XRD patterns in **Figure 2.6b** demonstrate the cyclic formation and decomposition of LiOH crystallites during discharge and charge over three cycles. This gives direct evidence that LiOH is a cyclic discharge product in the presence of an LiI mediator over multiple cycles. Additionally, the linear increase (discharge) and decrease (charge) of the integrated area of the LiOH {101} and {110} reflections over three cycles as shown in the supporting information **Figure S2.8** also supports the formation and decomposition of crystalline LiOH during (dis)charge.
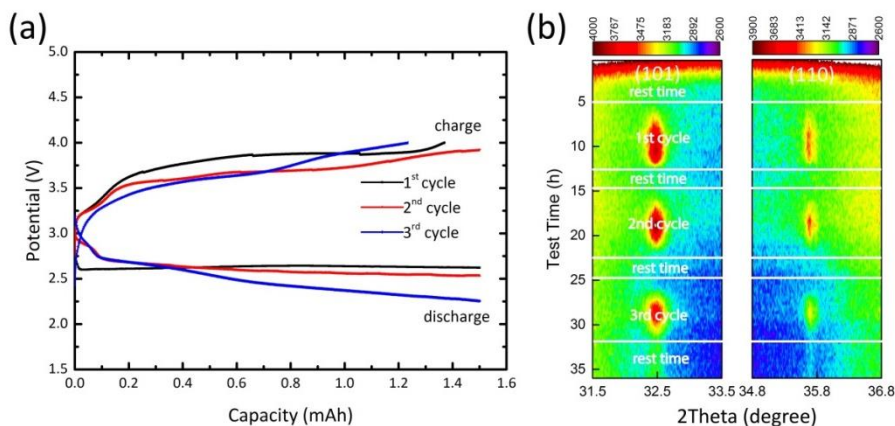
Figure 2.6. (a) Galvanostatic (dis)charge profiles, (b) two-dimensional contour plots of the operando XRD patterns showing the 2θ region between 31.5-33.5° and 34.8-36.8°, during three complete discharge-charge cycles demonstrating the LiOH formation ({101} and {110} reflections) and decomposition using the DME-LiI based electrolyte employing capacity restricted cycling capacity to 1.5 mAh at a current density of 0.3 mA/cm².

To explore the influence of H_2O on the formation of LiOH, the Li-O₂ battery, combining an activated carbon electrode and the DME-LiI electrolyte, was (dis)charged while exposing the cathode to H_2O saturated O₂. The (dis)charge curve obtained is shown in the supporting information **Figure 2.S9** where it is compared to that obtained for the same system exposed to dry O₂ (results shown in **Figure 2.5**). Due to the presence of H_2O in the provided O₂ gas, the discharge overpotential for the H_2O saturated O₂ battery is lower than its dry O₂ counterpart. Conversely, the charge overpotential for the H_2O saturated O₂ battery is larger, possibly due to the higher discharge capacity and associated increased resistance of the insulating LiOH crystallites and/or blocking of the gas diffusion electrode. The resulting *operando* XRD contour plots and the results from the Rietveld refinement of the LiOH structure are shown in the supporting information **Figures S2.10** and **S2.11** respectively. The evolution of the LiOH reflections in the presence of H_2O saturated O₂ is similar to that observed for the dry O₂ shown in **Figure 2.4**, indicating the formation and decomposition of crystalline LiOH. The main difference due to the presence of H_2O saturated O₂ is that the intensities of the LiOH reflections are larger and that the {101} reflection becomes sharper. These results indicate that bigger sized LiOH crystallites are generated during the discharge process due to the presence of H_2O saturated O₂. Both the apparent crystallite size and the lattice parameters evolve similar to that observed for dry O₂, also indicating that small LiOH crystallites are decomposed first during the charging process.

Summarizing, from the detailed refinement of the cyclic appearance of the XRD LiOH reflections in the DME-LiI electrolyte, a formation and decomposition mechanism is shown in **Figure 2.7a**. Based on the evolution of the apparent crystallite shape and the aspect ratio D/T of LiOH, the LiOH crystallites follow a continuous nucleation and growth mechanism with a constant crystallite size distribution during discharge. This mechanism represents a particle-by-particle rather than concurrent nucleation and growth process, forming the plate-like LiOH particles (**Figure 2.7b, images A-C**). Based on the simulation of defects, we expect that the small concentration of water in the electrolyte induces OH sub-stoichiometric LiOH explaining the observed increase in *c*-lattice parameter. During charge, the average LiOH crystallite dimensions increase significantly, whereas the aspect ratio and crystallite shape remain constant suggesting that the smallest OH deficient LiOH crystallites oxidize first (**Figure 2.7b, images D-F**). This indicates that the crystallite size and presence of vacancies are important parameters to consider when aiming for increasing the charge rate and decreasing the charge overpotential.
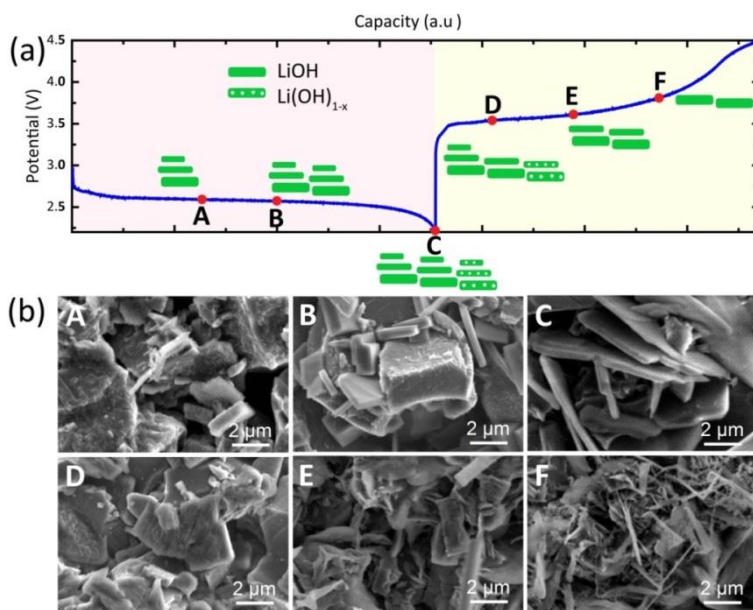
Figure 2.7. (a) Voltage profile including a schematic illustration of the formation and decomposition mechanism of the LiOH platelet shaped crystallites during the discharge and charge process as determined from refinement of the operando XRD patterns. (b) SEM images recorded at different capacity stages of LiOH formation and decomposition are depicted in panels A – F respectively.

2.4 Conclusions

Operando X-ray diffraction is performed to investigate the evolution structure of Li$_2$O$_2$ and LiOH during discharge and charge in the Li-O$_2$ battery employing a DME or DME-LiI electrolyte in combination with an activated carbon cathode. In the DME electrolyte, Li$_2$O$_2$ forms and decomposes reversibly as platelet crystallites with the normal of the platelet in the *c*-lattice parameter direction. During discharge the average Li$_2$O$_2$ crystallite shape becomes more isotropic due to the formation of more isotropic crystallites. The decomposition of Li$_2$O$_2$ crystallites during charging takes place into two distinct stages. First, amorphous species and small Li$_2$O$_2$ crystallites are oxidized and second, the larger crystallites are decomposed. In the DME-LiI electrolyte, LiI appears to act as a redox mediator resulting in the cyclic formation of crystalline LiOH over multiple cycles. During discharge, platelet LiOH crystallites form, with the normal of the platelet in the *c*-lattice parameter direction. As the average crystallite size and shape does not evolve during discharge, this indicates continuous, particle-by-particle nucleation and growth. The increase in the average *c*-lattice parameter is, based on DFT calculations, proposed to be a result of the formation of OH vacancies in LiOH, suggested to be the consequence of the depleting water in the DME electrolyte during LiOH formation. During decomposition on charge, the smallest OH deficient LiOH crystallite decomposes first, indicating that the decomposition of these particles is most facile. Providing H$_2$O saturated O$_2$ does not change the crystallite growth mechanism significantly, however, the amount of crystalline LiOH increases, consistent with the larger electrochemical discharge capacity.

References

1. Abraham, K. M.; Jiang, Z. *J. Electrochem. Soc.* **1996,** *143,* 1.

2. Bruce, P. G.; Freunberger, S. A.; Hardwick, L. J.; Tarascon, J. M. *Nat. Mater.* **2012,** *11,* 19.

3. Peng, Z.; Freunberger, S. A.; Chen, Y.; Bruce, P. G. *Science* **2012,** *337,* 563.

4. Thotiyl, M. M. O.; Freunberger, S. A.; Peng, Z.; Chen, Y.; Liu, Z.; Bruce, P. G. *Nat. Mater.* **2013,** *12,* 1050.

5. Freunberger, S. A.; Chen, Y.; Peng, Z.; Griffin, J. M.; Hardwick, L. J.; Barde, F.; Novak, P.; Bruce, P. G. *J. Am. Chem. Soc.* **2011,** *133,* 8040.

6. Thotiyl, M. M. O.; Freunberger, S. A.; Peng, Z.; Bruce, P. G. *J. Am. Chem. Soc.* **2012,** *135,* 494.

7.   Johnson, L.; Li, C.; Liu, Z.; Chen, Y.; Freunberger, S. A.; Ashok, P. C.; Praveen, B. B.; Dholakia, K.; Tarascon, J.-M.; Bruce, P. G.*Nat. Chem.* **2014,** *6,* 1091.

8.   Aetukuri, N. B.; McCloskey, B. D.; García, J. M.; Krupp, L. E.; Viswanathan, V.; Luntz, A. C. *Nat. Chem.* **2015,** *7,* 50.

9.   McCloskey, B. D.; Bethune, D. S.; Shelby, R. M.; Girishkumar, G.; Luntz, A. C. *J. Phys. Chem. Lett.* **2011,** *2,* 1161.

10.   McCloskey, B. D.; Scheffler, R.; Speidel, A.; Girishkumar, G.; Luntz, A. C. *J. Phys. Chem. C* **2012,** *116,* 23897.

11.   McCloskey, B. D.; Speidel, A.; Scheffler, R.; Miller, D. C.; Viswanathan, V.; Hummelshøj, J. S.; Nørskov, J. K.; Luntz, A. C. *J. Phys. Chem. Lett.* **2012,** *3,* 997.

12.   Gowda, S. R.; Brunet, A.; Wallraff, G. M.; McCloskey, B. D. *J. Phys. Chem. Lett.* **2013,** *4,* 276.

13.   Adams, B. D.; Black, R.; Radtke, C.; Williams, Z.; Mehdi, B. L.; Browning, N. D.; Nazar, L. F. *ACS Nano* **2014,** 8, 12483.

14.   Kundu, D.; Black, R.; Berg, E. J.; Nazar, L. F. *Energy Environ. Sci.* **2015**, *8,* 1292.

15.   Lu, J.; Lei, Y.; Lau, K. C.; Luo, X.; Du, P.; Wen, J.; Assary, R. S.; Das, U.; Miller, D. J.; Elam, J. W.; Albishri, H. M.; El-Hady, D. A.; Sun, Y.-K.; Curtiss, L. A.; Amine, K. *Nat. Commun.* **2013,** *4,* 2383.

16.   Feng, N.; He, P.; Zhou, H. *Adv. Energy Mater.* **2016**, *6,* 1502303.

17.   McCloskey, B. D.; Speidel, A.; Scheffler, R.; Miller, D. C.; Viswanathan, V.; Hummelshøj, J. S.; Nørskov, J. K.; Luntz, A. C. *J. Phys. Chem. Lett.* **2012,** *3,* 997.

18.   Itkis, D. M.; Semenenko, D. A.; Kataev, E. Y.; Belova, A. I.; Neudachina, V. S.; Sirotina, A. P.; Hävecker, M.; Teschner, D.; Knop-Gericke, A.; Dudin, P.; Barinov, A.; Goodilin, E. A.; Shao-Horn, Y.; Yashina, L. V. *Nano Lett.* **2013,** *13,* 4697.

19.   Grande, L.; Paillard, E.; Hassoun, J.; Park, J. B.; Lee, Y. J.; Sun, Y. K.; Passerini, S.; Scrosati, B. *Adv. Mater.* **2015,** *27,* 784.

20.   Meini, S.; Tsiouvaras, N.; Schwenke, K. U.; Piana, M.; Beyer, H.; Lange, L.; Gasteiger, H. A. *Phys. Chem. Chem. Phys.* **2013,** *15,* 11478.

21.   Schwenke, K. U.; Metzger, M.; Restle, T.; Piana, M.; Gasteiger, H. A. *J. Electrochem. Soc.* **2015,** *162,* A573.

22.   Wu, S.; Tang, J.; Li, F.; Liu, X.; Zhou, H. *Chem. Commun.* **2015,** *51,* 16860-16863.

23. Li, F.; Wu, S.; Li, D.; Zhang, T.; He, P.; Yamada, A.; Zhou, H. *Nat. Commun.* **2015,** 6.

24. Kwak, W.-J.; Hirshberg, D.; Sharon, D.; Shin, H.-J.; Afri, M.; Park, J.-B.; Garsuch, A.; Chesneau, F. F.; Frimer, A. A.; Aurbach, D.; Sun, Y.-K. *J. Mater. Chem. A* **2015,** 3, 8855.

25. Liu, T.; Leskes, M.; Yu, W.; Moore, A. J.; Zhou, L.; Bayley, P. M.; Kim, G.; Grey, C. P., Cycling Li-O₂ Batteries via LiOH Formation and Decomposition. *Science* **2015,** 350, 530.

26. Viswanathan, V.; Pande, V.; Abraham, K. M.; Luntz, A. C.; McCloskey, B. D.; Addison, D. *Science* **2016,** 352, 667.

27. Shen, Y.; Zhang, W.; Chou, S.-L.; Dou, S.-X. *Science* **2016,** 352, 667.

28. Burke, C. M.; Black, R.; Kochetkov, I. R.; Giordani, V.; Addison, D.; Nazar, L. F.; McCloskey, B. D. *ACS Energy Lett.* **2016**, 1, 747.

29. Ganapathy, S.; Adams, B. D.; Stenou, G.; Anastasaki, M. S.; Goubitz, K.; Miao, X.-F.; Nazar, L. F.; Wagemaker, M. *J. Am. Chem. Soc.* **2014,** 136, 16335.

30. Kang, S.; Mo, Y.; Ong, S. P.; Ceder, G. *Chem. Mater.* **2013,** 25, 3328.

31. Ganapathy, S.; Heringa, J. R.; Anastasaki, M. S.; Adams, B. D.; van Hulzen, M.; Basak, S.; Li, Z.; Wright, J. P.; Nazar, L. F.; van Dijk, N. H.; Wagemaker, M. *J. Phys. Chem. Lett.* **2016**, 3388.

32. Lim, H.; Yilmaz, E.; Byon, H. R. *J. Phys. Chem. Lett.* **2012,** 3, 3210.

33. Storm, M. M.; Johnsen, R. E.; Younesi, R.; Norby, P., Capillary Based Li-Air Batteries for in situ Synchrotron X-Ray Powder Diffraction Studies. *J. Mater. Chem. A* **2015,** 3, 3113-3119.

34. Xia, C.; Waletzko, M.; Chen, L.; Peppler, K.; Klar, P. J.; Janek, J. *ACS Appl. Mater. Interfaces* **2014,** 6, 12083.

35. Aetukuri, N. B.; McCloskey, B. D.; García, J. M.; Krupp, L. E.; Viswanathan, V.; Luntz, A. C. *Nat. Chem.* **2015,** 7, 50-56.

36. Griffith, L. D.; Sleightholme, A. E. S.; Mansfield, J. F.; Siegel, D. J.; Monroe, C. W. *ACS Appl. Mater. Interfaces* **2015,** 7, 7670.

37. Mitchell, R. R.; Gallant, B. M.; Shao-Horn, Y.; Thompson, C. V. *J. Phys. Chem. Lett.* **2013,** 4, 1060.

38. Black, R.; Lee, J.-H.; Adams, B.; Mims, C. A.; Nazar, L. F. *Angew. Chem.Int. Ed.* **2013,** 52, 392.

39. Adams, B. D.; Radtke, C.; Black, R.; Trudeau, M. L.; Zaghib, K.; Nazar, L. F. *Energy Environ. Sci.* **2013,** *6,* 1772.

40. Olivares-Marín, M.; Sorrentino, A.; Lee, R.-C.; Pereiro, E.; Wu, N.-L.; Tonti, D., Spatial *Nano Lett.* **2015,** *15,* 6932.

41. Lau, S.; Archer, L. A. *Nano Lett.* **2015,** *15,* 5995.

42. Black, R.; Oh, S. H.; Lee, J.-H.; Yim, T.; Adams, B.; Nazar *J. Am. Chem. Soc.* **2012,** *134,* 2902.

43. Oh, S. H.; Adams, B. D.; Lee, B.; Nazar, L. F. *Chem. Mater.* **2015,** *27,* 2322.

44. Rodríguez-Carvajal, J. Laboratoire Léon Brillouin (CEA-CNRS), CEA/Saclay, 2003, 91191.

45. Casas-Cabanas, M.; Rodriguez-Carvajal, J.; Canales-Vazquez, J.; Palacin, M. R. *J. Mater. Chem.* **2006,** *16,* 2925.

46. Leoni, M. *Sci. Forum* **2004,** 4*43-444,* 1.

47. Vaiss, V. S.; Borges Jr, I.; Wypych, F.; Leitão, A. A. *Chem. Phys.* **2013,** *418,* 1.

48. Tanigawa, H.; Tanaka, S. *J. Nucl. Sci. Technol.* **2001,** *38,* 1004.

49. Okazaki, S.; Ohtori, N.; Okada, I. *J. Chem. Phys.* **1990,** *92,* 7505.

50. Mérawa, M.; Labeguerie, P.; Ugliengo, P.; Doll, K.; Dovesi, R. *Chem. Phys. Lett.* **2004,** *387,* 453.

51. Varley, J. B.; Viswanathan, V.; Norskov, J. K.; Luntz, A. C. *Energy Environ. Sci.* **2014,** *7,* 720.

Supporting Information for Chapter 2

Fitting procedure microstructural parameters, methodology DFT calculations, evolution of the integrated XRD peak area, evolution of the average crystallite sizes, galvanostatic (dis)charge profiles during the *operando* XRD experiments, *operando* XRD patterns, lattice parameters resulting from DFT calculations.

Refinement of the microstructural parameters

Assuming that our observed anisotropic broadening is solely due to the microstructure effects, the XRD patterns at different (dis)charge states are refined with the FullProf program using the Thompson−Cox-Hasting pseudo−Voigt profile function including an anisotropic size-broadening model based on spherical harmonics where both instrumental and sample intrinsic profiles are supposed to be described approximately.[S2.1] The peak profiles and the resulting apparent crystallite shapes are average quantities. The crystallite shapes obtained are restricted by the symmetry of the crystal, which do not refer to the particle shape, but do represent the approximate average shape of the crystallites.

The cell parameters, scale factor, and background parameters were refined. The parameters constituting the instrumental resolution function (U, V, W) were obtained from a LaB6 standard sample. The full width at half maximum (FWHM) of the Gaussian (HG) and Lorentzian (HL) components of the peak profile have the following angular dependence:[S2.1]

$$H_G^2 = (U \tan \theta + V) \tan \theta + W + \frac{4 In2 \lambda^2}{\pi D_g^2 \cos^2 \theta}(\frac{180}{\pi})^2$$

$$H_L = X \tan \theta + \frac{2\lambda}{\pi D_l \cos \theta}(\frac{180}{\pi})$$

Where U, V, W, X, D_g, and D_l are the parameters which can be refined, D_g and D_l account for the Gaussian and Lorentzian components of size effects, respectively, X accounts for Lorentzian isotropic strain, V and W describe instrumental broadening, and U accounts for both Gaussian isotropic strain and instrumental contributions. In our case, the parameters constituting the instrumental resolution function (U, V, W) were obtained from a LaB6 standard (U =0.001821, V =-0.000809, W =0.001740) and were fixed during the refinement process.

Anisotropic size broadening can be described as a linear combination of spherical harmonics (SPH) model using the Scherrer formula. It is assumed that the anisotropic size only contributes to the Lorentzian component of the total Voigt function. The explicit formula of the intrinsic integral breadth using the SPH treatment of size broadening is given by:[S2.2]

$$\beta_h = \frac{\lambda}{D_h \cos \theta} = \frac{\lambda}{\cos \theta} \sum_{lmp} a_{lmp} y_{lmp} (\Theta_h, \Theta_h) \ .$$

Where β_h is the size contribution to the integral breadth of reflection (hkl), $y_{lmp} (\Theta_h, \Theta_h)$ are real spherical harmonics, and a_{lmp} are coefficients that can be refined, depending on the Laue class. In our case, the Laue groups of Li$_2$O$_2$ and LiOH are 6/mmm and 4/mmm, respectively, which are shown as follows.[S2.3-2.5]

Li$_2$O$_2$-6/mmm

$$\overline{R}_h = R_0^0 P_0^0(\Phi) + R_2^0 P_2^0(\Phi) + R_4^0 P_4^0(\Phi) + R_6^0 P_6^0(\Phi) + R_6^6 P_6^6(\Phi)\cos 6\varphi + \cdots,$$

LiOH-4/mmm

$$\overline{R}_h = R_0^0 P_0^0(\Phi) + R_1^0 P_2^0(\Phi) + R_2^0 P_4^0(\Phi) + R_3^0 P_4^4(\Phi)\cos 4\varphi + \cdots$$

A number of the terms can be determined by successive refinements starting from the isotropic case $\overline{R}_h = R_0^0$. The terms are then added one by one until the corresponding fitted coefficient becomes insignificant.

Theoretical calculation

First-principle calculations were performed using the Heyd-Scuseria-Ernzerhof (HSE) hybrid functional[S2.6, 2.7] as implemented in the Vienna Ab Initio Simulation Package (VASP)[S2.8] with the projector augmented wave (PAW) method[S2.9] due to its ability to accurately represent the lattice constants and the electronic properties of Li$_2$O$_2$ and LiOH.[S2.10] For all the calculations, a 48–atom supercell representing bulk LiOH, an energy cutoff of 600 eV, and a Γ−centered 5×5×4 k-point grid was employed. Ionic relaxation was performed until a 10^{-5} eV per formula unit difference in energy was obtained.

Since the protons are always coupled with oxygen to form hydrogen-bonded zig-zag chains $O - H \cdots O - H \cdots O - H$ in the LiOH crystallites[S2.11] as shown in **Figure S2.5,** OH vacancies rather than O only vacancies are assumed to occur. However, considering that the total energy of H is very small[S2.12], it is sufficient to describe the formation energy of OH vacancies as the absence of O. The formation energies of Li and O vacancies in charge state q at standard conditions in Li$_2$O$_2$ have been calculated as described in detail by Varley *et al.*,[S2.10] which revealed us to define Li, H and OH vacancies of charge state q in LiOH with the electrochemical process *via* the equilibrium reaction as follows:

(1) $LiOH \rightleftharpoons V_{Li}^{q} + Li + qe^{-}$

(2) $LiOH \rightleftharpoons V_{H}^{q} + 1/2H_{2} + qe^{-}$

(3) $LiOH \rightleftharpoons V_{o}^{q} + 1/2O_{2} + qe^{-}$
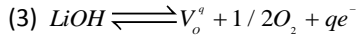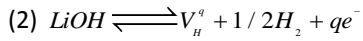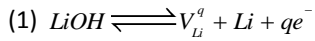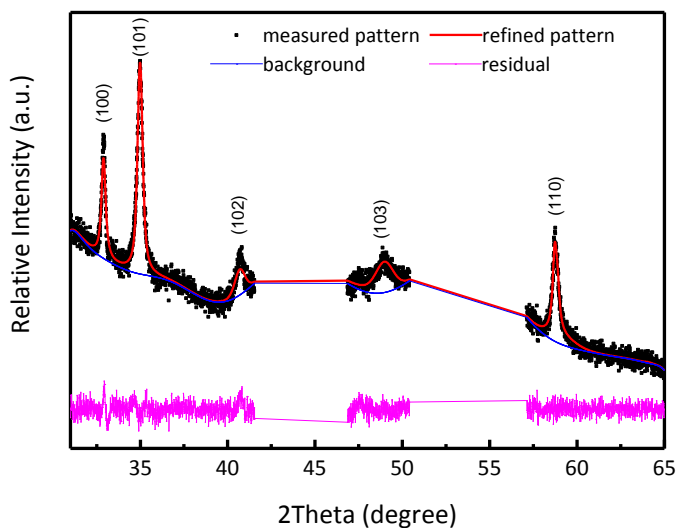
Figure S2.1. Experimental XRD pattern of Li_2O_2 on the electrode surface compared to the Rietveld refinement profile obtained using the FullProf program.
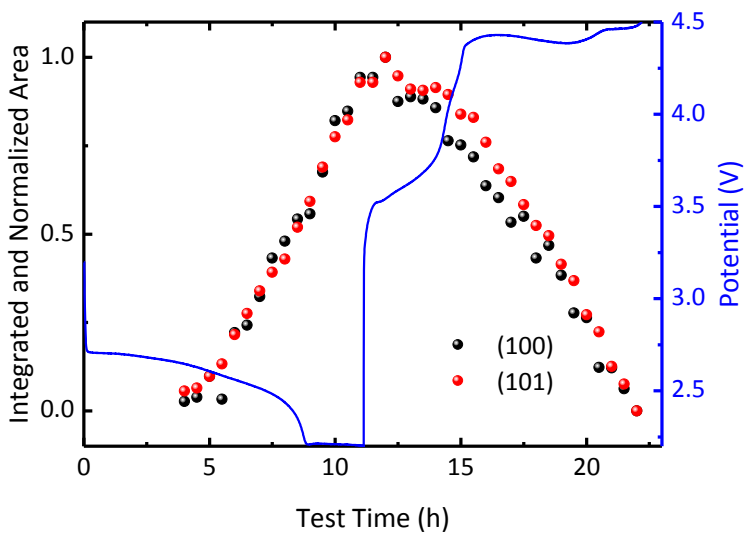
Figure S2.2. The evolution of the integrated and normalized area as a function of discharge time for the {100} and {101} reflections of Li_2O_2 during (dis)charge of a Li–O₂ battery in a DME based electrolyte at a current density of 0.3 mA/cm².
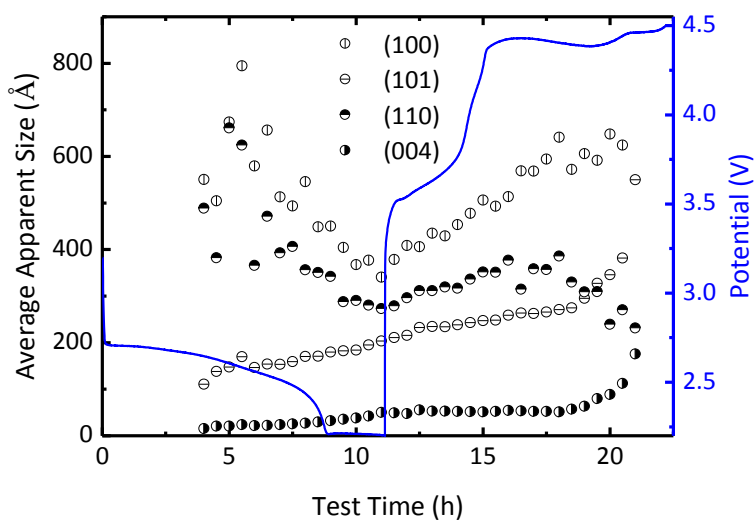
Figure S2.3. The average apparent size for individual XRD Li₂O₂ reflections resulting from Rietveld refinement, during the full galvanostatic (dis)charge cycle in a DME based electrolyte at a current density of 0.3 mA/cm².
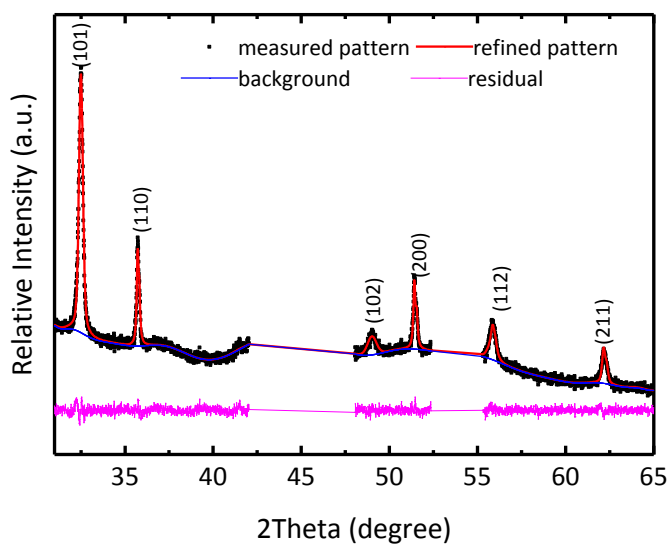
Figure S2.4. Experimental XRD pattern of LiOH on the electrode surface compared to the Rietveld refinement profile obtained using the FullProf program.
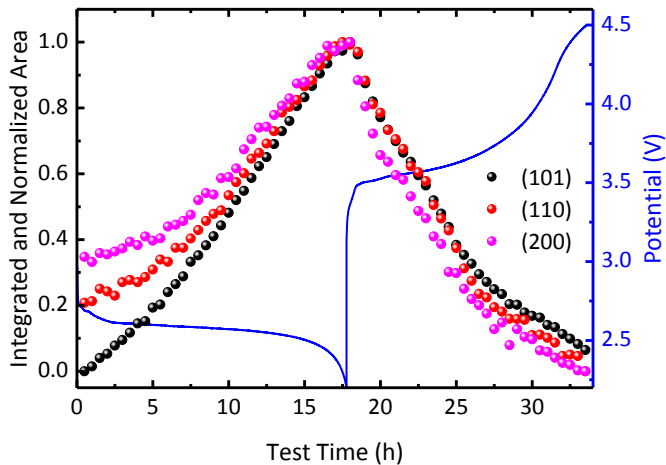
Figure S2.5. The evolution of the integrated and normalized area as a function of discharge time for {101}, {110} and {200} reflections of LiOH during (dis)charge in a DME/LiI based electrolyte at a current density of 0.3 mA/cm^2.
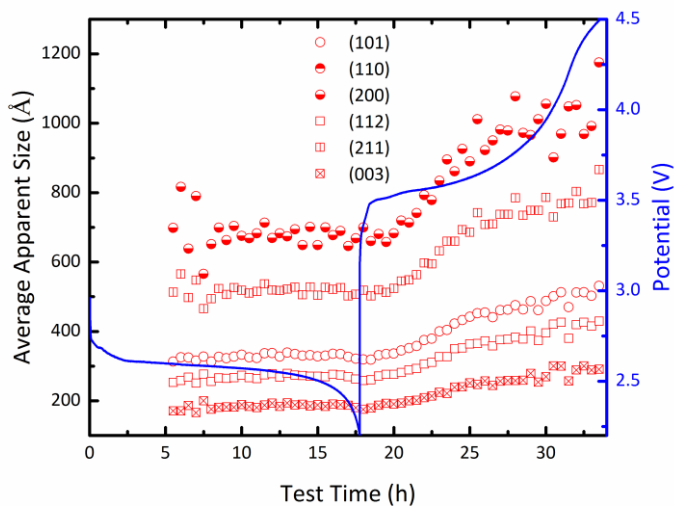
Figure S2.6. The evolution of the average apparent size for individual XRD LiOH reflections resulting from Rietveld refinement as a function of time during (dis)charge in a DME/LiI based electrolyte at a current density of 0.3 mA/cm^2.
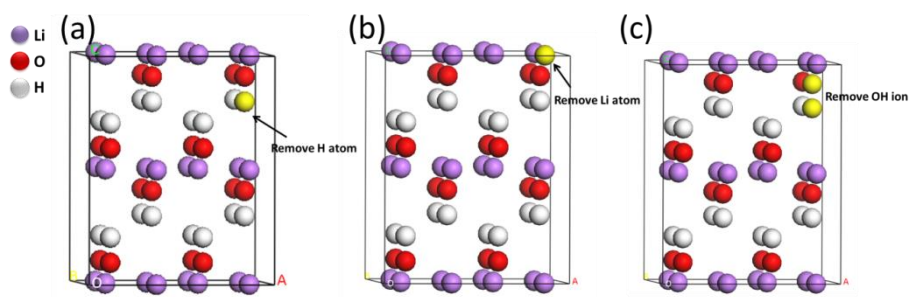
Figure S2.7. Models of super cells of LiOH with: (a) Hydrogen vacancy (b) Li vacancy and (c) OH vacancy.
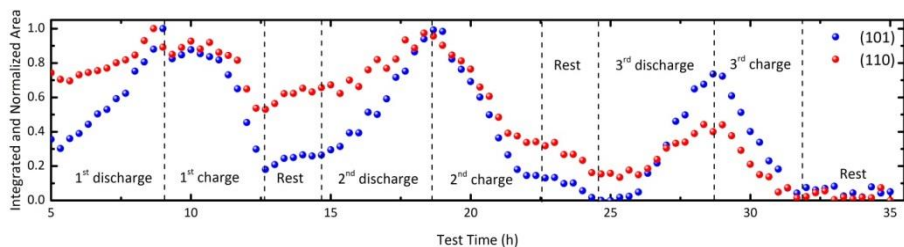
Figure S2.8. The evolution of the integrated and normalized area as a function of discharge time for {101} and {110} reflections of LiOH during (dis)charge in a DME/LiI based electrolyte employing capacity restricted cycling up to of 1.5 mAh at a current density of 0.3 mA/cm^2.
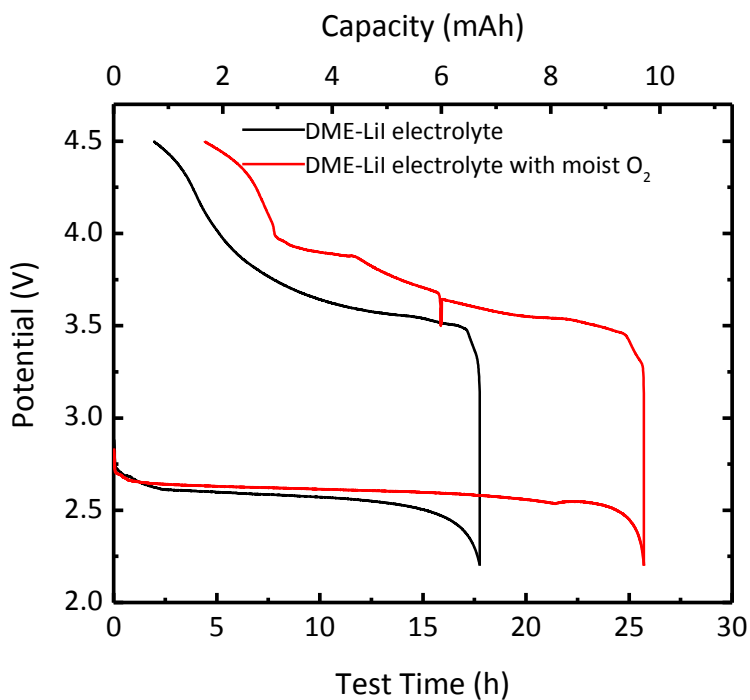
Figure S2.9. Galvanostatic (dis)charge profiles for the batteries with DME/LiI electrolytes with dry and moist O$_2$ respectively, in a 2.2 to 4.5 V voltage window versus Li/Li$^+$ at a current density of 0.3 mA/cm^2.
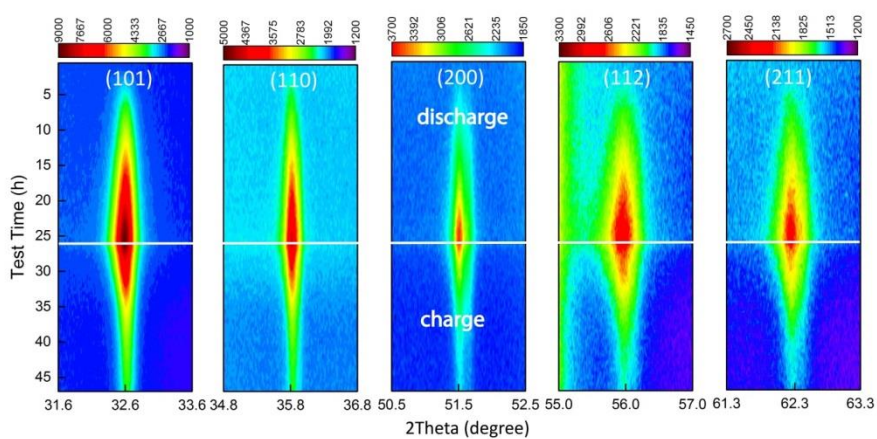
Figure S2.10. Two-dimensional contour plots of the operando XRD patterns showing the 2θ region between 31.6-33.6°, 34.8-36.8°, 50.5-52.5°, 55.0-57.0°, and 61.3-63.3°, during a complete (dis)charge cycle demonstrating the LiOH formation ({101}, {110}, {200}, {112}, and {211} reflections) and decomposition in the Li–O₂ battery using the DME/LiI based electrolyte with moist O₂ at a current density of 0.3 mA/cm².
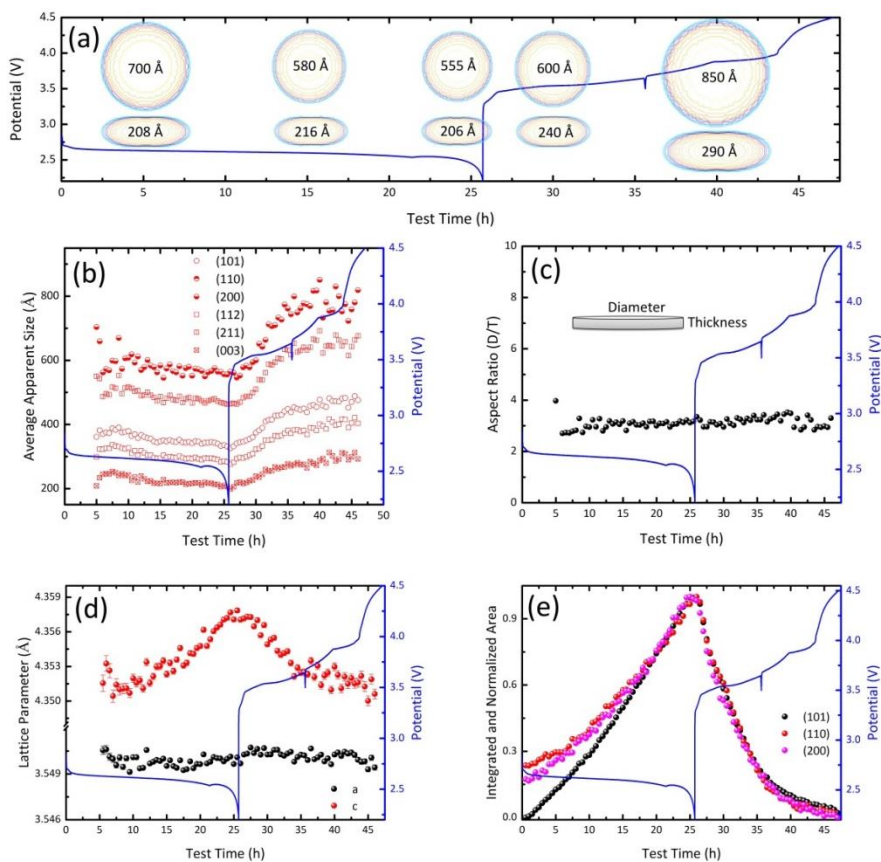
Figure S2.11. (a) The evolution of the LiOH crystallite shape, (b) the evolution the average apparent size, (c) the aspect ratio of the LiOH crystallite shape (diameter in the ab-plane/thickness in the c–direction), and (d) LiOH lattice parameters, resulting from Rietveld refinement as a function of time during the full galvanostatic (dis)charge cycle. (e) The evolution of the integrated and normalized area as a function of discharge time for {101}, {110} and {200} reflections of LiOH. The battery test was performed in a DME/LiI based electrolyte with moist O$_2$ at a current density of 0.3 mA/cm^2.

Table S2.1. Lattice parameters (2×2×2 supercell) and the total energy obtained from first-principle structural relaxation of the different compounds.

Systems	Lattice parameters (per unit cell)		Formation energy (per formula unit)(eV)
	a=b (Å)	c(Å)	
Experimental LiOH	3.548 to 3.549	4.350 to 4.359	-
Relaxed LiOH supercell	3.526	4.381	-19.144
LiOH with H vacancy	3.543	4.367	-18.715
LiOH with Li vacancy	3.498	4.430	-18.657
LiOH with OH vacancy	3.563	4.495	-18.020
Li	-	-	-1.886
O_2	-	-	-5.404
H_2	-	-	-1.492

References

S2.1. Rodríguez-Carvajal, J. Study of Microstructural Effects by Powder Diffraction Using the Program FULLPROF; Laboratorie Léon Brillouin (CEA-CNRS): Gif-sur-Yvette, France, 2003..

S2.2. Casas-Cabanas, M.; Palacín, M. R.; Rodríguez-Carvajal, J., Microstructural analysis of nickel hydroxide: Anisotropic size versus stacking faults. *Powder Diffr.* **2005,** 20, 334-344.

S2.3. Stephens, P., Phenomenological Model of Anisotropic Peak Broadening in Powder Diffraction. *J. Appl. Crystallogr.* **1999,** 32, 281-289.

S2.4. Popa, N. C.; Balzar, D., Size-broadening anisotropy in whole powder pattern fitting. Application to Zinc Oxide and Interpretation of the Apparent Crystallites in Terms of Physical Models. *J. Appl. Crystallogr.* **2008,** 41, 615-627.

S2.5. Popa, N., The (hkl) Dependence of Diffraction-Line Broadening Caused by Strain and Size for all Laue Groups in Rietveld Refinement. *J. Appl. Crystallogr.* **1998,** 31, 176-180.

S2.6. Zhang, W.; Chen, S.-J., Master Equation Approach to Finding the Rate-Limiting Steps in Biopolymer Folding. *J. Chem. Phys.* **2003,** 118, 3413-3420.

S2.7. Heyd, J.; Scuseria, G. E.; Ernzerhof, M., Erratum: "Hybrid functionals based on a screened Coulomb potential". *J. Chem. Phys.* **2006,** 124, 219906.

S2.8. Kresse, G.; Furthmüller, J., Efficiency of Ab-initio Total Energy Calculations for Metals and Semiconductors using a Plane-Wave Basis Set. *Comput. Mater.Sci.* **1996,** 6, 15-50.

S2.9. Pan, Y.; Zhang, H.; Shi, D.; Sun, J.; Du, S.; Liu, F.; Gao, H.-j., Highly Ordered, Millimeter-Scale, Continuous, Single-Crystalline Graphene Monolayer Formed on Ru (0001). *Adv. Mater.* **2009,** 21, 2777-2780.

S2.10. Varley, J. B.; Viswanathan, V.; Norskov, J. K.; Luntz, A. C., Lithium and Oxygen Vacancies and Their Role in Li$_2$O$_2$ Charge Transport in Li-O$_2$ Batteries. *Energy Environ. Sci.* **2014,** 7, 720-727.

S2.11. Hermann, A.; Ashcroft, N. W.; Hoffmann, R., Lithium Hydroxide, LiOH, at Elevated Densities. *J. Chem. Phys.* **2014,** 141, 024505.

S2.12. Mérawa, M.; Labeguerie, P.; Ugliengo, P.; Doll, K.; Dovesi, R., The Structural, Electronic and Vibrational Properties of LiOH and NaOH: An ab initio Study. *Chem. Phys. Lett.* **2004,** 387, 453-459.

Chapter 3

The Use of Nano Seed Crystals to Control Peroxide Morphology in a Non-Aqueous Li-O$_2$ Battery

This chapter is based on:
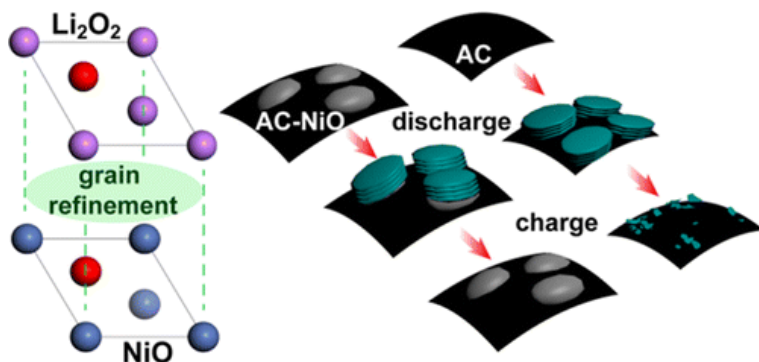
NiO nano seed crystal induced the growth of Li$_2$O$_2$ on its lattice facet. Owing to the similar lattice parameters between NiO and Li$_2$O$_2$, the Li$_2$O$_2$ crystalline is induced growth on the NiO nano seed, which is a more stable interface compared to that Li$_2$O$_2$ growth on the active carbon electrode, resulting in better electrochemical reversibility.

Abstract

The high theoretical energy density of Li-O$_2$ batteries as required for electrification of transport has pushed Li-O$_2$ research to the forefront. The poor cyclability of this system due to incomplete Li$_2$O$_2$ oxidation is one of the major hurdles to be crossed if it is ever to deliver a high reversible energy density. Here we present the use of nano seed crystallites to control the size and morphology of Li$_2$O$_2$ crystals. The evolution of the Li$_2$O$_2$ lattice parameters during operando X-ray diffraction shows that the rhombohedral NiO nanoparticles added to the activated carbon electrode act as seed crystals for equiaxed growth of Li$_2$O$_2$, while it can be seen from scanning electron microscopy energy-dispersive X-ray spectroscopy (SEM-EDX) elemental maps that the formation of Li$_2$O$_2$ occurs preferentially on the surface of NiO. Hence even small amounts, NiO (~5 wt%) particles act as preferential sites for Li$_2$O$_2$ nucleation, effectively reducing the average size of the primary Li$_2$O$_2$ crystallites and promoting crystalline growth. This is supported by first principle calculations, which predict a low interfacial energy for the formation of NiO-Li$_2$O$_2$ interfaces. The eventual cell failure appears to be the consequence of electrolyte side reactions indicating the necessity of more stable electrolytes. The control of the Li$_2$O$_2$ crystallite growth by the rational selection of appropriate nano seed crystals could be a promising strategy to improve the reversibility of Li-air electrodes.

3.1 Introduction

The promise of the Li-O$_2$[1,2] system as a possible replacement for gasoline in automotive applications has propelled battery research to the forefront.[3-5] The chemical reaction: $2Li + O_2 \rightleftarrows Li_2O_2$ represents the electrochemical processes that drive this battery, which in theory delivers an energy density of ~3,500 Wh/kg[3] However, there are several fundamental obstacles to be overcome before this battery system can work effectively. These include the high overpotentials observed during (dis)charge leading to low cycle energy efficiency,[2,6,7] slow kinetics due to poor electronic and ionic conductivity, and several side reactions involving the electrolyte and electrodes[8-11] leading to poor cyclability. Even if a stable electrolyte is found, capacity fading will occur as a consequence of the incomplete oxidation of the Li$_2$O$_2$ on charging,[12] as a consequence of the poor ionic and electronic conduction of Li$_2$O$_2$. Progressive buildup of inactive Li$_2$O$_2$ during repeated battery cycles, in addition to side product accumulation, eventually leads to cell failure. The main factors influencing the Li$_2$O$_2$ morphology, and consequentially cell capacity, are the current density[13] and the solubility of the LiO$_2$ intermediate.[14] Poor LiO$_2$ solubility by the electrolyte (low donor number) promotes the formation of a passivating Li$_2$O$_2$ film, even more pronounced by high current densities, leading to early cell death.[14] In contrast, good LiO$_2$ solubility (high donor number) dominantly leads to Li$_2$O$_2$ growth in solution before it is deposited on the electrode surface. A potential approach to mitigate the passivating formation of an amorphous Li$_2$O$_2$ film at high rates and in low donor electrolytes is to promote the formation of nano-sized Li$_2$O$_2$ crystallites at the electrode surface . A well-documented method to control grain size and prevent agglomeration is the addition of grain refining agents, a method frequently applied in metallurgy, aiming at better mechanical properties of metals and alloys.[15] Such grain refinement has also shown to be beneficial in metal hydride energy storage materials for enhancing the hydrogen sorption.[16,17] Grain refinement involves the addition of particles acting as substrates or seeds for heterogeneous nucleation also promoting equiaxed grain formation, which in the case of alloying competes with and therefore suppresses dendritic crystal nucleation and growth.[15] Mesoporous NiO sheets in its cubic crystalline form have already been demonstrated to work as a non-noble-metal based catalysts for the Li-O$_2$ battery system,[18-20] being active towards the decomposition of Li$_2$CO$_3$. NiO in its rhombohedral form however, has its a/b-lattice parameters (2.973 Å) close to that of Li$_2$O$_2$ (3.135 Å) which makes its doubly attractive for its added potential use as a grain refiner for Li-O$_2$ batteries. Here we show the preferential growth of Li$_2$O$_2$ on rhombohedral NiO in non-aqueous Li-O$_2$ cells when activated carbon (AC) electrodes are inoculated with this NiO. *Operando* X-ray diffraction (XRD) measurements supported by first principle calculations prove the formation of equiaxed Li$_2$O$_2$ grains with an a/b-parameter value tending to that

of NiO during discharge. Using increasing amounts of NiO seed crystals decreases the average Li$_2$O$_2$ crystallite sizes showing visible changes in the peroxide morphology. In addition at higher rates the preferential growth on the NiO promotes the formation of crystalline Li$_2$O$_2$, suppressing the formation of passivating amorphous Li$_2$O$_2$, and contributing towards better reversibility.

3.2 Material and methods

Rhombohedral NiO nanoparticles were prepared, starting from a nickel carbonate hydrate, as detailed in the supporting information section. Rietveld refinement of the XRD pattern resulted in NiO lattice parameters of a = b = 2.972 ± 0.001 Å and c = 7.158 ± 0.001 Å (supporting information, Figure S1). High-resolution transmission electron microscopy (HRTEM) images, (supporting information **Figures S3.2**), revealed crystalline grains with particle sizes between 5 – 10 nm. Gas diffusion electrodes of activated carbon (AC) alone, AC with 5% NiO (hereafter AC-NiO-1) and with 66.6% NiO (hereafter AC-NiO-2) were fabricated in exactly the same manner (supporting information) and used as cathodes in the Li-O$_2$ cells with a 1M lithium bis(trifluoromethanesulfonyl)-imide) (LiTFSI) in tetraethylene glycol dimethyl ether (TEGDME) electrolyte. Note that TEGDME is has a medium to high donor level, indicating that the Li2O2 formation is expected to take place both through formation in the solvent and directly on the electrode surface.[14]

3.3 Results and discussions

3.3.1 The structure and morphology evolution of the Li$_2$O$_2$ during (dis)charge

In order to follow the formation of crystalline Li$_2$O$_2$, *operando* XRD scans (each scan taking 67 minutes) were recorded during a complete galvanostatic (dis)charge cycle using AC-NiO-1 and AC electrodes at a current density of 50 μA/cm^2 in a specially designed Li-air cell.[21] Using the General Structure Analysis System (GSAS) program,[22] the diffraction data was fitted using the Rietveld method allowing us to determine the evolution of the lattice parameters and crystallite size, assuming only particle size broadening of Li$_2$O$_2$ during its formation and subsequent oxidation as a function of discharge-charge time. Interestingly, the evolution of the a/b-lattice parameters, shown in **Figure 3.1a,** is distinctly different between the AC-NiO-1 and AC electrodes during Li$_2$O$_2$ formation and subsequent decomposition. Compared to the AC electrode, the Li$_2$O$_2$ formed on the AC-NiO-1 electrode during the initial stages of discharge results in an a/b-lattice parameter that starts at a relatively small value *i.e.* 3.074 ± 0.004 Å, increasing to 3.129 ± 0.001 Å, at the end of discharge. In contrast to this, the a/b values of Li$_2$O$_2$ forming on the AC

electrode start at a 3.143 ± 0.002 Å decreasing to , 3.136 ± 0.0004 Å at the end of discharge. Assuming that smaller Li_2O_2 crystallites lead to the expansion of the lattice parameters,[21] as observed in some other crystalline metal oxide nanoparticles,[23,24] the higher initial values of the a/b-lattice parameter of Li_2O_2 in the AC-electrode indicates the initial formation of very small peroxide crystallites which, as discharge progresses, grow in size. The smaller lattice parameters of peroxide initially formed on the AC-NiO-1 electrodes can be attributed to the presence of NiO nanoparticles, which in their role as grain refiners; act as seeds for equiaxed Li_2O_2 growth.
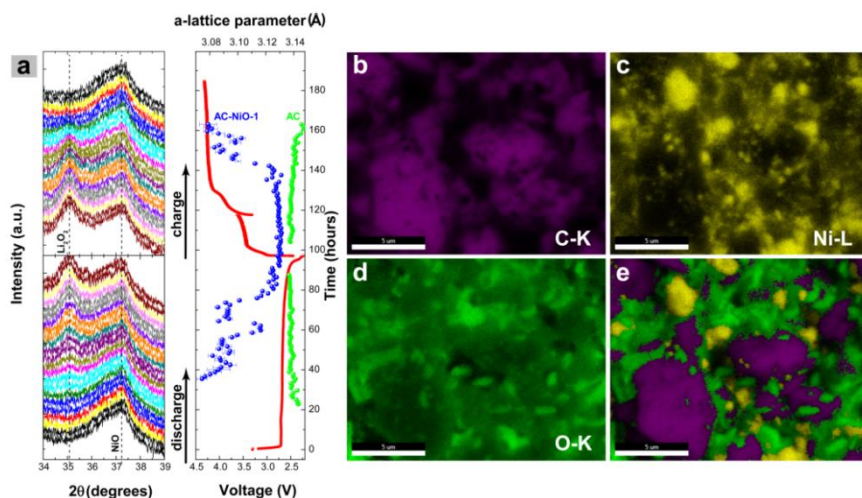
Figure 3.1 (a) Left: Section from every third XRD pattern recorded in-situ during the galvanostatic (dis)charge of the Li-O₂ cell containing an AC-NiO-1 cathode, showing the development of the (1 0 1) Li_2O_2 reflection. Right: Evolution of the Li_2O_2 a/b-lattice parameter as function of (dis)charge time. In addition the evolution of the Li_2O_2 a/b-lattice parameter in the AC electrode is shown at the same capacity. (b)-(e) SEM-EDX elemental mapping of a region of interest from an AC-NiO-2 electrode, completely discharged at a current density of 50 μA/cm² tot a 2.2 V cutoff, showing maps of (b) C (c) Ni (d) O and (e) overlay with purple = C; yellow = Ni; and green = O; The scale bar corresponds to 5 μm.

Also during the (dis)charge cycle the a/b-lattice parameters of the Li_2O_2 crystallites in the AC-NiO electrodes are significantly smaller compared to that in the AC electrode. This most likely reflects the confinement of the average a/b-lattice parameters induced by the smaller 2.9925 Å NiO a/b-lattice parameters. The deviation of the average a/b lattice parameters of the electrochemically formed Li_2O_2 when NiO is present unambiguously proves that the majority of the Li_2O_2 takes place on the NiO particles, resulting in equiaxed Li_2O_2 growth. To visualize Li_2O_2 on the surface of an electrode consisting of NiO at the end of discharge, scanning electron microscopy with energy-dispersive X-ray spectroscopy (SEM-EDX) was performed on electrodes of AC-NiO-2. The

high NiO content of this sample makes it easier to see the dispersed NiO, and yields elemental maps (**Figure 3.1b-e**) of the carbon and oxygen K-edges and the nickel L-edge. The elemental maps of the pristine AC-NiO-2 electrodes have been given in the supporting information section Figure S3. As can be clearly seen from **Figure 3.1e** the oxygen from Li$_2$O$_2$ is preferentially found on the parts of the electrode where Ni is present whereas the area of the electrode consisting predominantly of C remains mostly uncovered. This is in agreement with what we predict based on our observations from the *operando* X-ray diffraction measurements which indicate based on the lattice deviations of Li$_2$O$_2$ that it forms preferentially on the NiO present in the electrode, even when such said material is present in small amounts.

SEM images recorded at the end of discharge at a current density of 50 µA/cm^2 for the AC and AC-NiO-1 electrode have been shown in **Figure 3.2a and b** (supporting information **Figures S3.4 and S3.5**).[21] The corresponding electrochemistry has been given in the supporting information, and yields capacities of 2.2 mAh/cm^2 and 2.4 mAh/cm^2 for the AC and AC-NiO-1 electrodes respectively. It can be seen, specifically from the insets which depict a higher magnification, that there is a marked absence of the amorphous Li$_2$O$_2$ blanket on the AC-NiO-1 electrode surface (**Figure 3.2b**, inset) as has been previously reported by some of the authors for the AC electrode (**Figure 3.2a**). In addition the toroids of peroxide that form on the AC-NiO-1 electrode (**Figure 3.2b**) are more uniform in size in contrast to those that form on the AC electrode surface (**Figure 3.2a**) which shows a distribution of particles of Li$_2$O$_2$ from platelets to fully formed toroids, with a much higher density on the surface, despite the lower final capacity exhibited by this electrode. In order to better understand the effect on the peroxide formed by the addition of the NiO grain refiner, detailed ex-situ Rietveld analysis of the XRD patterns was performed on both AC-NiO-1 and AC electrodes after completely being discharged (2.2 V cut-off) at current densities ranging from 50 – 200 µA/cm^2. The (1 0 1) reflections are depicted in **Figure 3.2c** for both electrodes (the complete patterns and discharge curves are included in the Supporting Information Figures S6-S9). The first observation made is consistent with what has been reported elsewhere and is that the intensity and linewidth (FWHM) of the Li$_2$O$_2$ reflection for the AC cathodes could be directly correlated to the current density applied[13,21] which in turn determines the total capacity as seen from the upper panel in **Figure 3.2c** (supporting information **Figures S3.6 and S3.8**). In contrast, both the peak intensity and its FWHM were independent of the current density used for the Li$_2$O$_2$ formed on the AC-NiO-1 cathodes up to a current density of 150 µA/cm^2 (**Figure 3.2c**, lower panel). This was despite having slightly different discharge capacities *i.e.* 2.4, 2.3 and 2.2 mAh/cm^2 for current densities of 50, 100 and 150 µA/cm^2 respectively (supporting information **Figures S3.7 and S3.9**). This indicates that the amount of crystalline Li$_2$O$_2$

formed on the AC-NiO-1 cathodes is independent up to 150 μA/cm^2, despite of the decreasing total capacity at higher rate. Here we point the reader towards the use of the word crystalline peroxide only, since this by no means represents the total amount of peroxide formed which has been shown to have a combination of crystalline and amorphous morphologies. At 200 μA/cm^2 no crystalline peroxide peaks were visible both on the AC-NiO-1 and AC cathodes, which most likely indicate the formation of peroxide films[25] which are amorphous in nature on the cathode surface. This phenomenon of peroxide film formation at higher current densities, which limits the total capacity by premature surface passivation in combination with low donor number electrolyte solvents has been described in detail elsewhere.[13,14,26] Even at current densities exceeding 200 μA/cm^2 a small fraction of crystalline Li$_2$O$_2$ that forms on the NiO seed crystals competes with the formation of amorphous Li$_2$O$_2$ films and is barely perceptible with XRD (**Figure 3.2c**, supporting information **Figure S3.7**). Its presence can be ascertained by a comparison of the charge voltage profiles measured at these rates. The extended sloping region of the voltage profile at lower potentials observed during charge for the AC electrode (dis)charged at 200 μA/cm^2 (supporting information, **Figure S3.10**), has been attributed to the oxidation of amorphous Li$_2$O$_2$ films.[13,27,28] The charge profile of the AC-NiO-1 electrode (dis)charged at the same rate is markedly different, with the sloping region at higher potentials, followed by a plateau at 4.25 V corresponding to the oxidation of the residual crystalline fraction of Li$_2$O$_2$ as well as the oxidation of the organic and inorganic species present which has been demonstrated to occur in this voltage region.[10,29] This further suggests that the presence of NiO influences *only* the nature of the Li$_2$O$_2$ promoting the formation of crystalline Li$_2$O$_2$.

A comparison of the peak widths of the (1 0 1) and (1 1 0) reflections of the crystalline Li$_2$O$_2$ formed on the AC and AC-NiO-1 cathodes after 50 μA/cm^2 discharge, shown in **Figure 3.2d**, reveals a distinct difference in crystallite coherence length. This indicates a different anisotropic crystallite size forming on the AC-NiO-1 as compared to the AC electrodes. Where the broadening of the (1 0 1) Li$_2$O$_2$ reflection is nearly the same for the two cathodes, the broadening of the (1 1 0) reflection is considerably larger for the AC-NiO-1 compared to NiO free cathodes. Assuming that the broadening of the reflections is solely due to particle size broadening, the anisotropic broadening of AC cathodes confirms the platelet shape of the Li$_2$O$_2$ crystallites that make up the toroidal particles previously found with SEM/TEM[12,30,31] and I X-ray diffraction.[21] The additional broadening of the (1 1 0) reflection induced by the presence of NiO indicates that average crystallite size and anisotropy in the AC-NiO-1 cathodes is smaller compared to that of the Li$_2$O$_2$ formed in the AC cathodes. To quantify this the diffraction patterns were refined using an anisotropic size-broadening based on spherical harmonics as implemented in the

FulProf[32,33] Rietveld refinement program.[34] This resulted in coherence lengths of 28.5 nm and 10.3 nm for the (1 0 1) and (1 1 0) reflections for Li_2O_2 formed on the AC-NiO-1 cathode, significantly smaller compared to 42.3 nm and 11.7 nm of the Li_2O_2 forming on the AC cathode. These dimensions most likely correspond to the primary platelet Li_2O_2 particles which build up the toroids. This indicates that the NiO acts as a grain refiner decreasing the sizes of the primary crystallites of Li_2O_2 during formation.
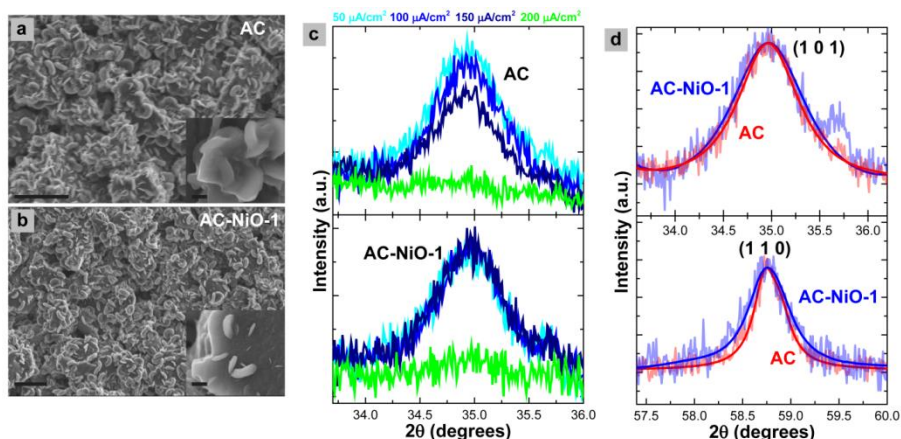
Figure 3.2 (a) and (b) Scanning electron microscopy (SEM) images recorded at the end of discharge with a current density of 50 μA/cm² of the AC and AC-NiO-1 cathodes respectively. The scale bar represents 5 μm. The insets represent images taken at higher magnifications with a 200 nm scale bar. (c) The Li_2O_2 (1 0 1) XRD reflections of the AC and AC-NiO-1 cathodes at the end of complete discharge for different current densities. (d) The Li_2O_2 (1 0 1) and (1 1 0) reflections including the corresponding Rietveld refinements of the AC (blue) and AC-NiO-1 (red) cathodes after discharge at a current density of 50 μA/cm².

3.3.2 Electrochemical cycling

The presence of a considerable amount of activated carbon in the AC-NiO-1 electrode and to a lesser extent in the AC-NiO-2 electrode inherently precludes the possibility of attaining excellent reversibility when these electrodes are used in a Li-O₂ battery despite the demonstrated efficacy of NiO as a grain refiner, due to the inevitable build of side products as a consequence of the presence of the high surface carbon. **Figure 3.3a and b** shows the first cycle voltage profile of the AC, AC-NiO-1, and AC-NiO-2, measured at a current density of 100 μA/cm² applying lower and upper voltage limits of 2.2 V and 4.5 V. Realistic comparison of currents and specific capacities in terms of mAh/g*carbon* or mAh/cm² is difficult given the variety in gas diffusion electrodes (dimension, coating thicknesses, carbon/active material loading, porosity, actual surface areas) and the restricted peroxide formation on the surface of the gas diffusion electrode. To be as complete and consistent as possible we report our results in capacities both geometrically

(in mAh/cm^2) and gravimetrically (in mAh/g$_{carbon+NiO}$). For AC-NiO-2, consisting primarily of NiO, the discharge process corresponding to the oxygen reduction reaction (ORR) occurs at an average of 2.6 V (**Figure 3.3b**), while the ORR of both the AC and AC-NiO-1 cathodes occurs at ~2.65V. During the charge process, (oxygen evolution reaction, OER), the onset of the sloping region of the charge curve for AC-NiO-2 occurs just above 3 V, which is very close to the thermodynamically expected value of 2.959 V[35] for Li$_2$O$_2$ decomposition. For the AC-NiO-1 electrode this occurs at 3.3 V which is still slightly lower (~ 100 mV) than that observed for the pure AC electrode. The total capacity at the end of discharge of AC-NiO-2, corresponding to 100% capacity in **Figures 3.3b** results in the geometrical capacity of ~0.65 mAh/cm^2 and to a gravimetrical capacity of ~220 mAh/g$_{(carbon+NiO)}$. This relatively low capacity can be attributed to the lower surface area of NiO, which forms 66% of this electrode (supporting information). The total capacity of the AC-NiO-1 and AC cathodes, corresponding to 100% capacity in **Figure 3.3a**, reaches to the geometrical capacity of 2.1 – 2.2 mAh/cm^2 and geometrical capacity of 1000 mAh/g$_{(carbon+NiO)}$. Using the protocol developed by McCloskey and co-workers,[36] the yield of Li$_2$O$_2$ after a set discharge was determined using an Iodometric titration (details in the supporting information). The AC and AC-NiO-1 cathodes yielded 60.3% and 73.7% of Li$_2$O$_2$ respectively at for a fixed capacity discharge of 1 mAh, confirming that most of the capacity is due to the formation of Li$_2$O$_2$.
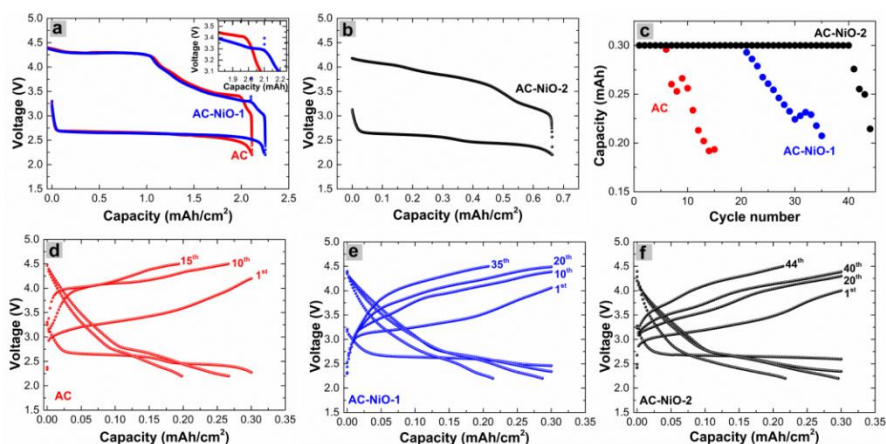
Figure 3.3 (a) and (b) Galvanostatic (dis)charge profile for the first cycle of AC/AC-NiO-1 and AC-NiO-2 electrodes measured at a current density of 100 μA/cm^2 respectively. (c) Restricted capacity cycling performance of AC-NiO-1/2 and AC electrodes at a current density of 100 μA/cm^2. The cut-off capacity was set 0.3 mAh/cm^2. (Dis)charge voltage profiles of the AC (d)AC-NiO-1 (e) and AC-NiO-2 (f) electrodes for restricted capacity cycling.

To monitor the reversibility of the electrochemical process, the batteries were cycled to full (supporting information Figure S11) and a restricted capacity of 0.3 mAh as

seen in **Figure 3.3c and d**. The AC-NiO-1/2 electrodes have improved capacity retention upon restricted capacity cycling compared to the AC electrodes. The AC-NiO-1 electrode completely regains its discharge capacity on charge for more than 20 cycles, while the AC-NiO-2 electrode retains its capacity for 40 cycles (**Figure 3.3d**). A closer look at the AC-NiO-2 voltage profiles during oxidation of Li_2O_2 (**Figure 3.3f**) shows that a majority of the charge process occurs below 4V, even up to 20 cycles, though progressive cycling leads to an increasing fraction of the voltage curve exceeding 4 V. This is also reflected, albeit to a lesser extent in the voltage profiles of the AC-NiO-1 electrodes (**Figure 3.3e**) as a consequence of its higher carbon content. We anticipate that this is due to aforementioned oxidation of side products that form during the discharge process resulting in the buildup of carbonate and formate species among others as well as the progressive degradation of the electrolyte, increasing the internal resistance as we continue cycling.[36-38]
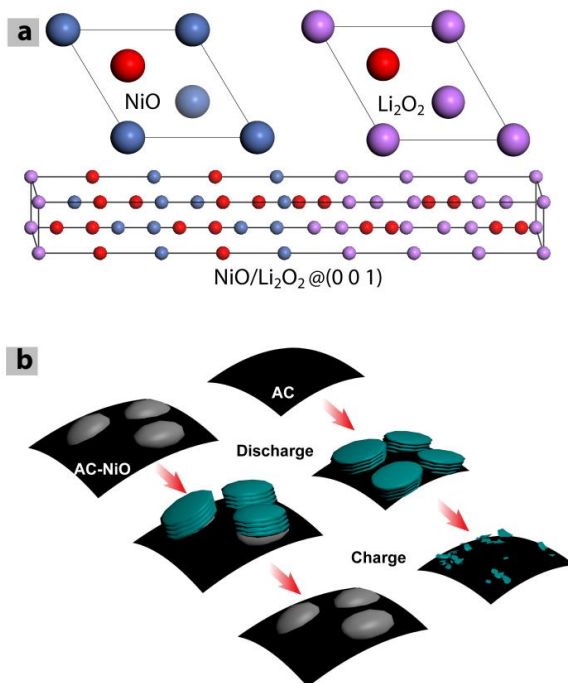
Figure 3.4 (a) Unit cells of NiO and Li_2O_2 showing the (0 0 1) facet and the layered structure of NiO/Li_2O_2, with the interface along (0 0 1). (b) A cartoon, depicting possible differences between Li_2O_2 formation and oxidation on AC-NiO and AC electrodes respectively.

3.3.3 DFT calculations of the NiO-Li$_2$O$_2$ interface

Using DFT calculations we have determined that the interface energy[39] for the equiaxed formation of (0 0 1) Li$_2$O$_2$ on the (0 0 1) facet of NiO is ~0.156 eV/Å^2 (**Figure 3.4a**, details in the supporting information). This relatively small value, smaller compared to other known coherent interfaces[40][39] indicates that the energy penalty for the formation of a coherent interface between NiO and Li$_2$O$_2$ at the (0 0 1)/(0 0 1) interfacial plane is very low. Also using DFT it has been shown that the (0 0 1) facet of Li$_2$O$_2$ is the lowest energy surface, consequently the most dominant in the Wulff shape, occupying over 60 % of the crystalline facets,[28,41,42] consistent with the present observation of equiaxed growth in the (0 0 1) direction. We anticipate that as discharge progresses the average a/b value increases due to the formation of crystalline peroxide on non-NiO sites, and due to the stacking and growth of the plate-like Li$_2$O$_2$ crystallites to form toroidal particles (**Figure 3.4b**). Nevertheless, at the end of discharge the average a/b-lattice parameter of the Li$_2$O$_2$ formed in the AC-NiO-1 electrode remains smaller than that of peroxide forming on AC. Consistently with equiaxed growth in the (0 0 1) direction no major differences are observed between the evolution of the c-lattice parameter of Li$_2$O$_2$ on the AC-NiO-1 and AC electrodes, indicating that the stacking of the Li$_2$O$_2$ takes place along the c-axis. This is also in agreement with the slight broadening observed in the (1 0 1) reflection of Li$_2$O$_2$ that forms on the AC-NiO-1 electrode, in contrast to the broadening observed in the (1 1 0) reflection, indicating that the growth in the c-direction, is unperturbed by the presence of the NiO seed crystals.

3.4 Discussion and conclusions

Because TEGDME has a medium to high donor level Li$_2$O$_2$ formation is expected to take place both through formation in the solvent and directly on the electrode surface.[14] The NiO can be expected in particular to influence the Li$_2$O$_2$ formation on the electrode surface. The observed increased crystallinity, and equiaxed growth on the NiO indicates that the NiO helps to prevent the formation of a passivating amorphous Li$_2$O$_2$ film, increasing crystalline Li$_2$O$_2$ capacity and cycle life. The observed average changes in the Li$_2$O$_2$ lattice parameters suggest that a relatively large fraction of the Li$_2$O$_2$ formed upon discharge is affected by the NiO. An interesting question is to what extend the in solution formed Li$_2$O$_2$ particles are influenced by the NiO, which may strongly depend on their particle size in solution. From the changes observed in the peroxide crystallite dimensions and a/b-lattice parameters upon NiO addition, it is revealed that the presence of NiO affects the morphology and growth of Li$_2$O$_2$ grains due to equiaxed growth of the peroxide on the NiO, resulting in an improvement of the reversibility of peroxide formation and oxidation on partial (dis)charge. An added advantage of preferential Li$_2$O$_2$

growth on the NiO surfaces may be the absence of a direct contact and possible reactions between the peroxide and the carbon cathode. This is advantageous compared to carbon-only electrodes, that are known to be reactive especially with superoxide- like lithium sub-stoichiometric $Li_{2-x}O_2$ present in amorphous lithium peroxide forming on high surface area carbons.[21,25] The resulting lithium carbonate buildup[43,44] irreversibly alters the nature of the gas-diffusion electrode surface. While the use of non-carbon gas diffusion electrodes is by no means untried,[2,45-48] their use has been primarily in the cadre of a catalyst or redox-mediator. The presence of a grain refiner, in addition to defining sites for preferential Li_2O_2 nucleation and growth, prolonging the cyclability of the Li-O$_2$ cell, additionally allows us to alter the nature of Li_2O_2 as it forms. This concept taken a step further, by the use of epitaxial thin films of NiO would allow directed growth of Li_2O_2 allowing the double benefit of the complete elimination of carbon while at the same time attaining control over their shape and morphology of Li_2O_2 as it forms. It is anticipated that this mechanism mainly effects the surface growth of Li_2O_2 as promoted by poorly LiO_2 solvating electrolytes (low donor number), thereby mitigating at least partially the poor capacity retention of this type of electrolytes. The presented grain refiner strategy motivates further research in materials that can act as seed crystal while at the same time catalyzing the Li-air redox reactions, preventing side reactions combined with good electronic conductivity.

References

1. Abraham, K. M.; Jiang, Z. *J. Electrochem. Soc.* **1996**, *143*, 1.

2. Peng, Z.; Freunberger, S. A.; Chen, Y.; Bruce, P. G. *Science* **2012**, *337*, 563.

3. Bruce, P. G.; Freunberger, S. A.; Hardwick, L. J.; Tarascon, J. M. *Nat. Mater.* **2012**, *11*, 19.

4. Black, R.; Adams, B.; Nazar, L. F. *Adv. Energy Mater.* **2012**, *2*, 801.

5. Christensen, J.; Albertus, P.; Sanchez-Carrera, R. S.; Lohmann, T.; Kozinsky, B.; Liedtke, R.; Ahmed, J.; Kojic, A. *J. Electrochem. Soc.* **2012**, *159*, R1.

6. Lu, Y. C.; Gallant, B. M.; Kwabi, D. G.; Harding, J. R.; Mitchell, R. R.; Whittingham, M. S.; Shao-Horn, Y. *Energy Environ. Sci.* **2013**, *6*, 750.

7. Lee, J. H.; Black, R.; Popov, G.; Pomerantseva, E.; Nan, F.; Botton, G. A.; Nazar, L. F. *Energy Environ. Sci.* **2012**, *5*, 9558.

8. McCloskey, B. D.; Bethune, D. S.; Shelby, R. M.; Girishkumar, G.; Luntz, A. C. *J. Phys. Chem. Lett.* **2011**, *2*, 1161.

9. McCloskey, B. D.; Scheffler, R.; Speidel, A.; Girishkumar, G.; Luntz, A. C. *J. Phys. Chem. C* **2012**, *116*, 23897.

10. McCloskey, B. D.; Speidel, A.; Scheffler, R.; Miller, D. C.; Viswanathan, V.; Hummelshøj, J. S.; Nørskov, J. K.; Luntz, A. C. *J. Phys. Chem. Lett.* **2012**, *3*, 997.

11. Gowda, S. R.; Brunet, A.; Wallraff, G. M.; McCloskey, B. D. *J. Phys. Chem. Lett.* **2013**, *4*, 276.

12. Mitchell, R. R.; Gallant, B. M.; Thompson, C. V.; Shao-Horn, Y. *Energy Environ. Sci.* **2011**, *4*, 2952.

13. Adams, B. D.; Radtke, C.; Black, R.; Trudeau, M. L.; Zaghib, K.; Nazar, L. F. *Energy Environ. Sci.* **2013**, *6*, 1772.

14. Johnson, L.; Li, C.; Liu, Z.; Chen, Y.; Freunberger, S. A.; Ashok, P. C.; Praveen, B. B.; Dholakia, K.; Tarascon, J.-M.; Bruce, P. G. *Nat Chem* **2014**, *6*, 1091.

15. Murty, B. S.; Kori, S. A.; Chakraborty, M. *Int. Mater. Rev.* **2002**, *47*, 3.

16. Singh, S.; Eijt, S. W. H.; Huot, J.; Kockelmann, W. A.; Wagernaker, M.; Mulder, F. M. *Acta Mater.* **2007**, *55*, 5549.

17. Mulder, F. M.; Singh, S.; Bolhuis, S.; Eijt, S. W. H. *J. Phys. Chem. C* **2012**, *116*, 2001.

18. Qiu, D.; Bu, G.; Zhao, B.; Lin, Z.; Pu, L.; Pan, L.; Shi, Y. *Mater. Lett.* **2015**, *141*, 43.

19. Hong, M.; Choi, H. C.; Byon, H. R. *Chem. Mater.* **2015**, *27*, 2234.

20. Tong, S.; Zheng, M.; Lu, Y.; Lin, Z.; Li, J.; Zhang, X.; Shi, Y.; He, P.; Zhou, H. *Journal of Materials Chemistry A* **2015**, *3*, 16177.

21. Ganapathy, S.; Adams, B. D.; Stenou, G.; Anastasaki, M. S.; Goubitz, K.; Miao, X. F.; Nazar, L. F.; Wagemaker, M. *J. Am. Chem. Soc.* **2014**, *136*, 16335.

22. Larson, A. C.; Von Dreele, R. B. *General Structure Analysis System (GSAS)*, Los Alamos National Laboratory, 2004.

23. Diehm, P. M.; Ágoston, P.; Albe, K. *ChemPhysChem* **2012**, *13*, 2443.

24. Xu, J.; Harmer, J.; Li, G.; Chapman, T.; Collier, P.; Longworth, S.; Tsang, S. C. *Chem. Commun.* **2010**, *46*, 1887.

25. Yang, J.; Zhai, D.; Wang, H. H.; Lau, K. C.; Schlueter, J. A.; Du, P.; Myers, D. J.; Sun, Y. K.; Curtiss, L. A.; Amine, K. *Phys. Chem. Chem. Phys.* **2013**, *15*, 3764.

26. Gallant, B. M.; Kwabi, D. G.; Mitchell, R. R.; Zhou, J.; Thompson, C. V.; Shao-Horn, Y. Energy *Environ. Sci.* **2013**, *6*, 2518.

27. Lu, J.; Lei, Y.; Lau, K. C.; Luo, X.; Du, P.; Wen, J.; Assary, R. S.; Das, U.; Miller, D. J.; Elam, J. W.; Albishri, H. M.; El-Hady, D. A.; Sun, Y.-K.; Curtiss, L. A.; Amine, K. *Nat. Commun.* **2013**, *4*.

28. Radin, M. D.; Rodriguez, J. F.; Tian, F.; Siegel, D. J. *J. Am. Chem. Soc.* **2012**, *134*, 1093.

29. Black, R.; Lee, J. H.; Adams, B.; Mims, C. A.; Nazar, L. F. *Angew. Chem., Int. Ed.* **2013**, *52*, 392.

30. Mitchell, R. R.; Gallant, B. M.; Shao-Horn, Y.; Thompson, C. V. *J. Phys. Chem. Lett.* **2013**, *4*, 1060.

31. Black, R.; Oh, S. H.; Lee, J. H.; Yim, T.; Adams, B.; Nazar, L. F. *J. Am. Chem. Soc.* **2012**, *134*, 2902.

32. Rodríguez-Carvajal, J. *Phys. B (Amsterdam, Neth.)* **1993**, *192*, 55.

33. Roisnel, T.; Rodríguez-Carvajal, J. Mater. Sci. Forum **2001,** *378,* 118

34. Popa, N. C. *J. Appl. Crystallogr.* **1998**, *31*, 176.

35. Garcia-Araez, N.; Novák, P. *J. Solid State Electrochem.* **2013**, *17*, 1793.

36. McCloskey, B. D.; Valery, A.; Luntz, A. C.; Gowda, S. R.; Wallraff, G. M.; Garcia, J. M.; Mori, T.; Krupp, L. E. *J. Phys. Chem. Lett.* **2013**, *4*, 2989.

37. Freunberger, S. A.; Chen, Y.; Peng, Z.; Griffin, J. M.; Hardwick, L. J.; Barde, F.; Novak, P.; Bruce, P. G. *Journal of the American Chemical Society* **2011**, *133*, 8040.

38. Adams, B. D.; Black, R.; Williams, Z.; Fernandes, R.; Cuisinier, M.; Berg, E. J.; Novak, P.; Murphy, G. K.; Nazar, L. F. *Adv. Energy Mater.* **2015,** *5,* 1400867.

39. Wagemaker, M.; Mulder, F. M.; van der Ven, A. *Adv. Mater.* **2009**, *21*, 1.

40. Mooij, L. P. A.; Baldi, A.; Boelsma, C.; Shen, K.; Wagemaker, M.; Pivak, Y.; Schreuders, H.; Griessen, R.; Dam, B. *Adv. Energy Mater.* **2011**, *1*, 754.

41. Nicola, S. *Nanotechnology* **2009**, *20*, 445703.

42. Wulff, G. *Z. Kristallogr.* **1901**, *34*, 449.

43. Itkis, D. M.; Semenenko, D. A.; Kataev, E. Y.; Belova, A. I.; Neudachina, V. S.; Sirotina, A. P.; Hävecker, M.; Teschner, D.; Knop-Gericke, A.; Dudin, P.; Barinov, A.; Goodilin, E. A.; Shao-Horn, Y.; Yashina, L. V. *Nano letters* **2013**, *13*, 4697.

44. Thotiyl, M. M. O.; Freunberger, S. A.; Peng, Z.; Bruce, P. G. *J. Am. Chem. Soc.* **2012**, *135*, 494.

45. Chen, Y.; Freunberger, S. A.; Peng, Z.; Fontaine, O.; Bruce, P. G. *Nat Chem* **2013**, *5*, 489.

46. Thotiyl, M. M. O.; Freunberger, S. A.; Peng, Z.; Chen, Y.; Liu, Z.; Bruce, P. G. *Nat Mater* **2013**, *12*, 1050.

47. Zhao, G.; Mo, R.; Wang, B.; Zhang, L.; Sun, K. *Chemistry of Materials* **2014**, *26*, 2551.

48. Kundu, D.; Black, R.; Berg, E. J.; Nazar, L. F. *Energy Environ. Sci.* **2015,** *8,* 1292.

Supporting Information for Chapter 3

Materials and Methods

Nickel Oxide synthesis: The rhombohedral phase of NiO was obtained by heating nickel carbonate basic hydrate (99.9% trace metal basis, Sigma Aldrich) to 1200 ^{o}C for 24 h under ambient air after which it was slowly cooled. The obtained product was tested with X-ray diffraction (XRD) and the resulting pattern was fit with the General Structure Analysis System (GSAS) program[S3.1] using the Rietveld method to verify the phase of the material (Figure S3.1). This material was further nanosized by ball milling. Five cycles, each comprising a 5-minute milling process at 500 rpm followed by a 20-minute rest period was performed. Further XRD and TEM analysis and refinement showed that the resultant NiO nanoparticles had an average domain size of 5-10 nm.

Electrode preparation and Electrochemistry: Gas diffusion electrodes (cathodes) were prepared, with Activated Carbon (AC, Kuraray Chemical) and with Activated Carbon containing NiO nanoparticles (with AC:NiO weight ratios of 95:5 (AC-NiO-1) and 33.3:66.6 (AC-NiO-2) respectively) and a lithiated Nafion®[S3.2, 3.3] binder in N-Methyl-2-pyrrolidone (NMP, Aldrich).The mixture of AC-NiO was ball milled at a low speed of 100 rpm to ensure proper contact between AC and NiO. Slurries of AC and the AC-NiO mixtures and binder (90:10 by weight) were cast on carbon paper (Spectracarb 2050a). These cathodes were further dried under vacuum at 100 °C for 24 h to remove all traces of surface adsorbed water, upon which discs 11 and 19 mm in diameter were punched out. The final mass of AC/AC-NiO-1 on carbon paper was ~ 2 – 3 mg/cm^2 while that of AC-NiO-2 on carbon paper was ~4 – 5 mg/cm^2. The electrolyte used was a solution of 1M lithium bis(trifluoromethanesulfonyl)imide (LiTFSI, Aldrich) dissolved in dried and distilled tetraethylene glycol dimethyl ether (TEGDME, <5 ppm H$_2$O, Aldrich). Batteries comprising a cathode, glass microfiber separator (Whatman) soaked with electrolyte and a Li-metal anode were assembled in a glove box (Argon, O$_2$ and H$_2$O < 0.1 ppm) in our home-built cells for non-aqueous Li-O$_2$ batteries, as well as in our special cells for *operando* X-ray diffraction.[S3.4] Once connected to O$_2$ (Linde, 99.995%) the cell was allowed to equilibrate for 2 – 6 h under an O$_2$ pressure of 1.2 bar. Galvanostatic (dis)charge cycles were performed using a MACCOR 5300 battery cycler.

XRD measurements: X-ray diffraction measurements were performed during the operation of a Li-O$_2$ cell using a PANalytical X'Pert Pro PW3040/60 diffractometer with Cu Kα radiation operating at 45kV and 40 mA in an angular 2θ range of 31 – 66°. Each scan was 67 minutes long. Rietveld refinement of the diffraction data was performed using the aforementioned GSAS program. Several variables including the lattice parameters, peak

broadening and anisotropy (if present) and occupancies were fit, assuming the vibrational spectrum remained constant. Peaks arising from the aluminum mesh and carbon paper were excluded from the fits to enable a more accurate fit of the zero-position of the diffraction patterns.

TEM measurements: For preparing the TEM samples, the NiO sample was ultrasonicated in acetone for 30 minutes before dispersing on a standard TEM Cu-grid. TEM measurements were carried out in a Cs corrected TITAN microscope operating at 300 KV.

SEM measurements: Morphology of the discharged cathodes were characterized using Hitachi 4800S scanning electron microscope with cold FEG electron gun operated at 5 kV. SEM_EDX measurements were performed on a FEI Nova NanoSEM 450 equipped with EDAX TEAM operating at 15 kV.

Theoretical calculations: First-principle calculations were performed using the Heyd–Scuseria–Ernzerhof (HSE)[S3.5, 3.6] hybrid functional as applied in the Vienna Ab-Initio simulation package (VASP)[S3.7] with the projector augmented wave (PAW) method,[S3.8] because of its demonstrated ability to describe the electronic properties of Li_2O_2.[S3.9] The energy cut-off was set to 600 eV, along with convergence criteria of 10^{-4} eV/formula unit for ionic relaxation. In order to determine the excess energy that would occur as a result of an interface between periodic regions of NiO and Li_2O_2 the following protocol was employed. Two slabs with the in-plane interfacial dimensions of 2.967 Å × 2.967 Å and 3.070 Å × 3.070 Å were constructed consisting of periodic regions of (0 0 1) NiO and (0 0 1) Li_2O_2. The relaxed slab lengths of 29.9 Å (2.967 Å × 2.967 Å) and 30.5 Å (3.070 Å × 3.070 Å) were determined in the direction perpendicular to the interface. Additionally ionic relaxation was performed such that the total energy convergence was below 10^{-4} eV. In order to avoid contributions from elastic energy which would arise as a result of enforced strain the following method was employed. For the cells representing the bulk contributions of NiO and Li_2O_2, the cell parameters in the plane of the interface *i.e.* a/b parameters were fixed to the same values as that for the interface used in the slab (2.967 or 3.070 Å), while only the cell parameter in the direction perpendicular to the interface was relaxed. As a result when the bulk energy was subtracted from the interface slab energy, it was ensured that the energy arising as a result of elastic strain was also subtracted. The interface energy was determined to be 0.156 eV/Å² for the 2.967 Å × 2.967 Å interface and 0.22 eV/Å² for the 3.070 Å × 3.070 Å interface respectively.

Li₂O₂ titration: We followed the protocol for Li_2O_2 titration that has been described in detail the article published by McCloskey and co-workers.[S3.10] Cathodes were extracted

from the battery in the argon filled glove box, where they were transferred into glass vials and the tops were closed off with a tightly wrapped parafilm layer. These sealed bottles were taken out of the glove box, where they were injected with 2 – 3 mL of ultrapure water using a syringe. After shaking vigorously, the contents of the bottle were transferred to a 50 mL Erlenmeyer flask, where the base formed was titrated against a standardized 0.005M HCl (Sigma-Aldrich) solution using a drop of phenolphthalein (Sigma-Aldrich) in alcohol as the end-point indicator. After this, three reagents were added in quick succession. First, 1 mL of a 2 wt% KI (≥99.5 %, Sigma-Aldrich) solution in H$_2$O, followed by 1 mL of 3.5 M H$_2$SO$_4$ solution, followed finally by 50 μL of a molybdate-based catalyst solution. The molybdate-based catalyst solution was prepared by combining 1 g of ammonium molybdate (Sigma-Aldrich) with 10 mL of 6N NH$_4$OH (Sigma-Aldrich), to which 3 g of ammonium nitrate (≥98 %, Sigma-Aldrich) was added after which the mixture was diluted to 50 mL using ultrapure H$_2$O. Upon addition of these reagents, the solution in the flask turns yellow due to the formation of I$_2$ which is subsequently titrated against a standardized solution of 0.01 N Na$_2$S$_2$O$_3$ (Sigma-Aldrich) to a faint straw color. At this point ~0.5 mL a 1% starch solution (Sigma-Aldrich) is added as an end-point indicator turning the solution a deep blue, and the solution is further titrated until the solution turns colorless.

Iodometric titrations performed on commercially purchased Li$_2$O$_2$ powder (Sigma-Aldrich, 90% purity) with 1 mg of Li$_2$O$_2$ dissolved in 3 mL of ultrapure water yielded a Li$_2$O$_2$ purity of 83.1 ± 1.5% over three titrations, which gives an approximate percentage error of 6 - 8 % per titration. The percentage yield of Li$_2$O$_2$ was determined by dividing the amount of Li$_2$O$_2$ titrated (A), by the amount of Li$_2$O$_2$ that would be expected if a 2.0 e$^-$ per Li$_2$O$_2$ reaction occurred during discharge (B). For a 1 mAh discharge capacity, theoretically 18.65 μmols of Li$_2$O$_2$ would be expected to be formed.

Description of the specific capacity: Given the variety in dimension, coating thicknesses, carbon/active material loading, porosity, and actual surface areas reported for gas diffusion electrodes in literature, a realistic comparison of currents used and specific capacities in terms of mAh/g$_{carbon}$ or mAh/cm^2 becomes difficult. Given what is now known about the formation of peroxide and how its formation is restricted to the surface of the gas diffusion electrode as well as to allow a consistent comparison between capacities obtained with our own cathodes, with and without NiO seed crystals, we have reported all our results in terms of specific capacities per cm^2 (mAh/cm^2).

***Note on the total surface area of AC-NiO-1 and AC-NiO-2:*** The Activated Carbon (YP-50F, Kurary Chemicals, Japan) used for our electrodes has a high total surface area of 1500-1800 m^2/g. This corresponds to a roughly estimated 2 nm particle size. The NiO particles

are on average, 2 to 5 times larger than the AC particles so the AC-NiO-2 electrodes, which contain 30% NiO have a lower surface area than the AC-NiO-1 electrodes.
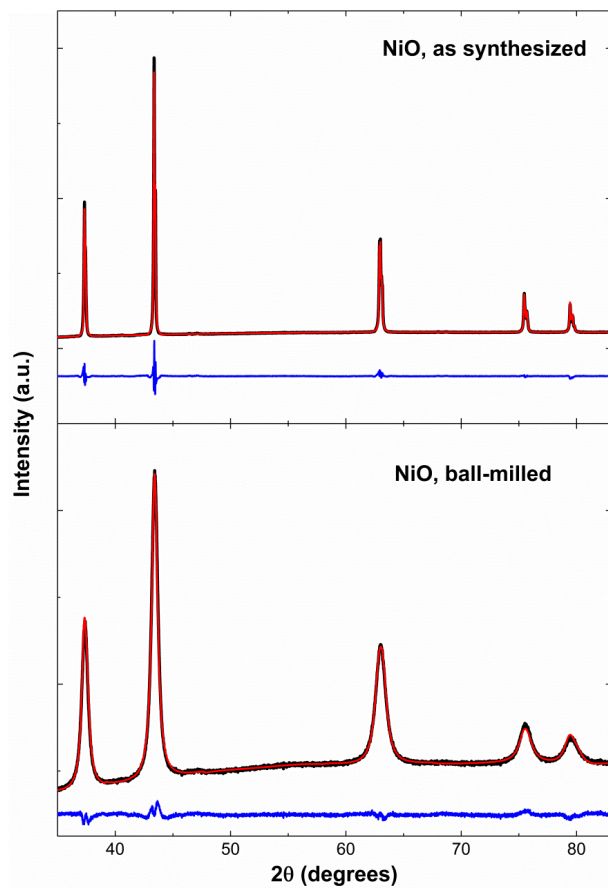
Figure S3.1 XRD patterns with corresponding Rietveld refinement of as synthesized and ball milled NiO. The black line represents the pattern as measured, the red line the fit and the blue line the difference.

50 nm

5 nm
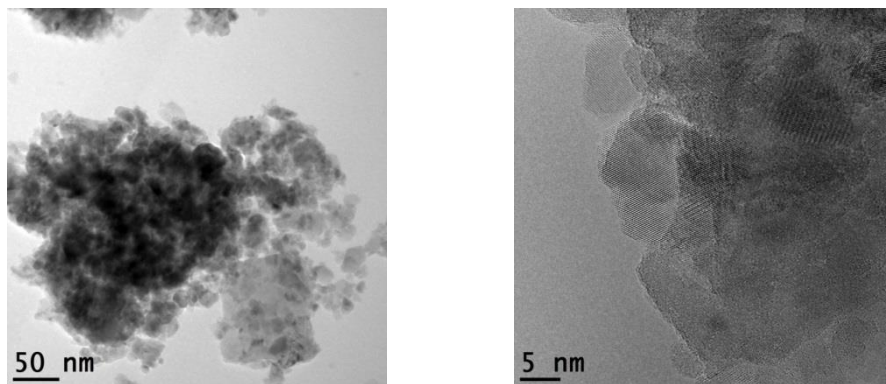
Figure S3.2 TEM image of the agglomerate of NiO nanoparticles.

a — 20 um — C-K

b — 20 um — Ni-L

c — 20 um — O-K

d — 20 um
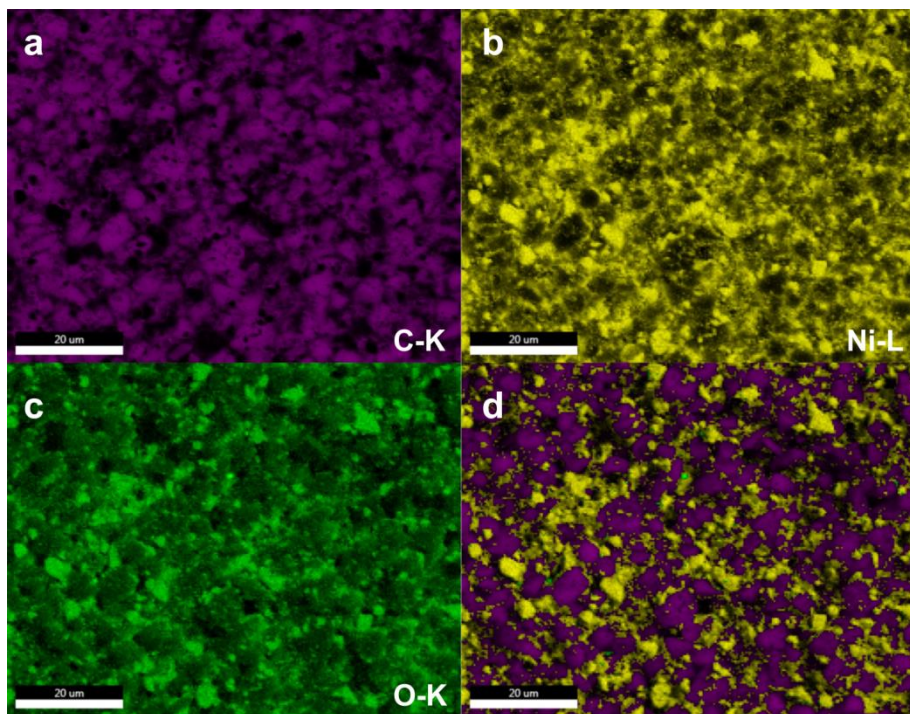
Figure S3.3 SEM-EDX elemental mapping of a pristine AC-NiO-2 electrode showing maps of (a) C (b) Ni (c) O and (d) overlay with purple = C; yellow = Ni; and green = O; The scale bar corresponds to 20 μm.
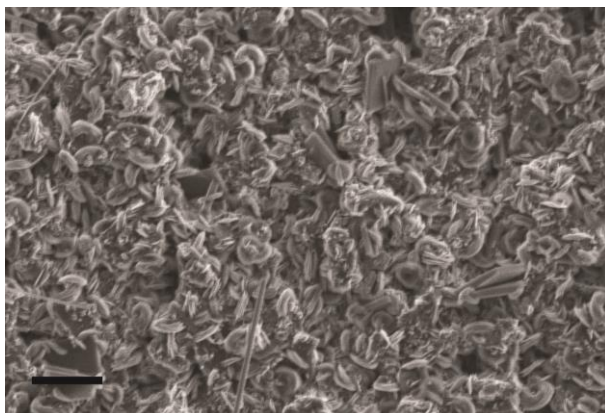
Figure S3.4 Scanning electron microscopy (SEM) images recorded at the end of discharge with a current density of 50 μA/cm² of the AC-NiO-2 cathode. The scale bar represents 5 μm.
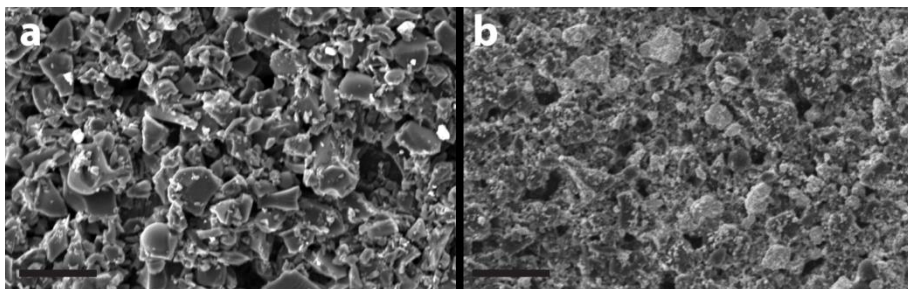
Figure S3.5 Scanning electron microscopy (SEM) images recorded of the pristine (a) AC-NiO-1 and (b) AC-NiO-2 cathodes. The scale bar represents 10 μm.
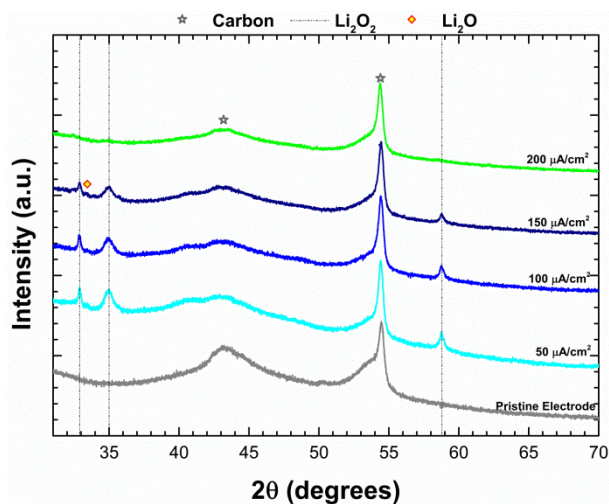
Figure S3.6 Full XRD patterns of AC electrodes completely discharged at different current densities.
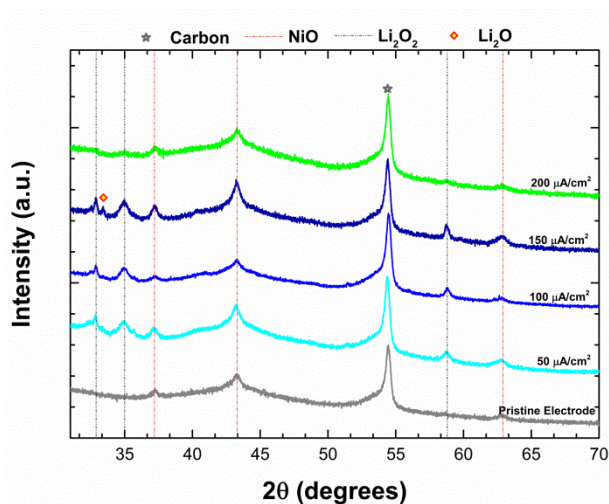
Figure S3.7 Full XRD patterns of AC-NiO-1 electrodes completely discharged at different current densities.
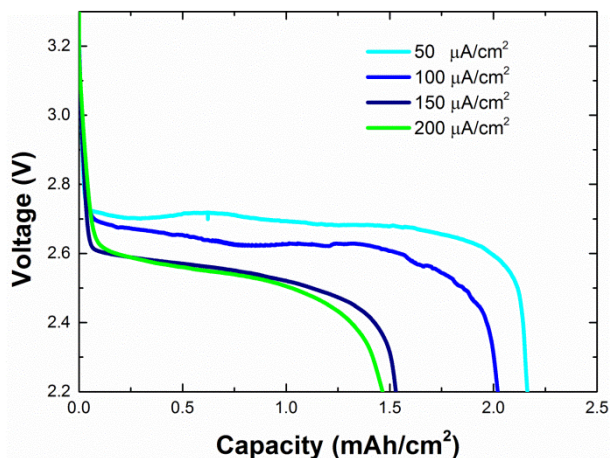
Figure S3.8 Galvanostatic discharge profiles of the AC electrodes in a Li-O$_2$ cell at current densities of 50 – 200 µA/ cm^2 (lower voltage cut-off set at 2.2 V).
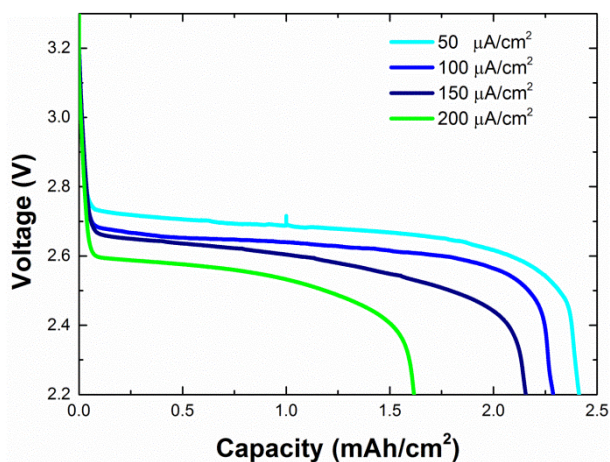
Figure S3.9 Galvanostatic discharge profiles of the AC-NiO-1 electrodes in a Li-O$_2$ cell at current densities of 50 – 200 µA/ cm^2 (lower voltage cut-off set at 2.2 V).
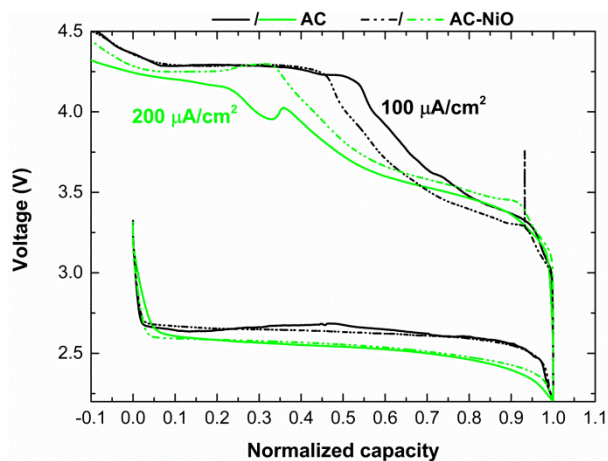
Figure S3.10 Full galvanostatic (dis)charge profiles of the AC-NiO-1 and AC electrodes in a Li-O₂ cell at current densities of 100 μA/cm^2 and 200 μA/ cm^2 (lower and upper voltage cut-offs set at 2.2 and 4.5 V) with their total capacities normalized to 1.
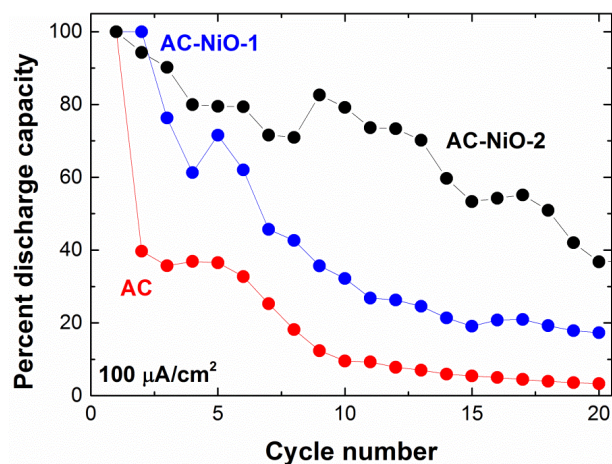
Figure S3.11 Full and capacity cycling performance of AC-NiO-1/2 and AC electrodes at a current density of 100 μA/cm^2. High and low voltage cutoff of 4.5 V and 2.2 V were set.
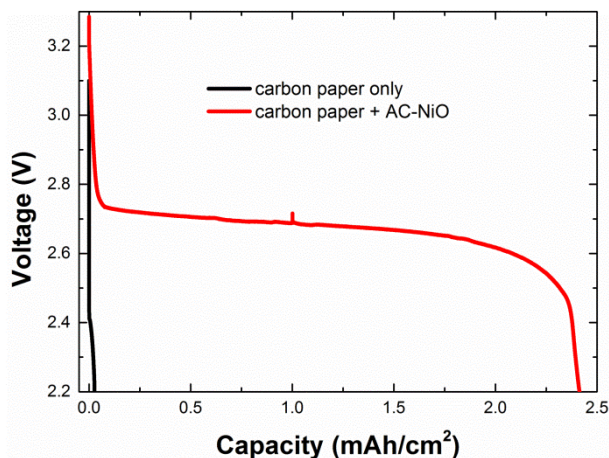
Figure S3.12 Galvanostatic discharge profiles of carbon paper and carbon paper coated with the AC-NiO mixture at a current density of 50 µA/cm² in a Li-O₂ cell.

References

S3.1. A. C. Larson and R. B. Von Dreele, *General Structure Analysis System (GSAS)*, Los Alamos National Laboratory, Los Alamos, NM 87545, 2004.

S3.2. R. R. Garsuch, D. B. Le, A. Garsuch, J. Li, S. Wang, A. Farooq and J. R. Dahn, *J. Electrochem. Soc.*, 2008, **155**, A721-A724.

S3.3. B. D. Adams, C. Radtke, R. Black, M. L. Trudeau, K. Zaghib and L. F. Nazar, *Energy Environ. Sci.*, 2013, **6**, 1772-1778.

S3.4. S. Ganapathy, B. D. Adams, G. Stenou, M. S. Anastasaki, K. Goubitz, X. F. Miao, L. F. Nazar and M. Wagemaker, *J. Am. Chem. Soc.*, 2014, **136**, 16335-16344.

S3.5. J. Heyd, G. E. Scuseria and M. Ernzerhof, *J. Chem. Phys.*, 2003, **118**, 8207-8215.

S3.6. J. Heyd, G. E. Scuseria and M. Ernzerhof, *J. Chem. Phys.*, 2006, **124**.

S3.7. G. Kresse and J. Furthmuller, *Comput. Mater. Sci.*, 1996, **6**, 15.

S3.8. G. Kresse and D. Joubert, *Phys. Rev. B*, 1999, **59**, 1758.

S3.9. S. P. Ong, Y. Mo and G. Ceder, *Phys. Rev. B: Condens. Matter Mater. Phys.*, 2012, **85**.

S3.10. B. D. McCloskey, A. Valery, A. C. Luntz, S. R. Gowda, G. M. Wallraff, J. M. Garcia, T. Mori and L. E. Krupp, *J. Phys. Chem. Lett.*, 2013, **4**, 2989-2993.

Chapter 4

Fe$_2$O$_3$ Nanoparticle Seed Catalysts Enhance Cyclability on Deep (Dis)charge in Aprotic Li-O$_2$ Batteries

This chapter is based on:
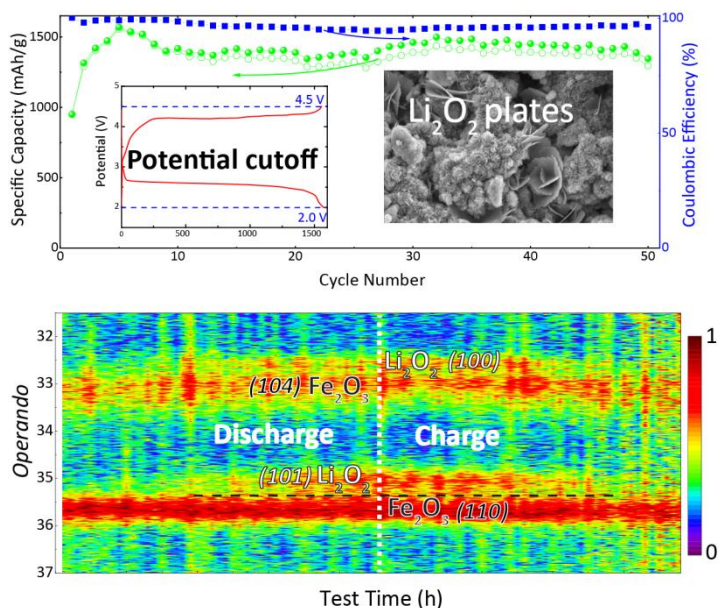
The Fe$_2$O$_3$/CNT cathode in Li–O$_2$ batteries is demonstrated to offer high cyclability and coulombic efficiency in potential limited (dis)charge. This is achived *via epitaxially* induced nucleation and growth of smaller and isoptropic Li$_2$O$_2$ crytallites on Fe$_2$O$_3$ seed catalyst owing to their similar lattic *d*-spacing. *Oprando* XRD confirms the reversible formation and decomposition of Li$_2$O$_2$ on the seed catalyst.

Abstract

Although the high energy density of Li–O$_2$ chemistry is promising for vehicle electrification, the poor stability and parasitic reactions associated with carbon-based cathodes and the insulating nature of discharge products limit their rechargeability and energy density. Here, we present a cathode material consisting of α–Fe$_2$O$_3$ nano-seeds and carbon nanotubes (CNT) that achieves excellent cycling stability on deep (dis)charge with high capacity. The initial capacity of Fe$_2$O$_3$/CNT electrode reaches 805 mAhg^{-1} (0.70 mAh/cm^2) at 0.2 mA/cm^2, while maintaining a capacity of 1098 mAhg^{-1} (0.95 mAh/cm^2) after 50 cycles. Our *operando* structural, spectroscopic, and morphological analysis on the evolution of Li$_2$O$_2$, indicates preferential Li$_2$O$_2$ growth on the Fe$_2$O$_3$. The similar *d*-spacing of the *(100)* Li$_2$O$_2$ and *(104)* Fe$_2$O$_3$ planes suggest that the latter *epitaxially* induced Li$_2$O$_2$ nucleation. This results in larger Li$_2$O$_2$ primary crystallites and smaller secondary particles compared to that deposited on CNT, which enhances the reversibility of the Li$_2$O$_2$ formation and leads to more stable interfaces within electrodes. Our mechanistic insights into dual-functional materials that act both as stable host substrates and promote redox reactions in Li–O$_2$ batteries represent new opportunities for controlling the discharge product morphology, leading to high cycling stability and coulombic efficiency.

4.1 Introduction

Rechargeable aprotic Li-air or Li–O$_2$ batteries have great potential to enable energy-hungry applications, owing to their extremely high theoretical specific energy density.[1-4] In typical aprotic Li–O$_2$ batteries, the (dis)charge process proceeds *via* the formation (oxygen reduction reaction, ORR) and decomposition (oxygen evolution reaction, OER) of Li$_2$O$_2$ according to the reaction $2\text{Li} + \text{O}_2 \underset{\text{charge}}{\overset{\text{discharge}}{\rightleftharpoons}} \text{Li}_2\text{O}_2$.[1] Therefore, the performance of this battery is determined by the reversibility of Li$_2$O$_2$ redox and the electrolyte stability.[1] The morphology and mechanism of Li$_2$O$_2$ deposition depends on the relative stability of the intermediate LiO$_2$ product in the electrolyte and the time scale of the Li$_2$O$_2$ formation on the cathode surface. While LiO$_2$ stability is determined by the stabilization of the Li$^+$ both through the solvation strength of the electrolyte (quantified by the donor number (DN)) and the association strength of the counter anion,[5-7] the time scale determines to what extent the intermediate LiO$_2$ species are solvated.[8] In an intermediate DN electrolyte, such as tetraethylene glycol dimethyl ether (TEGDME), the nucleation and growth of toroidal Li$_2$O$_2$ particles was proposed to occur *via* the solution dismutase mechanism at low current rates, whereas at fast rates quasi-amorphous thin films were observed on electrode surface.[8] Porous carbon based materials have been extensively explored as O$_2$ gas diffusion electrodes because of their high surface area, low weight and low cost. Unfortunately, the discharge product Li$_2$O$_2$ reacts with carbon and the electrolyte at high potentials that characterize the OER process, and forms byproducts that clog the electrode pores, resulting in capacity fading and poor cycling stability.[9, 10] Significant efforts have been expended to mitigate these side reactions by employing several combinations of noble metals (Au, Ru/RuO$_2$, and Pt),[11-21] transition metal oxides(MnO$_2$, Co/CoO/Co$_3$O$_4$, NiO, TiO$_2$)[22-33] and metal related compounds[34-40] both as catalysts and conductive matrices to improve the energy efficiency and cycle life of the Li-O$_2$ batteries.

Most often the reported cycling performance of Li-O$_2$ systems is based on capacity-limited cycling, rather than the preferred potential-limited cycling where the full electrode capacity is utilized. Capacity limitation makes it difficult to quantify if improved cycling stability can be attributed to the specific role of electrode or to the continuous consumption of new active sites on the electrode surface is delivered. To date, the only electrode systems that have displayed improved reversible Li$_2$O$_2$ formation and decomposition during potential limited cycling in aprotic Li–O$_2$ batteries are porous gold,[14] metallic RuO$_2$,[42] the metallic porous Magnéli phase Ti$_4$O$_7$[43], and TiC[37]. However, Ru and Au are heavy elements that limit their gravimetric energy density, and their high cost makes them unlikely candidates for practical Li–O$_2$ batteries. TiC based cathodes also exhibit

good capacity retention but have a relatively low gravimetric capacity (about 350 mAh/g in DMSO electrolyte and 520 mAh/g in TEGDME electrolyte)[37], and the same hold true for Ti$_4$O$_7$ electrodes.[41] Alternatively, iron and iron oxide are both low-cost and abundant, and carbon-supported iron-based catalysts[44-47] have been studied as O$_2$ diffusion electrodes for Li–O$_2$ batteries. Although iron oxide electrodes have been shown to exhibit lower overpotential, a higher capacity and better cycling performance compared to carbon electrodes upon capacity-limited cycling, full (dis)charge (with potential limited cycling) has not been reported to date, which is in fact a key figure-of-merit for these batteries.

Hematite Fe$_2$O$_3$ is known as a O$_2$ reduction catalyst in aqueous media[48, 49] and as an O$_2$ adsorption material.[50] While it is ostensibly a wide band gap semiconductor, the presence structrual of defects lead to significant electronic conductivity[50]. Shimizu K. *et al.*[48] and Sun M. *et al.*[49] found that *via* its catalytic activity, Fe$_2$O$_3$ could alter the ORR reaction pathway from a 2e$^-$ to a 4e$^-$ process in aqueous media. Gurlo A. *et al.*[50] have reported that oxygen could preferentially adsorp on the α-Fe$_2$O$_3$ surface, and Zhang P. *et al.*[33] found that Co$_3$O$_4$ acted as crystal seed by preferential oxygen adsorption, facilitating the formation of Li$_2$O$_2$ film and particles. Motivated by these observations, our work reported here demonstrates that oxygen cathodes prepared by a combination of nano-sized Fe$_2$O$_3$ seed crystallites with carbon nanotubes (CNT) exhibit an impressive cycle stability and large capacity when cycled in a large potential cutoff window of 2.0-4.5 V. The initial specific capacity of the Fe$_2$O$_3$/CNT electrode reaches about 805 mAh/g (0.70 mAh/cm^2), and it maintains a reversible capacity of ~1098 mAh/g (0.95 mAh/cm^2) after 50 cycles at a current density of 0.2 mA/cm^2. We propose that the similar *(104)* Fe$_2$O$_3$ and *(100)* Li$_2$O$_2$ lattice plane *d-spacing* induces epitaxial growth of Li$_2$O$_2$ on the Fe$_2$O$_3$ surface. The epitaxial growth enhances the nucleation of Li$_2$O$_2$ which enhances its crystallinity, and suppresses amorphous Li$_2$O$_2$ formation which leads to passivation. This epitaxial growth of Li$_2$O$_2$ on Fe$_2$O$_3$ seeds results in oriented and smaller secondary Li$_2$O$_2$ particles, which are responsible for more facile decomposition upon oxidation. The preferential formation of Li$_2$O$_2$ on Fe$_2$O$_3$ and the facile decomposition is proposed to be responsible for the significantly improved reversible Li$_2$O$_2$ formation and decomposition leading to the observed high capacity retention on deep (dis)charge.

4.2 Results and discussions

4.2.1 Electrochemical performance
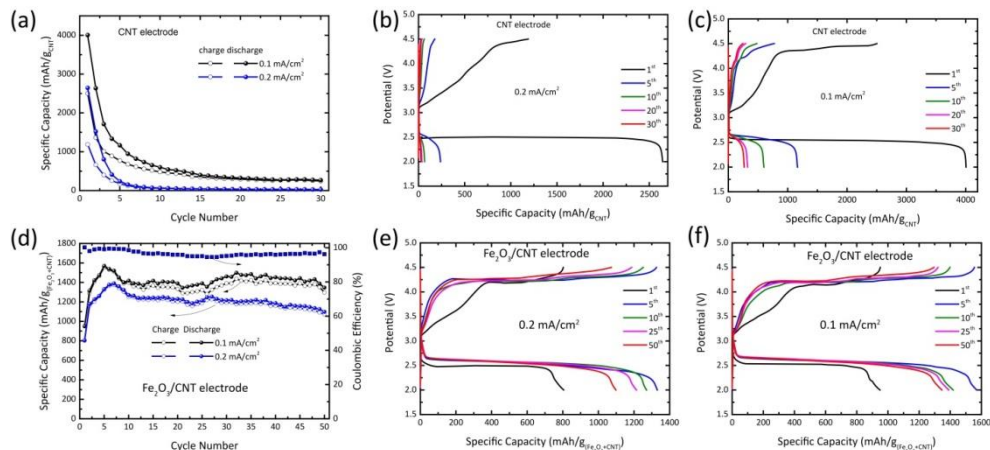
Figure 4.1. Cycling performance of (a) CNT and (d) Fe$_2$O$_3$/CNT oxygen cathodes during deep (dis)charge by employing a potential window of 2.0–4.5 V, measured in 0.5 M LiTFSI/TEGDME electrolyte at current densities of 0.1 and 0.2 mA/cm^2, respectively in Li–O$_2$ batteries at 1.0 bar O$_2$ pressure. (b), (c), (e), and (f) selected, potential cut-off, galvanostatic (dis)charge profiles for CNT and Fe$_2$O$_3$/CNT oxygen cathodes, respectively.

The use of Fe$_2$O$_3$ nano seed crystals in the gas diffusion cathode was also motivated by our previous study, where hexagonal NiO nanocrystals ($a=b$=2.972 ± 0.001 Å, c=7.158 ± 0.001 Å) were found to induce equiaxal growth of Li$_2$O$_2$ ($a=b$=3.142 ± 0.005 Å, c=7.650 ± 0.005 Å) due to an approximate match of their a- and b- lattice parameters.[30] The lattice parameters of the α–Fe$_2$O$_3$ ($a=b$=5.5035 Å and c=13.74 Å) are distinct from Li$_2$O$_2$, however, the inter planar spacing of its *(104)* (2.70 Å) and *(110)* (2.52 Å) planes are approximately equal to the *(100)* (2.72 Å) and *(101)* (2.56 Å) planes of Li$_2$O$_2$. (**Figure S4.1**). The CNTs plays an important role in forming an interpenetrating porous network structure that facilitates access of O$_2$, and they also provide electronic conductivity across electrodes and support the Fe$_2$O$_3$ catalyst.

Figure 4.1 displays the galvanostatic (dis)charge cycle performance of Li–O$_2$ batteries with CNT and Fe$_2$O$_3$/CNT cathodes by employing a potential cut–off at different (dis)charge current densities. The BET surface of the cast Fe$_2$O$_3$/CNT cathodes (75%/25% wt) is smaller (8.47 m^2/g), compared to that of the CNT powder (150-200 m^2/g). Therefore, the effective electrochemical surface area of Fe$_2$O$_3$/CNT electrodes must be significantly smaller compared to the CNT cathodes. That implies that when applying the same current density, based on the geometrical surface of the cathodes, the local current density should

be expected to be larger for the Fe_2O_3/CNT cathodes. The cycling stability of the CNT cathode is relatively poor (**Figure 4.1 (a), (b) and (c)**), and after 30 cycles the specific discharge capacity decreases drastically at current densities of 0.1 and 0.2 mAh/cm^2. Under the same cycling conditions, despite the fact that the local current density should be larger, the Fe_2O_3/CNT cathode shows significantly better cycling stability and coulombic efficiency, as shown in **Figure 4.1 (d), (e)** and **(f)**. The reversible specific capacity on deep (dis)charge of the Fe_2O_3/CNT electrode reaches 1295 mAh/g after 50 cycles at a current density of 0.1 mA/cm^2 (based on the total mass of the Fe_2O_3 and CNT), which is larger than the first discharge capacity (951 mAh/g). Also, at a current density of 0.2 mA/cm^2, the initial specific discharge capacity of the Fe_2O_3/CNT cathode is 805 mAh/g, and it maintains a capacity of 1098 mAh/g after 50 cycles. The incremental capacity increase over cycling is most likely the result of continuous activation of the Fe_2O_3 surface due to the gradual impregnation of the electrolyte into the porous structure of CNT and Fe_2O_3 nanoparticles, which activates more reaction surface over time.[41]

Interestingly, after the first cycle the specific capacity of the Fe_2O_3/CNT cathode (normalized using geometric surface of the electrode) is larger than that of the CNT cathode (**Figure S4.2**). Again we note that the electrochemical surface area of the Fe_2O_3 electrodes is expected to be smaller based on the smaller Fe_2O_3 surface area compared to that of CNT. The initial discharge capacity of the Fe_2O_3/CNT cathode is 0.6 and 0.7 mAh/cm^2, and 0.95 and 1.05 mAh/cm^2 for the CNT cathode at current densities of 0.1 and 0.2 mA/cm^2, respectively (Figure S2). However, after 30 deep (dis)charge cycles, the capacities for the CNT electrode dramatically drop to almost zero. In contrary, the capacity of the Fe_2O_3/CNT electrode increases to 0.85 and 0.95 mAh/cm^2 after 50 deep (dis)charge cycles at current densities of 0.1 and 0.2 mA/cm^2, respectively. The results indicate that the Fe_2O_3/CNT cathode surface is more active towards ORR compared to the CNT cathode, hence triggering the formation of more Li_2O_2. The charge overpotential of the Fe_2O_3/CNT electrode is 200 mV lower than that of the CNT cathode (**Figure S4.3**), which was also observed in other studies.[44, 45]

As an anode in lithium-ion batteries, Fe_2O_3 nanostructured materials follow a series of Li-insertion processes resulting in two voltage plateaus at approximately 1.2 V and 0.75 V, respectively.[51, 52] A Fe_2O_3/CNT electrode cycled in Ar within a 2.0–4.5 V window (**Figure S4.4**), shows a reversible capacity of only 24 mAh/g (0.027 mAh/cm^2) at a current density of 0.1 mA/cm^2. On the other hand, in the presence of O_2, the Fe_2O_3/CNT cathode displays a stable discharge plateau at around 2.6 V, as shown in **Figure 4.1(e)** and **(f)**. Thus within the potential window of 2.0–4.5 V, the Li-intercalation reaction does not contribute to the discharge capacity of the Fe_2O_3/CNT cathode in a $Li–O_2$ battery.

Figure S4.5 shows the cyclic voltammetry (CV) curves of CNT and Fe$_2$O$_3$/CNT cathodes, respectively. The observed bell shaped oxygen reduction curves of both the CNT and Fe$_2$O$_3$/CNT cathodes can be described on the basis of the diffusion controlled currents originating from the expected formation process of Li$_2$O$_2$.[53] Due to the low electronic conductivity of lithium oxide, the oxidation overpotential is observed to be high. The oxygen evolution anodic peaks can be attributed to the oxidation process of Li$_2$O$_2$.[53, 54]

4.2.2 Analysis of the evolution of products during (dis)charge
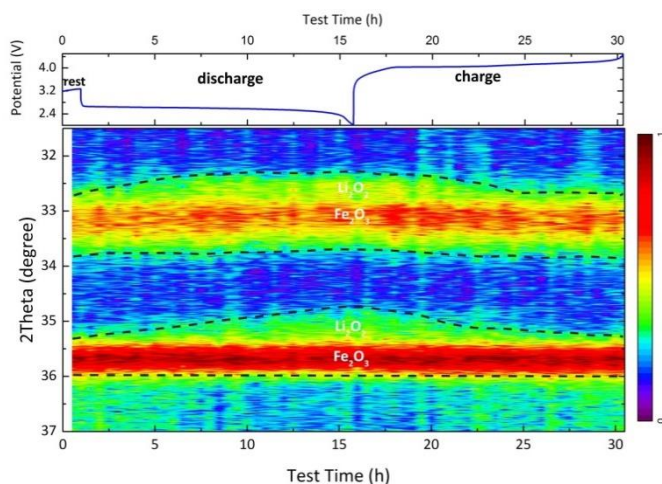
Figure 4.2. Top: (Dis)charge profile of the Fe$_2$O$_3$/CNT oxygen cathode in an *operando* Li–O$_2$ battery. Bottom: Two-dimensional contour plots of the *operando* XRD patterns showing the 2ϑ region between 31.5-37° during a complete (dis)charge cycle, demonstrating the formation of Li$_2$O$_2$ and its decomposition. The battery was (dis)charged using a 0.5 M LiTFSI/TEGDME electrolyte within a potential window of 2.0–4.5 V at a current density of 0.2 mA/cm^2.

In principle, the potential of a Li–O$_2$ battery system should sharply increase when the discharge product is completely decomposed during charge. This is typically observed in Li-ion battery electrodes, where after all of the removable lithium ions are extracted, the potential steeply increases towards the cutoff voltage. However, this phenomenon is seldom reported for Li–O$_2$ batteries, where capacity restriction is typically used to demonstrate the electrochemical performance of oxygen cathodes. Thereby, side reactions with the electrolyte that occur at large and small potentials are avoided, at the same time the reversibility is artificially improved as the battery is only partially discharged. Potential limited cycling utilizes the full capacity, and is more challenging, because side reactions are unavoidable in an aprotic Li–O$_2$ battery at high charge

potentials. These parasitic reactions lead to the formation of Li_2CO_3, the decomposition of the electrolyte and the decomposition of the binder in the cathode.[55]

To investigate the reversibility of the products on the Fe_2O_3/CNT oxygen cathodes at high charge potentials, the discharge capacity was restricted to 0.5 and 0.25 mAh and the Li–O_2 batteries were subsequently charged to 4.5 V at current densities of 0.1 and 0.2 mA/cm^2, respectively, as shown in **Figure S4.6**. Under these conditions the Li–O_2 battery also exhibits stable cycling, where the potential limited charge capacity is very close to the discharge capacity over 50 cycles (**Figure S4.6(a) and (d)**). The discharge plateau is close to 2.6 V (**Figure S4.6(b), (d), (e)** and **(f)**). Notably, the charge voltage increases to 4.5 V at the end of the charge process following the stable charge plateaus, which is rarely reported for Li–O_2 battery (dis)charge profiles. From the *ex-situ* XRD patterns shown in the supporting information **Figure S4.7(a)**, it is difficult to observe differences between the diffraction peaks of the pristine and discharged Fe_2O_3/CNT cathode at the current densities of 0.1 and 0.2 mA/cm^2, as expected owing to the similar lattice spacing of *(104)* Fe_2O_3 and *(100)* Li_2O_2 planes (**Figure S4.1**). The SEM images also show no significant difference between the pristine sample (**Figure S4.7(b)**) and the discharged cathode (**Figure S4.7(c)**), with the exception of a film-like structure that forms at a current density of 0.2 mA/cm^2. This most likely represents the deposition of a quasi-amorphous thin Li_2O_2 film, which is known to occur at high (dis)charge currents.[8] Using the titration experiment developed by McCloskey and co-workers[56] (**Figure S4.8**), the yield of Li_2O_2 after 1st discharge to 2.0 V on the surface of Fe_2O_3/CNT cathodes was found to be 95.7% and 96.5% compared to the theoretical capacity at the current density of 0.2 mA/cm^2 and 0.1 mA/cm^2, respectively, confirming that the discharge capacity of the Fe_2O_3/CNT cathode is mainly due to the formation of Li_2O_2. On-line electrochemical mass spectrometry (OEMS) measurements were performed to quantify the O_2 evolution during charge (**Figure S4.9**). Even though O_2 evolution does not match electrons involved in the first charge in the OEMS experiment, only O_2 is detected over the charge plateau (**Figure S4.9(a)**). At the end of charge, CO_2 is generated from the decomposition of some carbonates that are unavoidably generated *via* reaction of superoxide and/or peroxide with the electrolyte. This is the reason for the lower e$^-$/O_2 ratio in **Figure S4.9(b)** (compared to the theoretical value of 2e$^-$/O_2 corresponding to pure O_2 evolution); namely some byproducts form that are not related to the evolution of O_2. Unfortunately, despite the increased columbic efficiency, the stability of all the cell components (electrolyte, CNT conductive support, *etc.*) in the electrolyte with an intermediate donor number still need to be addressed in order to obtain an ratio of 2.0 e$^-$/O_2. However the aim of this study is to show the beneficial impact of the Fe_2O_3 on the reversible growth of Li_2O_2, resulting in the improved cycling under potential limited cycling.

To verify the formation and decomposition of Li_2O_2 on the Fe_2O_3/CNT cathode, *operando* XRD was carried out on a Li-O_2 battery cycled within a potential window of 2.0–4.5 V at a current density of 0.2 mA/cm^2 in a 0.5 M LiTFSI/TEGDME electrolyte (**Figure 4.2**). Since the *(104)* and *(110)* lattice plane distances of Fe_2O_3 are very similar to the *(100)* and *(101)* planes of Li_2O_2，respectively (**Figure S4.1**), the reflections are not distinguishable in *ex-situ* XRD measurements of discharged cathodes, especially due to the broadened of nano-sized Fe_2O_3 peaks. However, the two-dimensional contour *operando* XRD patterns in the *2ϑ* region of 31.5–37° (**Figure 4.2**) shows a symmetric broadening of the *(100)/(104)* and the *(101)/(110)* Li_2O_2/Fe_2O_3 lattice planes, confirming the gradual formation and decomposition of Li_2O_2.
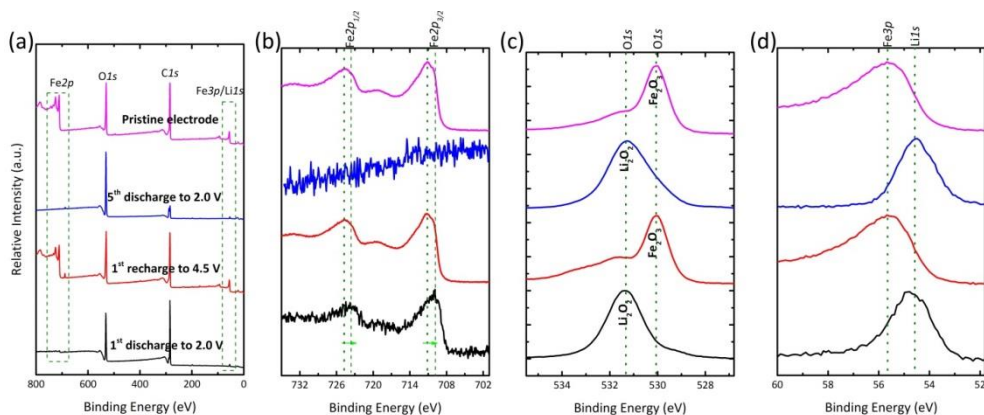
Figure 4.3. (a) XPS survey scans of Fe_2O_3/CNT oxygen cathodes at different (dis)charge states. (b), (c) and (d) High resolution XPS in the Fe2p, O1s and Li1s or Fe3p regions, respectively of the Fe_2O_3/CNT oxygen cathode at different states of (dis)charge. The black, red, blue, and pink lines represent the cathode at the state of 1st discharge to 2.0 V, 1st recharge to 4.5 V, 5th discharge to 2.0 V, and pristine states, respectively.

To further investigate the discharge product formed on the cathode surface at a current density of 0.2 mA/cm^2, *ex-situ* X-ray photoelectron spectroscopy (XPS) analysis (**Figure 4.3**) was carried out on the pristine Fe_2O_3/CNT cathode and cathodes from discharged and recharged batteries (discharge to 2.0 V and recharge to 4.5 V; the electrochemical performance of these batteries are shown in **Figure S4.10**). All spectra were calibrated using the C1s peak of CNT at 284.48 eV. The survey scan from 0 to 800 eV is given in **Figure 4.3(a)** and shows the relative change in the quantities of oxygen, lithium, and iron on the surface of the Fe_2O_3/CNT cathodes. The relative intensity of the Fe2p peaks for the Fe_2O_3/CNT cathodes diminishes after the 1st and 5th discharge (black and blue lines in **Figure 4.3(a)**), but recovers after recharge (red line in **Figure 4.3(a)**), indicating that the surface of the cathode is covered with a discharge product which is

removed after charge. **Figure 4.3(b–d)** displays the XPS spectra in the Fe2p, O1s and Li1s/Fe3p regions, respectively. The Fe2p region from 705 to 730 eV shows the characteristic 2p$_{1/2}$ and 2p$_{3/2}$ doublet which is attributed to Fe$_2$O$_3$ (pink line in **Figure 4.3(b)**).[57] After the 1st discharge, the peak becomes less prominent (black line in **Figure 4.3(b)**), and after the 5th discharge the peak becomes indistinguishable (blue line in **Figure 4.3(b)**). However, when the cathode is recharged to 4.5 V, the Fe2p signal completely reappears, and is similar to the pristine sample (red and pink lines in **Figure 4.3(b)**). This is an indication of the formation and decomposition of products on the cathode surface during (dis)charge. In addition, after 1st discharge, the main peak of Fe2p slightly shifts to low binding energy compared to the pristine and recharged cathodes, which may be attributed to the surface redox activities (involving Fe$^{2+/3+}$ redox couple). Further, this could probably overlap with the surface bonds between Li$_2$O$_2$ and Fe$_2$O$_3$. In the pristine electrode, O1s spectral peaks (pink line in **Figure 4.3(c)**) appear from 528 to 533 eV and can be assigned to Fe-O and Fe-OH from Fe$_2$O$_3$.[57] The features (pink line in **Figure 4.3(d)**) in the region from 55.5 to 57.3 eV can be attributed to the Fe3p contribution from Fe$_2$O$_3$. It is interesting to note that after the 1st and 5th discharge to 2.0 V, the spectral peaks in the O1s and Fe3p/Li1s regions (black and blue lines in **Figure 4.3(c) and (d)**) shift to binding energies of 54.6 eV and 531.2 eV, mainly corresponding to the lithium and oxygen contributions from Li$_2$O$_2$, respectively.[58] Furthermore, after recharge (red line in **Figure 4.3(c) and (d)**), the shift of peaks in this region return to their original positions, indicating reappearance of the Fe2p and Fe3p contributions and hence the removal of Li$_2$O$_2$ from the cathode surface. In summary, from the XPS analysis of the pristine, discharged and recharged samples, we conclude that Li$_2$O$_2$ is the main product formed reversibly on the Fe$_2$O$_3$/CNT cathode surface during (dis)charge in the Li–O$_2$ battery.
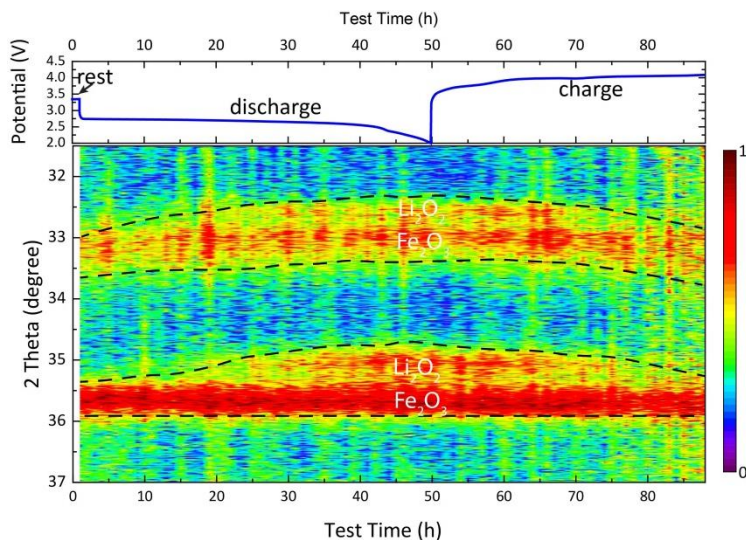
Figure 4.4. Top: (Dis)charge profile of the electrochemical performance of the Fe$_2$O$_3$/CNT oxygen cathode in an *operando* Li–O$_2$ battery. Bottom: Two-dimensional contour plots of the *operando* XRD patterns showing the *2ϑ* region between 31.5-37˚, during a complete (dis)charge cycle demonstrating the formation and decomposition of Li$_2$O$_2$. The *operando* Li–O$_2$ battery was (dis)charged using a 0.5 M LiTFSI/TEGDME electrolyte within a potential window of 2.0–4.5 V at a current density of 0.05 mA/cm^2.

　　　Figure 4.4 shows the two dimensional contour plot of the *operando* XRD patterns of the Fe$_2$O$_3$/CNT cathode at a lower current density of 0.05 mA/cm^2 compared to that shown in **Figure 2**. Discernable Li$_2$O$_2$ XRD peaks are observed on the Fe$_2$O$_3$/CNT cathode when the discharge current density is lowered to 0.05 mA/cm^2 (**Figure 4.5(a)**). The gradual increase and decrease in the intensities of the Li$_2$O$_2$ reflections, corresponding to the *(100)* and *(101)* planes of Li$_2$O$_2$ (**Figure 4.4)**, indicate the gradual formation and decomposition of Li$_2$O$_2$ on the Fe$_2$O$_3$/CNT cathode as a function of (dis)charge time. The *ex-situ* SEM image of the Fe$_2$O$_3$/CNT cathode after discharge to 2.0 V shows a homogenous platelet morphology of the Li$_2$O$_2$ particles (**Figure 4.5(b)**). Based on the Rietveld refinement of the sequential *operando* XRD patterns (**Figure 4.5(c)**), we obtained the average coherent size of Li$_2$O$_2$ as a function of (dis)charge time (**Figure 4.5(d)**). During the refinement, the Fe$_2$O$_3$ parameters were fixed based on the refinement result as shown in the supporting information **Figure S4.11**. The average coherent length of the Li$_2$O$_2$ crystallite platelets first increases during initial discharge, after which it decreases as discharge progresses. This indicates the formation of larger, and more anisotropic shaped Li$_2$O$_2$ crystallites at the initial stages of discharge. The deposition of smaller and more isotropic Li$_2$O$_2$ occurs as discharge progresses, similar to what we reported previously.[59] During charge, smaller Li$_2$O$_2$ crystallites preferentially decompose followed by the decomposition of the larger

Li$_2$O$_2$ crystallites, as can be concluded from the initial increase in the average coherence length of Li$_2$O$_2$ (after which it remains constant to the end of charge).[60]
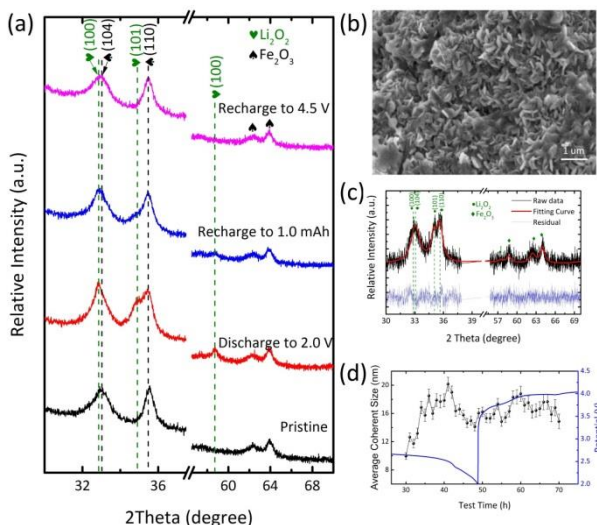
Figure 4.5. (a) *Ex-situ* XRD patterns of the Fe$_2$O$_3$/CNT cathode at different discharge and recharge states. (b) SEM image of the Li$_2$O$_2$ particles formed on the Fe$_2$O$_3$/CNT cathode at the end of discharge. (c) Rietveld refinement result of the XRD patterns. (d) Average coherent size of Li$_2$O$_2$ obtained from Rietveld refinement as a function of (dis)charge time. The corresponding voltage profile measured during (dis)charge is illustrated in the graph.

Figure 4.6 displays XRD patterns and SEM images of the discharge product formed on the cathode surface at even lower current densities (0.02 mA/cm^2). Very evident Li$_2$O$_2$ peaks are observed in the XRD patterns of both the discharged CNT and Fe$_2$O$_3$/CNT cathodes, as observed in **Figure 4.6(a)**. After complete discharge at a current density of 0.02 mA/cm^2, the surface of the CNT cathode (**Figures 4.6(b)** and **(c))** shows homogenous toroidal Li$_2$O$_2$ particles - about 500 nm in diameter and 100 nm in thickness, randomly oriented on the cathodes. In contrast, the surface of the Fe$_2$O$_3$/CNT cathode (**Figures 4.6(d)** and **(e))** at the end of the discharge is covered by Li$_2$O$_2$ with significantly smaller disc-like particles - about 300 nm in diameter and several tens of nanometer in thickness, and some large flower-like plates, several micrometers in diameter and a hundred nanometers in thickness. Notably, the Li$_2$O$_2$ disc-like particles on the Fe$_2$O$_3$/CNT cathode appear to be oriented perpendicular to the Fe$_2$O$_3$ surface and are more frequently vertically aligned. The difference in Li$_2$O$_2$ morphology between the CNT and Fe$_2$O$_3$/CNT cathodes, suggests a different growth mechanism induced by the Fe$_2$O$_3$ seeds. In the presence of Fe$_2$O$_3$ nanoparticles, at low discharge current density, disk like rather than toroidal Li$_2$O$_2$ particles are formed, some of which grow into flower-like structures.

The cycling performance of the Fe$_2$O$_3$/CNT cathode battery at a current density of 0.02 mA/cm^2 upon deep (dis)charge is represented in **Figure S4.12**. The rather good cycling stability and high coulombic efficiency (exceeding 90%) over the first 20 cycles again suggests that the Li$_2$O$_2$ morphology on the Fe$_2$O$_3$/CNT cathode allows for more stable cycling compared to that on the CNT cathodes under comparable conditions.
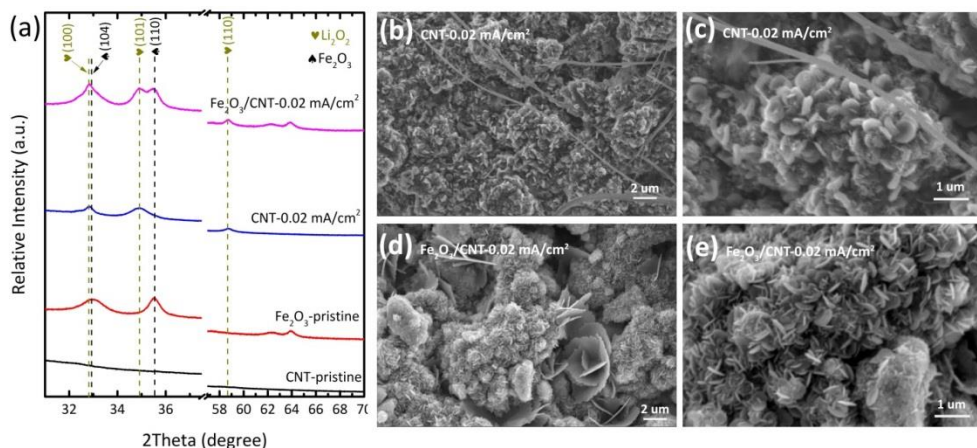
Figure 4.6. (a) The Li$_2$O$_2$ and Fe$_2$O$_3$ XRD reflections resulting from CNT and Fe$_2$O$_3$/CNT oxygen cathodes at the end of complete discharge, respectively. (b, c) and (d, e) SEM images of the CNT cathode and the FeO$_3$/CNT cathode at the end of discharge with a current density of 0.02 mA/cm^2.

4.3 Mechanism

Since TEGDME has an intermediate DN, Li$_2$O$_2$ formation is expected to take place both through formation in the solvent and directly on the surface of the cathode.[5, 6] The different Li$_2$O$_2$ morphology obtained upon adding Fe$_2$O$_3$ to the CNT cathodes, observed in the SEM images in **Figure 4.6(b–e)**, demonstrates that the presence of Fe$_2$O$_3$ influences the growth mechanism of the Li$_2$O$_2$ particles. In this context we remind that Fe$_2$O$_3$ is a wide band gap hopping semiconductor, but the presence of extensive defects leads to significant electronic conductivity. Previously, hexagonal NiO nanoparticles were used as nano-seed crystals to induce equiaxal growth of Li$_2$O$_2$ owing to their similar *a*- and *b*-lattice parameters.[30] The Fe$_2$O$_3$ nano-seed particles have even more similar inter-planar spacing to that of Li$_2$O$_2$, as shown in **Figure 4.7** and **Figure S4.1**. In the XRD pattern of the Fe$_2$O$_3$ nanoparticles the *(104)* reflection is broader than the *(110)* reflection (**Figure S4.11**), reflecting the anisotropic shape of the Fe$_2$O$_3$ nanoparticles.[58] High resolution TEM image (**Figure S4.14**) indicates that the Fe$_2$O$_3$ nanoparticles have a two dimensional shape, where the long-dimension is along the [*hk0*] direction and the short-dimension is along the [*00l*]

direction. TEM image also shows that the inter-planar spacing on the surface of the Fe_2O_3 crystallites is close to 0.27 nm. The similar value of the *d*-spacing of the Li_2O_2 *(100)* lattice planes (0.272 nm in **Figure S4.1**) led us to hypothesize a "*epitaxially* induced nucleation and growth" mechanism for Li_2O_2 growth on Fe_2O_3. This mechanism is schematically shown in **Figure 4.7** where (1) the Li_2O_2 crystallite nucleates on the *[0k0]* surface facets of the Fe_2O_3 crystallite; (2) because the dominant Li_2O_2 growth direction is *(001)*[60, 61], and the footprint of the Li_2O_2 crystallite is in the *(100)/(010)* direction, which matches on the *(104)* lattice plane exposed on the Fe_2O_3 surface. This is consistent with the disc-like Li_2O_2 particles that appear to grow perpendicular to the Fe_2O_3/CNT electrode surface observed in **Figure 4.6(d-e)**. The Rietveld refinement shows no significant change in lattice parameters of the Li_2O_2 that forms on the CNT and F_2O_3/CNT cathodes (**Figure S4.13** and **Table S4.1**) in contrast to NiO[30].

It is established that the current density affects the morphology of the Li_2O_2 formed.[8] This is also confirmed by the present XRD studies where the average coherent length of Li_2O_2 at relatively low current density (0.02 mA/cm^2) (**Table S4.1**) is larger than that at high current density (0.05 mA/cm^2) (**Figure 4.5(d)**) on the Fe_2O_3/CNT electrode. Interestingly, comparing the XRD refinement results (**Table S4.1**) of the average coherent length of Li_2O_2 crystallites, the larger and much more isotropic Li_2O_2 crystallites are formed on the Fe_2O_3/CNT cathodes compared to that on CNT cathode. However, comparing the SEM images in **Figure 4.5(b)**, **Figure 4.6(b-e)** suggests that significantly smaller disc-like Li_2O_2 secondary particles form on Fe_2O_3/CNT cathodes. The smaller secondary particles will be easier to decompose upon charge due to their relatively higher surface area. Another aspect of the proposed *epitaxial* growth mechanism is that the larger crystallites indicate that the Fe_2O_3 enhances the crystallinity of the Li_2O_2, thus suppressing the formation of passivating amorphous films, as also observed on NiO seed crystallites[30], and enhances reversiblity of Li_2O_2. This is particularly noteworthy as the local current density is most likely much larger on the Fe_2O_3/CNT cathodes because of their smaller surface area. Another advantage is that at high charge potentials the Li_2O_2–Fe_2O_3 interface can be expected to more stable than Li_2O_2–carbon interface, which forms a thin isolating Li_2CO_3 film.[10] In this context, it is important to note that hematite Fe_2O_3 nano structures exhibit good electronic conductivity[50, 62, 63], necessary for the electron transport between the carbon matrix and the Li_2O_2. Finally, preferential adsorption of oxygen onto the surface of α-Fe_2O_3 surface[64], may promote the deposition of Li_2O_2 on the Fe_2O_3 surface.

These favorable properties of α-Fe_2O_3 most likely contributing to the reversible growth of Li_2O_2 provide a rational for the improved reversibility upon potential-limited cycling of the Fe_2O_3/CNT cathodes in direct comparison to the CNT cathodes. As discussed,

the Fe$_2$O$_3$ impacts the reversible formation of Li$_2$O$_2$, which appears to be the origin of the improved reversibility; however, this is not expected to prevent detrimental reactions between the intermediate discharge products and the electrolyte. The relatively large coulombic efficiency (*ca*. >95% for Li$_2$O$_2$ production), especially under potential limited cycling conditions, in combination with the titration results suggests a reduction in the degree of side reactions. Possibly, faster Li$_2$O$_2$ nucleation induced by Fe$_2$O$_3$ may reduce the exposure time of intermediate discharge products. However, the far from theoretical O$_2$ evolution measured by OEMS indicates that parasitic reactions as generally observed for this system or reversible reactions that do not involve O$_2$ evolution cannot be excluded, which will be topic of further investigations.
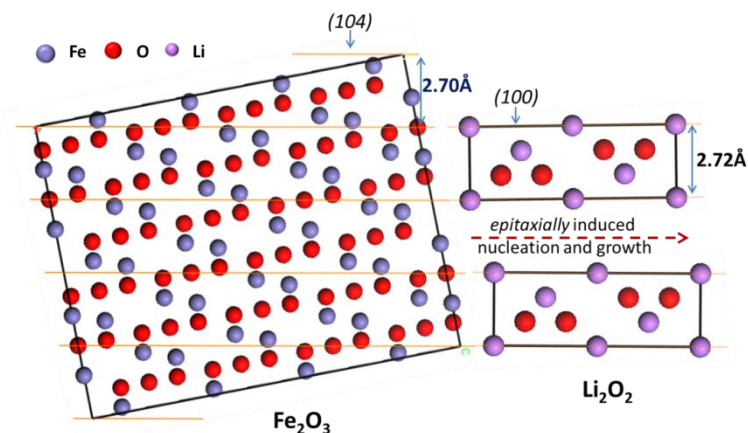
Figure 4.7. Schematic of the proposed "*epitaxially* induced nucleation and growth" mechanism of Li$_2$O$_2$ on Fe$_2$O$_3$. The Fe$_2$O$_3$ crystallites expose the *(104)* lattice *spacing* at their surface, which matches the *(100)* lattice distance of the Li$_2$O$_2$ crystallites, which grow in the *(001)* direction perpendicular to the Fe$_2$O$_3$ surface.

4.4 Conclusions

In conclusion, we have demonstrated that a Li−O$_2$ battery consisting of an Fe$_2$O$_3$/CNT oxygen cathode with TEGDME electrolyte offers more reversible cycling on deep potential-restricted (dis)charge with a capacity retention of ~1098 mAh/g (0.95 mAh/cm^2) after 50 cycles at a current density of 0.2 mA/cm^2. *Operando* XRD and *ex-situ* XPS measurements reveal the reversible formation and decomposition of Li$_2$O$_2$ crystallites during (dis)charge at high and intermediate current densities (0.2 and 0.05 mA/cm^2). At low current densities (0.02 mA/cm^2) small disc–like particles and some large plates of Li$_2$O$_2$ form perpendicular to the Fe$_2$O$_3$/CNT electrode surface, which are very different from that of toroidal Li$_2$O$_2$ particles formed on the CNT electrode. Based on the similar lattice spacing of the

(104)/(100) reflections in Fe$_2$O$_3$/Li$_2$O$_2$, we have hypothesized a "*epitaxially* induced nucleation and growth" mechanism. The resulting Li$_2$O$_2$ has a more isotropic crystallite shape and a smaller secondary particle size, where the *epitaxial* growth and the larger surface area appears to be responsible for the improved reversibility of the Li$_2$O$_2$ formation and oxidation. Although electrolyte stability remains a critical issue, the "*epitaxially* induced nucleation and growth" mechanism proposed in this work can be potentially used to gain control over the Li$_2$O$_2$ growth and thereby improve the electrochemical performance of Li–O$_2$ batteries.

References

1. Aurbach, D.; McCloskey, B. D.; Nazar, L. F.; Bruce, P. G. *Nat. Energy* **2016,** *1*, 16128.
2. Luntz, A. C.; McCloskey, B. D. *Chem. Rev.* **2014,** *114*, 11721.
3. Lu, J.; Li, L.; Park, J. -B.; Sun, Y. -K.; Wu, F.; Amine, K. *Chem. Rev.* **2014,** *114,* 5611.
4. Black, R.; Adams, B.; Nazar, L. F. *Adv. Energy Mater.* **2012,** *2,* 801.
5. Johnson, L.; Li, C.; Liu, Z.; Chen, Y.; Freunberger, S. A.; Ashok, P. C.; Praveen, B. B.; Dholakia, K.; Tarascon, J. M.; Bruce, P. G. *Nat. Chem.* **2014,** *6,* 1091.
6. Aetukuri, N. B.; McCloskey, B. D.; García, J. M.; Krupp, L. E.; Viswanathan, V.; Luntz, A. C. *Nat. Chem.* **2015,** *7,* 50.
7. Burke, C. M.; Pande, V.; Khetan, A.; Viswanathan, V.; McCloskey, B. D. *Proc. Natl. Acad. Sci.* **2015,** *112,* 9293.
8. Adams, B. D.; Radtke, C.; Black, R.; Trudeau, M. L.; Zaghib, K.; Nazar, L. F. *Energy Environ. Sci.* **2013,** *6,* 1772.
9. McCloskey, B. D.; Scheffler, R.; Speidel, A.; Girishkumar, G.; Luntz, A. C. *J. Phys. Chem. C* **2012,** *116,* 23897.
10. McCloskey, B. D.; Speidel, A.; Scheffler, R.; Miller, D. C.; Viswanathan, V.; Hummelshøj, J. S.; Nørskov, J. K.; Luntz, A. C. *J. Phys. Chem. Lett.* **2012,** *3,* 997.
11. Lu, Y.-C.; Xu, Z.; Gasteiger, H. A.; Chen, S.; Hamad-Schifferli K.; Shao-Horn, Y. *J. Am. Chem. Soc.* **2010,** *132*, 12170.
12. Lu, Y. -C.; H. Gasteiger, A.; Shao-Horn, Y. *J. Am. Chem. Soc.* **2011,** *133,* 19048.
13. McCloskey, B. D.; Scheffler, R.; Speidel, A.; Bethune, D. S.; Shelby, R. M.; Luntz, A. C. *J. Am. Chem. Soc.* **2011,** *133,* 18038.
14. Peng, Z.; S. Freunberger, A.; Chen, Y.; Bruce, P. G. *Science* **2012,** *337,* 563.
15. Lim, H. D.; Song, H.; Gwon, H.; Park, K. -Y.; Kim, J.; Bae, Y.; Kim, H.; Jung, S. -K.; Kim, T.; Kim, Y. H.; Lepro, X.; Ovalle-Robles, R.; Baughman, R. H.; Kang, K. *Energy Environ. Sci.* **2013,** *6,* 3570.
16. Yilmaz, E.; Yogi, C.; Yamanaka, K.; Ohta, T.; Byon, H. R. *Nano Lett.* **2013,** *13,* 4679.

17. Jian, Z.; Liu, P.; Li, F.; He, P.; Guo, X.; Chen, M.; Zhou, H. *Angew. Chem., Int. Ed.* **2014,** *53,* 442.

18. Li, F.; Chen, Y.; Tang, D. -M.; Jian, Z.; Liu, C.; Golberg, D.; Yamada, A.; Zhou, H. *Energy Environ. Sci.* **2014,** *7,* 1648.

19. Ma, S.; Wu, Y.; Wang, J.; Zhang, Y.; Zhang, Y.; Yan, X.; Wei, Y.; Liu, P.; Wang, J.; Jiang, K.; Fan, S.; Xu, Y.; Peng, Z. *Nano Lett.* **2015,** *15,* 8084.

20. Su, D. W. S.; Dou, X.; Wang, G. X. *Mater. Chem. A* **2015,** *3,* 18384.

21. Tong, S.; Zheng, M.; Lu, Y.; Lin, Z.; Zhang, X.; He, P.; Zhou, H. *Chem. Commun.* **2015,** *51,* 7302.

22. Jiao, F.; Bruce, P. G. *Adv. Mater.* **2007,** *19,* 657.

23. Débart, A.; Paterson, A. J.; Bao, J.; Bruce, P. G. *Angew. Chem.* **2008,** *120*, 4597.

24. Wu, J.; Park, H. W.; Yu, A.; Higgins, D.; Chen, Z. *J. Phys. Chem. C* **2012,** *116,* 9427.

25. Black, R.; Lee, J.-H.; Adams, B.; Mims, C. A.; Nazar, L. F. *Angew. Chem., Int. Ed.* **2013,** *52,* 392.

26. Ryu, W. -H.; Yoon, T. -H.; Song, S. H.; Jeon, S.; Park, Y. -J.; Kim, I. -D. *Nano Lett.* **2013,** *13,* 4190.

27. Zhao, G.; Mo, R.; Wang, B.; Zhang, L.; Sun, K. *Chem. Mater.* **2014,** *26,* 2551.

28. Gao, R.; Zhu, J.; Xiao, X.; Hu, Z.; Liu, J.; Liu, X. *J. Phys. Chem. C* **2015,** *119,* 4516.

29. Schroeder, M. A.; Pearse, A. J.; Kozen, A. C.; Chen, X.; Gregorczyk, K.; Han, X.; Cao, A.; Hu, L.; Lee, S. B.; Rubloff, G. W.; Noked, M. *Chem. Mater.* **2015,** *27,* 5305.

30. Ganapathy, S.; Li, Z.; Anastasaki, M. S.; Basak, S.; Miao, X. -F.; Goubitz, K.; Zandbergen, H. W.; F. Mulder, M.; Wagemaker, M. *J. Phys. Chem. C* **2016,** *120,* 18421.

31. Yoon, K. R.; Lee, G. Y.; Jung, G. J. -W.; Kim, N. -H.; Kim, S. O.; Kim, I. -D. *Nano Lett.* **2016,** *16,* 2076.

32. Zhang, P.; Wang, R.; He, M.; Lang, J.; Xu, S.; Yan, X. *Adv. Funct. Mater.* **2016,** 26, 1354.

33. Zhang, P.; Zhang, S.; He, M.; Lang, J.; Ren, A.; Xu, S.; Yan, X. *Adv. Sci.* **2017,** 4, 1700172.

34. Oh, S. H.; Nazar, L. F. *Adv. Energy Mater.* **2012,** *2,* 903.

35. Wang, H.; Yang, Y.; Liang, Y.; Zheng, G.; Li, Y.; Cui, Y.; Dai, H. *Energy Environ. Sci.* **2012,** *5,* 7931.

36. Li, F.; Ohnishi, R.; Yamada, Y.; Kubota, J.; Domen, K.; Yamada, A.; Zhou, H. *Chem. Commun.* **2013,** *49,* 1175.

37. Ottakam Thotiyl, M. M.; Freunberger, S. A.; Peng, Z.; Chen, Y.; Liu, Z.; Bruce, P. G. *Nat. Mater.* **2013,** *12,* 1050.

38. Xie, J.; Yao, X.; Madden, I. P.; Jiang, D. -E.; Chou, L. -Y.; Tsung, C. -K.; Wang, D. *J. Am. Chem. Soc.* **2014,** *136,* 8903.

39. Kundu, D.; R. Black; Adams, B.; Harrison, K.; Zavadil, K.; Nazar, L. F. *J. Phys. Chem. Lett.* **2015,** *6,* 2252.

40. Sennu, P.; Christy, M.; Aravindan, V.; Lee, Y. -G.; Nahm, K.S.; Lee, Y. -S. *Chem. Mater.* **2015,** *27,* 5726.

41. Li, F.; Tang, D. -M.; Zhang, T.; Liao, K.; He, P.; Golberg, D.; Yamada, A.; Zhou, H. *Adv. Energy Mater.* **2015,** *5,* 1500294.

42. Liao, K.; Wang, X.; Sun, Y.; Tang, D.; Han, M.; He, P.; Jiang, X.; Zhang, T.; Zhou, H. *Energy Environ. Sci.* **2015,** *8,* 1992.

43. Kundu, D.; Black, R.; Berg, E. J.; Nazar, L. F. *Energy Environ. Sci.* **2015,** *8,* 1292.

44. Zhang, W.; Zeng, Y.; Xu, C.; Tan, H.; Liu, W.; Zhu, J.; Xiao, N.; Hng, H. H.; Ma, J.; Hoster, H. E.; Yazami, R.; Yan, Q. *RSC Adv.* **2012,** *2,* 8508.

45. Zhang, Z.; Zhou, G.; Chen, W.; Lai, Y.; Li, J. *J. ECS Electrochem. Lett.* **2013,** *3,* A8.

46. Lu, J.; Qin, Y.; Du, P.; Luo, X.; Wu, T.; Ren, Y.; Wen, J.; Miller, D. J.; Miller, J. T.; Amine, K. *RSC Adv.* **2013,** *3,* 8276.

47. Wang, F.; Wu, X.; Shen, C.; Wen, Z. *J. Solid State Electrochem.* **2016,** *20,* 1831.

48. Shimizu, K.; Sepunaru, L.; Compton, R. G. *Chem. Sci.* **2016,** *7,* 3364.

49. Sun, M.; Dong, Y.; Zhang, G.; Qu, J.; Li, J. *J. Mater. Chem. A* **2014,** *2,* 13635.

50. Gurlo, A.; Bârsan, N.; Oprea, A.; Sahm, M.; Sahm, T.; Weimar, U. *Appl. Phys. Lett.* **2004,** *85,* 2280.

51. Reddy, M. V.; Yu, T.; Sow, C. H.; Shen, Z. X.; Lim, C. T.; Subba Rao, G. V.; Chowdari, B. V. R. *Adv. Funct. Mater.* **2007,** *17,* 2792.

52. Hao, S.; Zhang, B.; Ball, S.; Wu, J.; Srinivasan, M.; Huang, Y. *J. Mater. Chem. A* **2016,** *4,* 16569.

53. Gunasekara, I.; Mukerjee, S.; Plichta, E. J.; Hendrickson, M. A.; Abraham, K. M. *J. Electrochem. Soc.* **2015,** *162,* A1055.

54. Han, J.; Guo, X.; Ito, Y.; Liu, P.; Hojo, D.; Aida, T.; Hirata, A.; Fujita, T.; Adschiri, T.; Zhou, H.; Chen, M. *Adv. Energy Mater.* **2016,** *6,* 1601933.

55. Geng, D.; Ding, N.; Hor, T. S. A.; Chien, S. W.; Liu, Z.; Wuu, D.; Sun, X.; Zong, Y. *Adv. Energy Mater.* **2016,** *6,* 1502164.

56. McCloskey, B. D.; Valery, A.; Luntz, A. C.; Gowda, S. R.; Wallraff, G. M.; Garcia, J. M.; Mori, T.; Krupp, L. E. *J. Phys. Chem. Lett.* **2013,** *4,* 2989.

57. Baltrusaitis, J.; Cwiertny, D. M.; Grassian, V. H. *Phys. Chem. Chem. Phys.* **2007,** *9,* 5542.

58. Yao, K. P. C.; Kwabi, D. G.; Quinlan, R. A.; Mansour, A. N.; Grimaud, A.; Lee, Y. -L.; Lu, Y. -C.; Shao-Horn, Y. *J. Electrochem. Soc.* **2013,** *160,* A824.

59. Li, Z.; Ganapathy, S.; Xu, Y.; Heringa, J. R.; Zhu, Q.; Chen, W.; Wagemaker, M. *Chem. Mater.* **2017,** *29,* 1577.

60. Ganapathy, S.; Adams, B. D.; Stenou, G.; Anastasaki, M. S.; Goubitz, K.; Miao, X. -F.; Nazar, L. F.; Wagemaker, M. *J. Am. Chem. Soc.* **2014,** *136,* 16335.

61. Radin, M. D.; Rodriguez, J. F.; Tian, F.; Siegel, D. J. *J. Am. Chem. Soc.* **2012,** *134,* 1093.

62. Tamirat, A. G.; Rick, J.; Dubale, A. A.; Su, W. -N.; Hwang, B. -J.; *Nanoscale Horiz.* **2016, 1,** 243.

63. Williams, A. G. B.; Scherer, M. M. *Environ. Sci. Technol*. **2004,** *38,* 4782.

64. Dai, M.; Zhao, L.; Gao, H.; Sun, P.; Liu, F.; Zhang, S.; Shimanoe, K.; Yamazoe, N.; Lu, G. *ACS Appl. Mater. Interfaces* **2017,** *9,* 8919.

Supporting Information for Chapter 4

Materials and Methods

Cathode Preparation. The cathodes were prepared by coating a slurry of carbon nanotubes (CNT) (purchased from Shenzhen Nanotech Port Co., Ltd., diameter 15–30 nm, length 5-15 um, >99.5%, 150–200 m^2/g) and iron (Ш) oxide nanopowder (Fe$_2$O$_3$, Alfa Aesar, α–phase, 98%, 30-50 nm APS Powder) on carbon fibre paper (CFP). In a typical process, the CNT was mixed with Fe$_2$O$_3$ powder and grinded in a mortar with a ratio of CNT:Fe$_2$O$_3$=1:3, and then the mixture powder was added into N-Methyl-2-pyrrolidone (NMP) (Sigma-Aldrich, anhydrous, 99.5%) in a milling bowl milled for 4 hours at 100 rpm. After, the slurry was coated on CFP and the coated sheet was dried at 80 ˚C for 24 hours in a vacuum oven to remove surface adsorbed water after which disks of Ø12.7 mm were punched out. The final active material loading was about 1.5 ~ 2.5 mg. For comparision, the CNT electrode was made by the same process.

Electrolytes. Tetraethylene glycol dimethyl ether (TEGDME, Sigma-Aldrich, >99.5%) solvent was dried for several days over freshly activated molecular sieves (type 4 Å) (Sigma-Aldrich) and lithium bis(trifluoromethane sulfonyl)imide salt (LiTFSI, 99.95%, Aldrich) was dried in a vacuum oven at 80 C for 24 hours. After that, the electrolyte was made by dissolving 0.5 M LiTFSI in TEGDME solvent. All the electrolyte preparations were carried out in an argon filled glovebox (H$_2$O and O$_2$ content of <1 ppm).

Electrochemistry. The Li–O$_2$ battery, comprising a cathode, a glass microfiber separator (Whatman) soaked in the electrolyte, and a lithium metal anode, was assembled in an argon filled glovebox. The battery was subsequently connected to O$_2$ (Linde, 99.9999%) under a pressure of 1.0 bar where it was allowed to equilibrate for 3 hours before testing. Electrochemical cycling tests were performed on a MACCOR 4000 battery cycler.

X-ray diffraction (XRD) measurements. XRD measurements were performed using a PANalytical X'Pert Pro PW3040/60 diffractometer with Cu Kα radiation operating at 45 kV and 40 mA in 2θ ranging from 30 to 70˚. Scans of 30 minutes and 60 minutes each were recorded for the *operand*o Li–O$_2$ batteries that under a complete (dis)charge cycles at the current densities of 0.2 and 0.05 mA/cm^2, respectively. Scans of about 12 hours for *ex-situ* measurement after a complete discharge were performed. Refinement of the diffraction data was carried out using the Rietveld method as implemented in the GSAS program. To more accurately fit the zero-position (effectively positioned at a different height in the cathode) of the Li$_2$O$_2$ diffraction pattern, peaks arising from the current collector as well as carbon paper were excluded from the fitting. When refining the pattern of the crystalline

Li$_2$O$_2$ grown on the surface of Fe$_2$O$_3$/CNT cathode, the Fe$_2$O$_3$ parameters were fixed to values obtained from the refinement results of the Fe$_2$O$_3$ powder.

Scanning Electron Microscopy (SEM). Electrodes were imaged at different stages of (dis)charge. Electrodes were rinsed with tetrahydrofuran (THF) and dried several times prior to analysis. Samples were transferred into the SEM (JEOL JSM-6010LA) under anaerobic conditions, and images were taken using an accelerating voltage of 5 kV.

X–ray photoelectron spectroscopy (XPS). Electrodes were rinsed with tetrahydrofuran (THF) and dried several time. XPS measurements were carried out with a K–alpha Thermo Fisher Scientific spectrometer using a monochromatic Al Kα X–ray source. The measurements were taken by scanning one spot per sample at ambient temperature and with a chamber pressure of about 7–10 mbar. A flood gun was used for charge compensation. All detected spectra were calibrated by the binding energy of C1s in CNT at 284.48 eV.

Titration experiment: We followed the Li$_2$O$_2$ titration process that has been described in detail as published before.[S4.1] The schematic process is shown in **Figure S4.7**. Briefly, the cathodes and separators after discharge were extracted from the battery, and then they were transferred into a glass vial. 5 mL deionized water was injected into the glass vial. After shaking vigorously, the solution was titrated against a standardized 0.005M HCl (Sigma-Aldrich) solution using a drop of phenolphthalein (Sigma-Aldrich) in alcohol as the end-point indicator. After this, three reagents were added in quick succession. 1 mL of a 2 wt% KI ((≥99.5 %, Sigma-Aldrich) solution in H$_2$O$_2$, followed by 1 mL of 3.5 M H$_2$SO$_4$ solution, finally by 2 drop of molybdate-based catalyst solution. The molybdate-based catalyst solution was prepared by combining 1 g of ammonium molybdate (Sigma-Aldrich) with 10 mL of 6N NH$_4$OH (Sigma-Aldrich), to which 3 g of ammonium nitrate (≥98 %, Sigma-Aldrich) was added after which the mixture was diluted to 50 mL using ultrapure H$_2$O. Upon addition of these reagents, the solution in the flask turns yellow due to the formation of I$_2$ which is subsequently titrated against a standardized solution of 0.01M Na$_2$S$_2$O$_3$ (Sigma-Aldrich) to a faint straw color. At this point ~0.5 mL a 1% starch solution (Sigma-Aldrich) is added as an end-point indicator turning the solution a deep blue, and the solution is further titrated until the solution turns colourless.

Iodometric titrations performed on commercially purchased Li$_2$O$_2$ powder (Sigma-Aldrich, 90% purity) with 1 mg of Li$_2$O$_2$ dissolved in 3 mL of ultrapure water yielded a Li$_2$O$_2$ purity of 83.1 ± 1.5% over three titrations, which give an approximate percentage error of 6 - 8 % per titration. The percentage yield of Li$_2$O$_2$ was determined by dividing the amount of Li$_2$O$_2$ titrated (A), by the amount of Li$_2$O$_2$ that would be expected if a 2.0 e⁻ per

Li$_2$O$_2$ reaction occurred during discharge (B). For a 1 mAh discharge capacity, theoretically 18.65 µmols of Li$_2$O$_2$ would be expected to be formed.
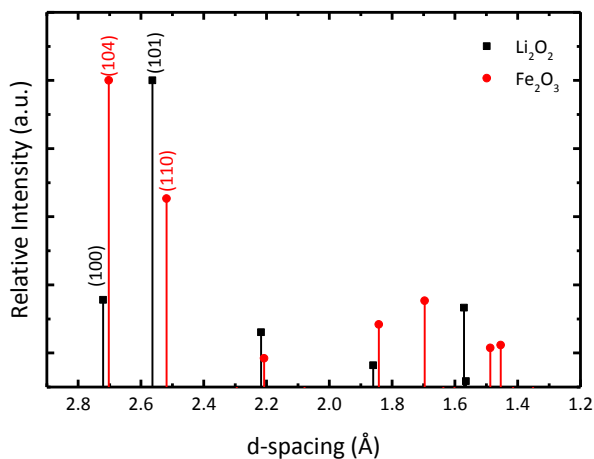
Figure S4.1. Comparison of *d*-spacing between the Li₂O₂ and Fe₂O₃ crystals.
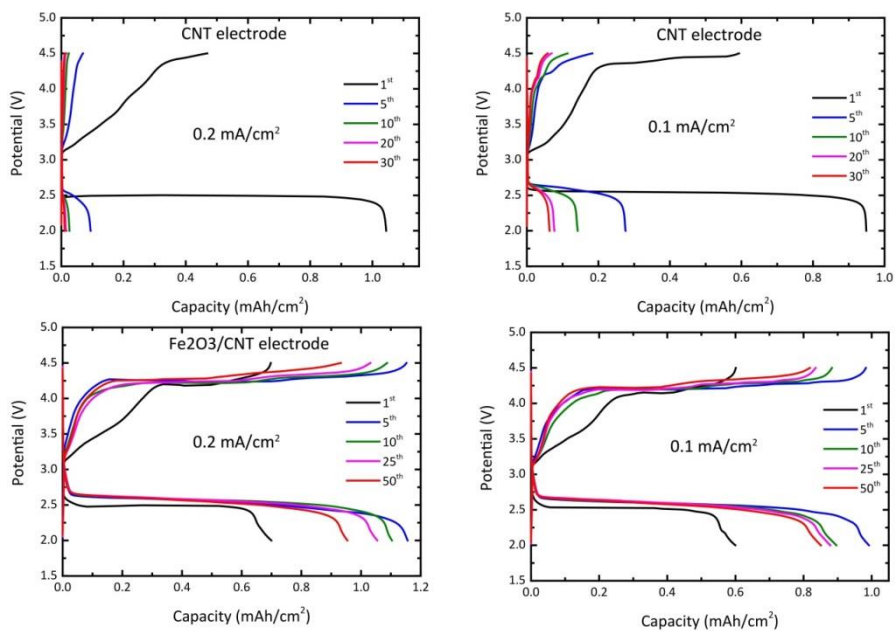
Figure S4.2. Selected potential cut-off galvanostatic (dis)charge voltage curves of CNT and Fe₂O₃/CNT oxygen cathodes at current densities of 0.1 and 0.2 mA/cm² in aprotic Li–O₂ batteries. The specific capacities are calculated based on the geometric area of the electrode.
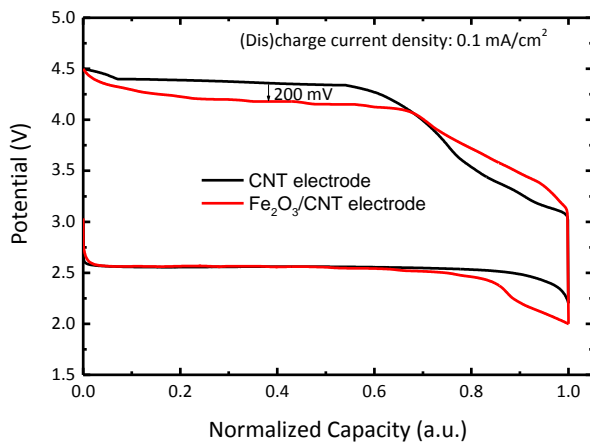
Figure S4.3. Voltage-curve comparison of CNT and Fe$_2$O$_3$/CNT oxygen cathodes in an aprotic Li–O$_2$ battery with normalized capacity.
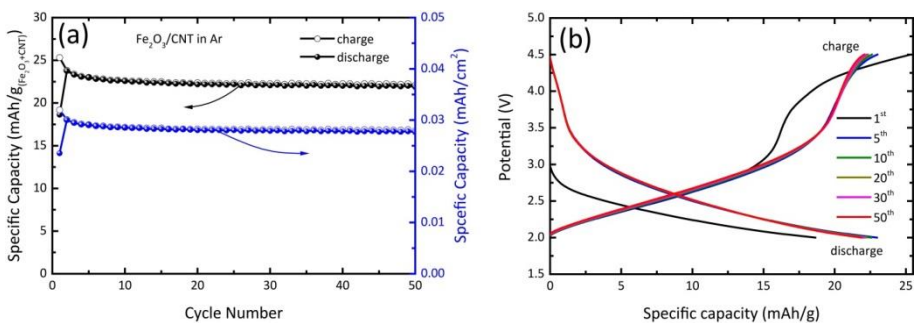
Figure S4.4. Cycling performance of an Fe$_2$O$_3$/CNT oxygen cathode in Ar employing a potential window of 2.0–4.5 V measured at a current density of 0.1 mA/cm^2. (b) Selected potential cut−off, galvanostatic (dis)charge profiles of the Fe$_2$O$_3$/CNT cathode in Ar measured at a current density of 0.1 mA/cm^2.
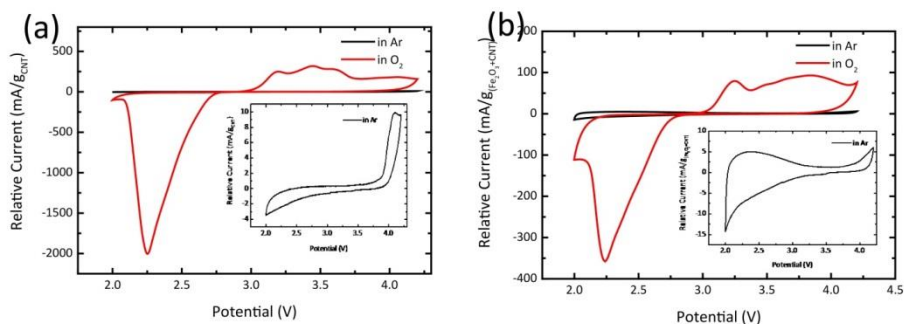
Figure S4.5. Cyclic voltammetry (CV) curves of (a) CNT and (b) Fe₂O₃/CNT cathodes between 2.0 and 4.2 V at a scan rate of 0.1 mV/s in Li-O₂ batteries, respectively. The inset figures show the enlarged view of the CV curve in Ar.
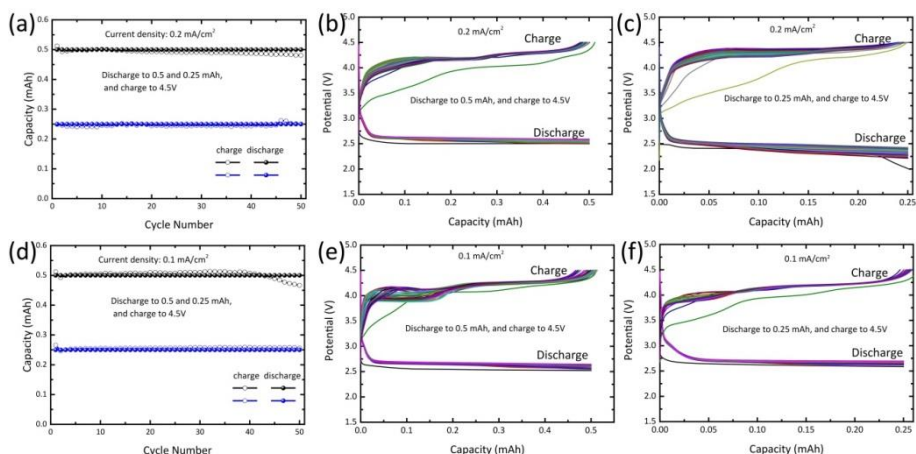
Figure S4.6. Cycling performance and (dis)charge profiles of Fe₂O₃/CNT oxygen cathodes employing a discharge capacity restricted to 0.5 and 0.25 mAh and a charge voltage limited to 4.5 V, respectively measured in a 0.5 M LiTFSI/TEGDME electrolyte at current densities of (a – c) 0.2 mA/cm² and (d – f) 0.1 mA/cm² in Li–O₂ batteries.
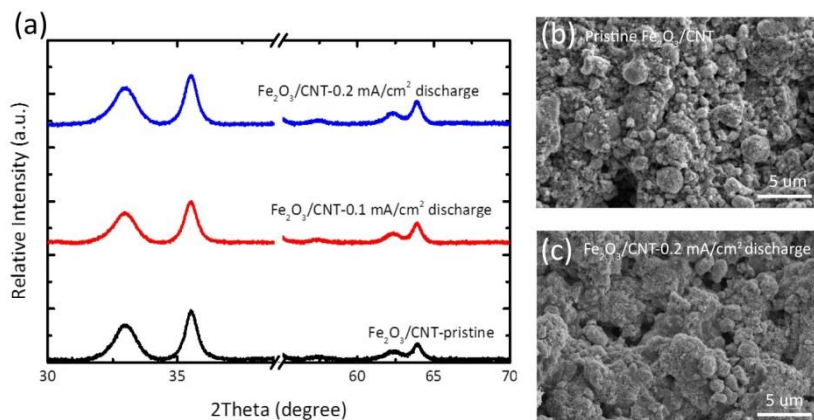
Figure S4.7. (a) XRD patterns of a pristine Fe$_2$O$_3$/CNT cathode and at the end of discharge with the current density of 0.1 and 0.2 mA/cm^2 respectively. SEM images of (b) pristine Fe$_2$O$_3$/CNT cathode and (c) at the end of discharge with a current density of 0.2 mA/cm^2.
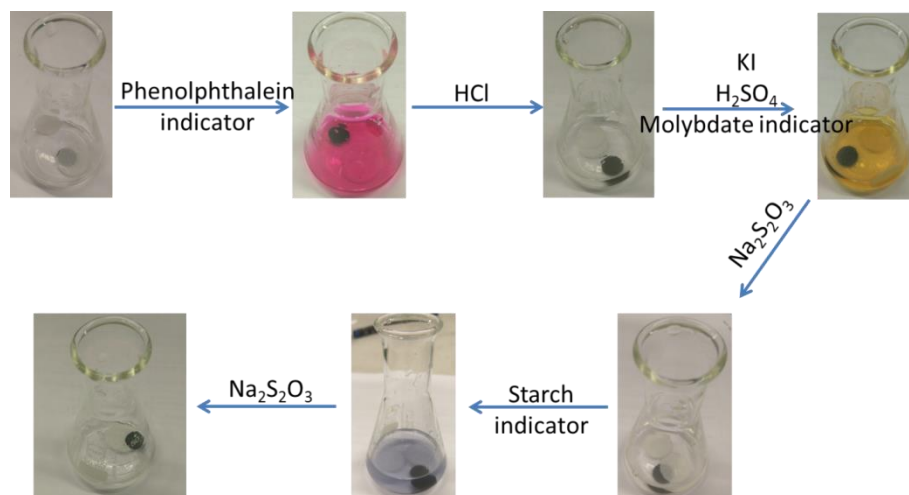
Figure S4.8. Schematic color change pictures of the titration experiment.
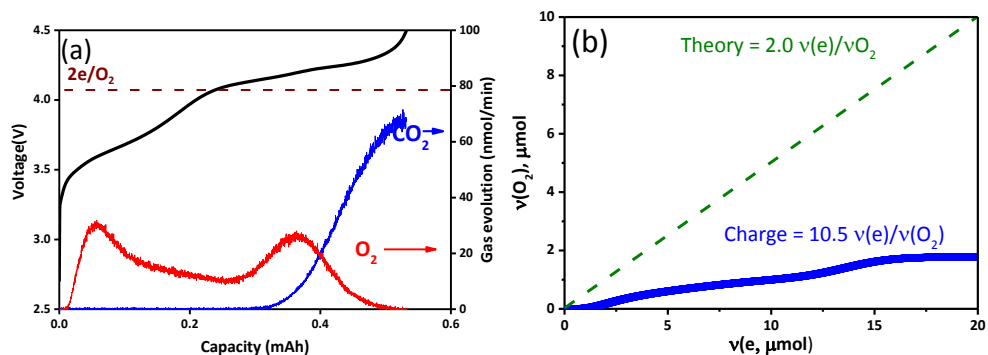
Figure S4.9. Quantitative differential electrochemical mass spectrometry (DEMS) measurements of the Fe$_2$O$_3$/CNT cathode in a Li-O$_2$ battery with a current density of 0.2 mA/cm^2. (a) O$_2$ and CO$_2$ evolution as the function of charge capacity. (b) Comparison of the electrons transport with the theoretical value (the dashed olive line is a 2e$^-$ process) during O$_2$ evolution.
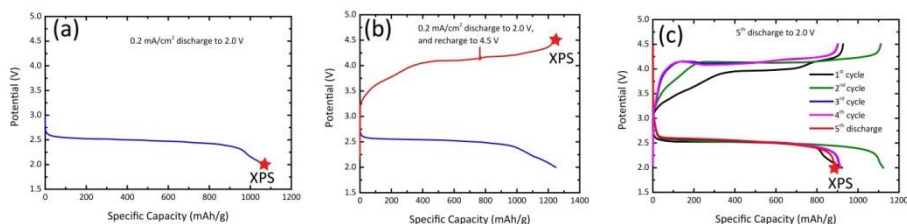
Figure S4.10. The different (dis)charge voltage profiles of Li–O$_2$ batteries with the Fe$_2$O$_3$/CNT cathode run for the *ex-situ* XPS test, measured in a 0.5 M LiTFSI/TEGDME electrolyte at a current density of 0.2 mA/cm2.
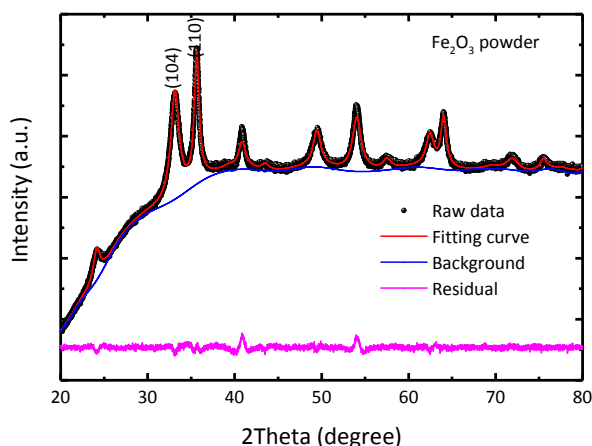
Figure S4.11. The XRD pattern of the Fe$_2$O$_3$ powder along with its Rietveld refinement. (a=b=5.036(0.0002), c=13.773(0.001); average apparent size=13.22(0.05)).
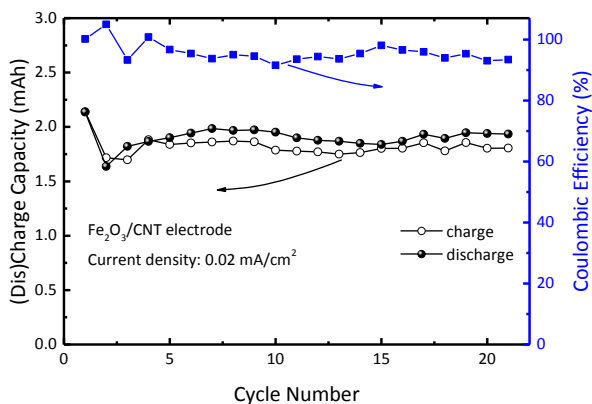
Figure S4.12. Cycling performance of Fe₂O₃/CNT oxygen cathodes during deep (dis)charge by employing a potential window of 2.0–4.5 V measured in 0.5 M LiTFSI/TEGDME electrolyte at a current density of 0.02 mA/cm² in a Li–O₂ battery.
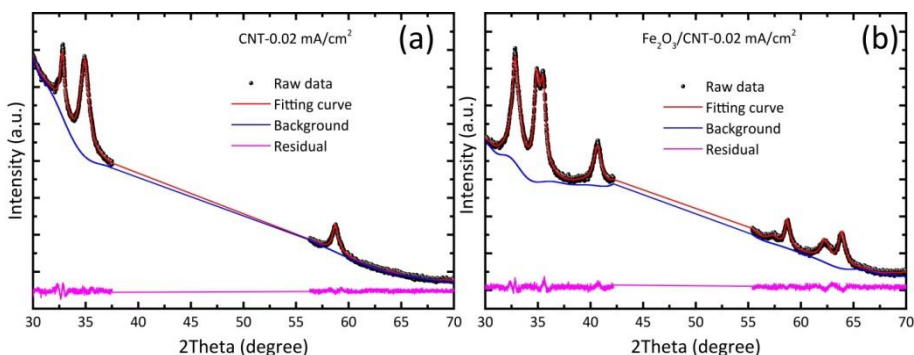
Figure S4.13. The XRD pattern recorded of first complete discharge of CNT and Fe₂O₃/CNT cathodes in an aprotic Li–O₂ battery along with their Rietveld refinement at a current density 0.02 mA/cm². Regions with peaks corresponding to the carbon paper were excluded from the fit. The Fe₂O₃ parameters were fixed based on the refinement results in Figure S9 during the refinement of Li₂O₂ structure.
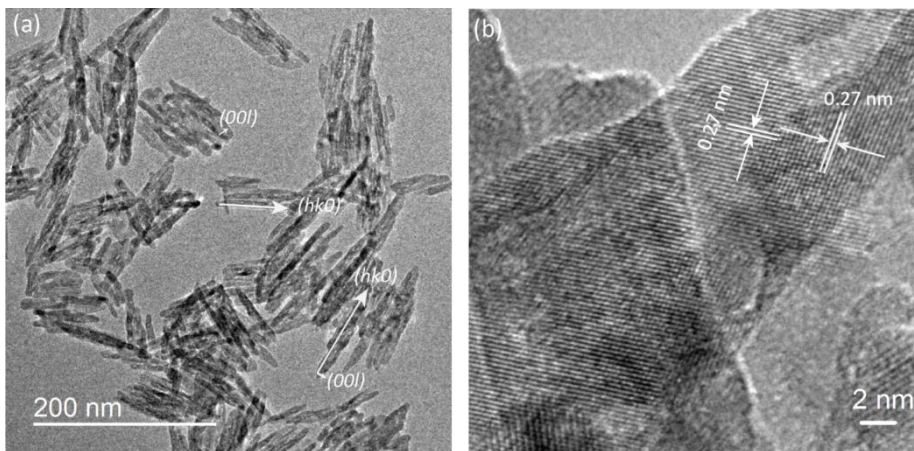
Figure S4.14. High-resolution transmission electron microscopy (TEM) images of Fe$_2$O$_3$ nanoparticles

Table S4.1. Lattice parameters and the average apparent size of Li$_2$O$_2$ on the CNT and Fe$_2$O$_3$/CNT surface respectively, based on the Rietveld refinement results. The lattice parameters for the Fe$_2$O$_3$ powder is also listed based on the refinement of Figure S9. (a=b=5.036(0.0002), c=13.773(0.001); average apparent size=13.22(0.05)).

Discharge current density	Lattice parameters		Average coherent size	Anisotropic value
	a=b (Å)	c (Å)	(nm)	
CNT-0.02 mA/cm^2	3.13496 (0.0002)	7.60256 (0.004)	16.461 (0.119)	142.46 (1.20)
Fe$_2$O$_3$/CNT-0.02 mA/cm^2	3.13739 (0.0001)	7.61898 (0.003)	21.144 (0.282)	64.14 (1.35)

Reference

S4.1 B.D. McCloskey, A. Valery, A. C. Luntz, S. R. Gowda, G. M. Wallraff, J. M. Garcia, T. Mori, L. E. Krupp, *J. Phys. Chem. Lett.* **2013,** *4,* 2989.

Chapter 5

Mechanistic Insight into the Electrochemical Performance of Zn/VO$_2$ Batteries with an Aqueous ZnSO$_4$ Electrolyte

This chapter is based on:
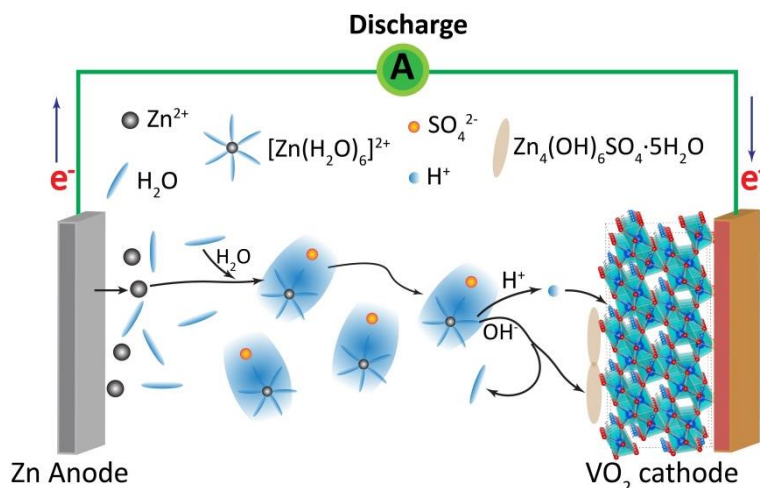
It is proposed that the competition between proton and Zn-ion insertion in the VO$_2$ host is determined by the solvation energy of the salt anion and proton insertion energetics, where proton insertion has the advantage of minimal structural distortion leading to a long cycle life, revealing a reaction mechanism that provides new perspective for the development of aqueous Zn-ion batteries.

Abstract

Rechargeable aqueous zinc-ion batteries (ZIBs) are promising for cheap stationary energy storage. Challenges for Zn-ion insertion hosts are the large structural changes of the host structure upon Zn-ion insertion and the divalent Zn-ion transport, challenging cycle life and power density respectively. Here we demonstrate a new mechanism for the VO$_2$ cathode towards proton insertion accompanied by Zn-ion storage through the reversible deposition of Zn$_4$(OH)$_6$SO$_4$·5H$_2$O on the cathode surface, supported by *Operando* XRD, XPS, neutron activation analysis (NAA) and DFT simulations. This leads to an initial discharge capacity of 272 mAh/g at a current density of 3.0 A/g, of which 75.5% is maintained after 945 cycles. It is proposed that the competition between proton and Zn-ion insertion in the VO$_2$ host is determined by the solvation energy of the salt anion and proton insertion energetics, where proton insertion has the advantage of minimal structural distortion leading to a long cycle life. As the discharge kinetics are capacitive for the first half of the process and diffusion limited for the second half, the VO$_2$ cathode takes the middle road possessing both fast kinetics and high practical capacities revealing a reaction mechanism that provides new perspective for the development of aqueous ZIBs.

5.1 Introduction

Lithium-ion batteries (LIBs) have gained significant success in powering portable electric devices, but they have drawbacks with respect to cost, safety and power density for their application in stationary energy storage devices. The safety issues are related to the flammable organic electrolytes and the growth of lithium dendrites.[1-3] For this reason cheap, rechargeable aqueous batteries are attracting extensive interest based on their high intrinsic safety (replacing flammable organic electrolyte in LIBs), facile and cheap manufacturing (stable versus H$_2$O and O$_2$), and high ionic conductivity (favours high rate capabilities suitable for high power density).[4,5] Among the various aqueous chemistries (aqueous Li- and Na-ion batteries,[4] Zinc-air batteries,[6,7] alkaline-acid Zn-H$_2$O fuel cells,[8] etc.), rechargeable aqueous Zn-ion batteries (ZIBs) with a mild electrolyte are particularly attractive as zinc is more compatible with water than alkaline metals, Zn-ions are divalent, and the production and recycling of these batteries is relatively simple.[9-12]

A variety of manganese dioxide (MnO$_2$) polymorphs (α-, β-, γ-, δ-,and amorphous) have been investigated as cathodes materials for ZIBs.[10,11,13-19] Several studies have demonstrated that the storage capacity of MnO$_2$ in a neutral or mildly acidic aqueous electrolyte is partly induced by a reversible Zn^{2+} insertion/extraction reaction and partly by the reversible H$^+$ insertion/extraction.[10,11,19] This process is governed by the reversible phase transition of the MnO$_2$ polymorphs from a tunnelled to layered structure, driven by the electrochemical reaction. During this phase transition, even though the crystalline structure is maintained, Mn^{3+} in the tunnel chains are reduced to soluable Mn^{2+} leading to a capacity fading, a short cycle life and low Coulombic efficiency of aqueous Zn/MnO$_2$ batteries.[17,20] To prevent this dissolution of Mn ions, alternative electrolytes were identified, for example, Zhang *et al*., found that by using a Zn(CF$_3$SO$_3$)$_2$ aqueous electrolyte, Mn-ion dissolution was suppressed and a high capacity retention with a ZnMn$_2$O$_4$ cathode was achieved.[21] Alternatively by using a MnSO$_4$ additive to a mild ZnSO$_4$ aqueous electrolyte, Pan *et al.* reported that the Mn^{2+} dissolution in the aqueous Zn/MnO$_2$ electrolyte was inhibited.[11] Though research into MnO$_2$ cathodes for aqueous ZIBs has gained momentum, it is of great importance to develop alternative high capacity cathode materials for ZIBs that are stable in an aqueous electrolyte.

Very recently, vanadium oxide and its related compounds have been reported as cathodes for ZIBs, showing higher energy densities and better capacity retention compared to MnO$_2$ cathodes. Senguttuvan *et al.* reported the reversible Zn^{2+} ion insertion/extraction process in the V$_2$O$_5$ cathode for a nonaqueous ZIBs.[22] Kundu *et al.* developed a highly stable vanadium bronze (Zn$_{0.25}$V$_2$O$_5 \cdot n$H$_2$O) cathode for aqueous ZIBs which displayed a high energy density and capacity retention through a reversible Zn^{2+}

(de)intercalation process.[12] In addition, LiV$_3$O$_8$,[23] H$_2$V$_3$O$_8$,[24] and V$_2$S[25] cathodes exhibit good capacity reversibility and power density for aqueous ZIBs. Although Oberholzer *et al.*[26] observed a proton intercalation mechanism for various cathode materials in aqueous ZIBs, Zn/VO$_2$ batteries are reported to follow a dominantly Zn^{2+} insertion/extraction mechanism.[27,28] The precise reaction mechanism of vanadium based cathodes for ZIBs is in many cases unclear and demands detailed investigation.

Here, we demonstrate a highly reversible electrochemical reaction for the VO$_2$ cathode combined with a Zn foil anode and a mild aqueous ZnSO$_4$ electrolyte. Within the voltage window of 0.2 – 1.3 V, the first discharge capacity of 353 mAh/g is delivered at a current density of 1.0 A/g, and 72% of the discharge capacity is maintained after 500 cycles and at a current density of 3.0 A/g, 75.5% is maintained after 945 cycles. By combining *ex-situ* and *operando* XRD measurements, neutron activation analysis (NAA), X-ray photoelectron spectroscopy analysis (XPS), and density functional theory (DFT) analysis, a mechanism is proposed based on the reversible H$^+$ insertion and extraction in the VO$_2$ crystallites during discharge and charge, respectively. *Operando* XRD demonstrates the reversible formation and decomposition of a solid Zn$_4$(OH)$_6$SO$_4$·5H$_2$O species on the electrode surface, concurrent with the H$^+$ insertion and extraction. The competition between H$^+$ and Zn^{2+} insertion appears driven by the nature of the salt anion and the stability of the inserted VO$_2$, and the complementary advantages provide new possibilities for cheap aqueous Zn batteries.

5.2 Results and discussions

5.2.1 Electrochemical performance of Zn/VO$_2$ batteries

The VO$_2$ nanorods were fabricated by a hydrothermal method. The XRD pattern of the as-prepared powder (**Figure 5.1A**), accompanied by the Rietveld refinement results, show that all of the diffraction peaks can be indexed to the monoclinic VO$_2$ (B) phase (space group: C2/m) with lattice constants of a=12.04167(3) Å, b=3.6982(1) Å, c=6.4251(3) Å. It is worth noting that a series of peaks corresponding to the (200), (110), (111), (310), and (020) planes of VO$_2$ are sharper than the peaks corresponding to the (001), (002), and (003) planes, which indicates a high degree of preferred orientation owing to the high width/thickness ratio. Scanning electron microscopy (SEM) images (**Figure 5.1B**) of this material shows the nanorod morphology with a high aspect ratio. The nanorods exhibit a stacked architecture, being a few micrometres in length and tens of nanometres in width. Transmission electron microscopy (TEM) images (**Figure 5.1C** and the inset image) confirm their anisotropic structure as well as their stacked nanorod morphology. The lattic-

resolved HRTEM image (**Figure 5.1C** inset) of the nanorods shows a spacing of 0.353 nm and 0.572 nm, which correspond to the d-spacing of the (110) and (200) planes, respectively. This set of planes dominates the surface of the nanorods and runs parallel to the length of the nanorods, confirming the crystalline growth along the *a*- and *b*-directions.
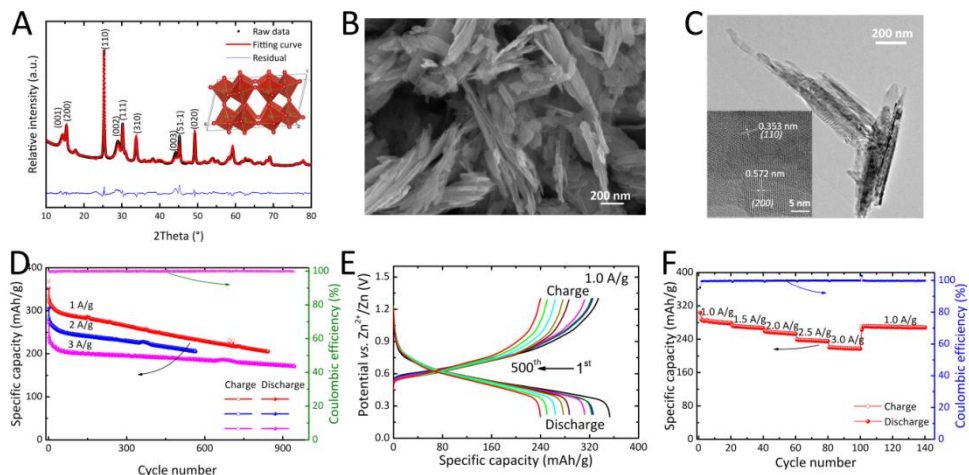
Figure 5.1. (A) XRD pattern and Rietveld refinement as indicated for the crystal structure. (B) SEM image showing the morphology of the prepared VO₂ nanorods. (C) TEM image of the stacked nanorods. Inset: lattice-resolved HRTEM showing the 0.353 nm distance of the (110) planes and 0.572 nm distance of the (200) planes (indicated by the parallel white lines). (D) Cycling performance and the corresponding Coulombic efficiency at different current densities within a voltage window of 0.2 – 1.3 V. (E) Selected galvanostatic discharge and charge profiles at the current density of 1.0 A/g. (F) Rate capability performance and the corresponding Coulombic efficiencies.

An aqueous electrolyte of 1 M $ZnSO_4$, Zn foil as anode, and glass fiber as separator were combined with the VO₂ cathode as aqueous ZIB. **Figure 5.1D** displays the cycling performance of the Zn/VO₂ batteries at different current densities within a voltage window of 0.2 and 1.3 V versus Zn/Zn^{2+}. Large initial discharge capacities of 353, 306, and 272 mAh/g are delivered for the VO₂ cathode at current densities of 1.0 (4.5C), 2.0 (8.9C), and 3.0 A/g (13.4C), respectively. In comparison with the 10th stable cycle, the discharge capacities are maintained at around 65.7%, 76.3%, and 75.5% at the 844th, 565th, and 945th cycle at the current densities of 1.0, 2.0, and 3.0 A/g, respectively. At a current density of 0.05 A/g (**Figure S5.1A**), the initial discharge capacity is 384 mAh/g, of which 70% is maintained after 40 cycles. From the individual voltage curves (**Figures 5.1E** and **Figure S5.1B**), on discharge a sloping plateau is seen from 0.75 to 0.3 V, and subsequently a sloping charge plateau is observed from 0.5 to 1.2 V. This relatively constant discharge

plateau facilitates a stable energy output as compared to for instance Zn$_{0.25}$V$_2$O$_5$·nH$_2$O,[12] which displays several solid-solution phase plateaus on discharge. In addition, the discharge/charge curves show very similar voltage behaviour over multiple cycles indicating a more stable electrochemical reaction mechanism than for Zn/MnO$_2$ aqueous batteries.[11,19] The rate capability of the Zn/VO$_2$ battery is tested at both high (from 1.0 to 3.0 A/g, **Figure 5.1F**) and low current densities (from 0.1 to 1.0 A/g, **Figure S5.1C**). Upon continuous cycling using varying current densities, the specific capacities drop only marginally on doubling/tripling the current rates, suggesting excellent kinetics and stable cycling of the VO$_2$ cathodes and Zn anodes. In addition, the high Coulombic efficiency (≥99.4 %) indicates that marginal side reactions occur in these Zn/VO$_2$ batteries. After 100 cycles, the morphology of the VO$_2$ cathode surface shows no significant change (**Figure S5.2**), indicating a highly stable VO$_2$ cathode structure during the electrochemical process. Based on the reversible capacity at different current densities, approximately 1 mol e$^-$ per VO$_2$ unit is stored during the electrochemical reaction of these Zn/VO$_2$ batteries.

5.2.2 Analysis of the electrode structure during discharge/charge

To investigate the phase evolution during discharge and charge, both *ex-situ* and *operando* XRD patterns were recorded during cycling. **Figure 5.2A** shows the *ex-situ* XRD patterns of a self-supporting VO$_2$ electrode at different discharge/charge states. In the XRD pattern of the pristine electrode, two additional peaks appear at 17.95 and 26.40° which can be attributed to the PTFE binder and CNT present in the electrode (**Figure S5.3A**), and the remaining diffraction peaks can be assigned to the VO$_2$ crystal structure. As the state of discharge progresses, a series of very clear reflections at 2θ values of 12.2°, 24.6°, 32.6°, 35.5°, 58.8°, and 61.9° gradually appear, and subsequently disappear upon charge. These peaks can be indexed to the (001), (002), (-2,3,0), (-3,1,1), (410), and (313) reflections of the Zn$_4$(OH)$_6$SO$_4$·H$_2$O crystalline phase. The formation of Zn$_4$(OH)$_6$SO$_4$·H$_2$O after discharge is more clearly visible in **Figure S5.4A**. The relatively intense (001) reflection indicates the anisotropic growth of the Zn$_4$(OH)$_6$SO$_4$·H$_2$O crystallites. As shown in the SEM images of the electrode after discharge (**Figure S5.5**), the observed anisotropic shape of the flake like surface products can be ascribed to the Zn$_4$(OH)$_6$SO$_4$·H$_2$O crystallites. In addition, the peak positions for the VO$_2$ phase remain unchanged throughout the electrochemical process, however the peak intensities gradually decrease and increase during discharge and charge respectively, which can be attributed to the VO$_2$ particles being covered by the Zn$_4$(OH)$_6$SO$_4$·H$_2$O crystallites (**Figure 5.2A** and **Figure S5.4A**).
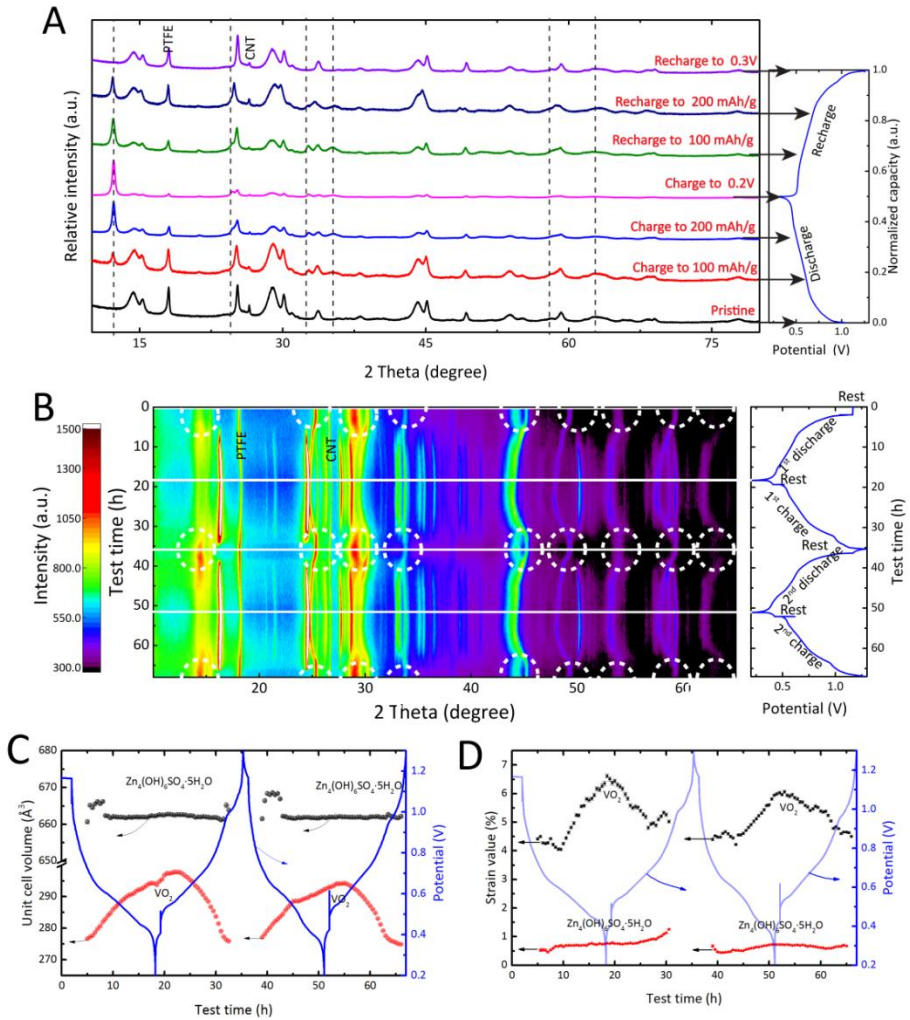
Figure 5.2. (A) Left: *Ex-situ* XRD patterns of the VO₂ electrode at different discharge/recharge states. The marked series of diffraction peaks can be assigned to the Zn₄(OH)₆SO₄·H₂O phase and the remaining peaks belong to the VO₂ phase. Right: The corresponding discharge/charge profiles of the Zn/VO₂ battery. (B) Left: Two-dimensional contour plots of the *operando* XRD patterns showing the 2θ region between 10 – 70˚ during two complete discharge/charge cycles. The marked series of diffraction peaks can be assigned to the VO₂ phase and the rest can be assigned to the Zn₄(OH)₆SO₄·5H₂O phase. Right: The corresponding discharge/charge profiles of the Zn/VO₂ *operando* XRD battery. (C and D) Rietveld refinement result of the *operando* XRD patterns: (C) the evolution of unit cell volume of VO₂ and (D) the evolution of strain values as a function of discharge/charge time.

XRD patterns were also measured under *operando* conditions (**Figure 5.2B**) over two complete discharge/charge cycles. Surprisingly, at various positions the recorded *operando* XRD patterns show different reflections compared to the *ex-situ* XRD patterns (**Figure 5.2A**). A direct comparison of the XRD patterns recorded *operando* and *ex-situ* at the end of discharge is shown in the supporting information in **Figure S5.4B**. As observed in **Figure 5.2B**, a series of peaks can be ascribed to the VO$_2$ phase (marked white circles) before the electrochemical discharge. These VO$_2$ peaks gradually curve and disappear as upon discharging to 0.2 V, and are completely recovered when the battery is subsequently charged to 1.3 V. Concurrently, a series of new reflections appear upon discharge, which can be attributed to Zn$_4$(OH)$_6$SO$_4\cdot$5H$_2$O rather than the Zn$_4$(OH)$_6$SO$_4\cdot$H$_2$O phase observed under *ex-situ* conditions. During the charge process, the reflections of Zn$_4$(OH)$_6$SO$_4\cdot$5H$_2$O gradually disappear on recharging to 1.3 V. These results indicate the reversible formation/decomposition of the Zn$_4$(OH)$_6$SO$_4\cdot$5H$_2$O crystallites on the VO$_2$ electrode during the discharge/charge process. The difference in product observed between the *operando* and *ex-situ* XRD measurements can be explained by the dehydration of Zn$_4$(OH)$_6$SO$_4\cdot$5H$_2$O phase as a consequence of vacuum drying at 80 ˚C prior to the *ex-situ* measurements.[29]

The structural evolution of VO$_2$ has been experimentally and computationally studied for Li, Na, Mg and Al-ion batteries.[30,31] It is especially noteworthy that the intercalation of multivalent Mg and Al-ions into VO$_2$ is typically accompanied by strong deformation of the crystal structure.[30] However, based on our *ex-situ* XRD results, no significant change in the crystalline VO$_2$ was observed, suggesting that the insertion of multivalent Zn^{2+} into the VO$_2$ host does not occur. Recently, researchers have reported that H$^+$ participates in zinc aqueous electrochemistry.[11,19,32] Also, it is well known that protons can insert into the VO$_2$ lattice by a hydrogenation[33-35] in which case the VO$_2$ structure is far less perturbed than when Li, Na, or multivalent ions are inserted. This motivates us to propose a reaction mechanism where a combination of H$^+$ insertion/extraction into the VO$_2$ crystal lattice and the formation/decomposition of the Zn$_4$(OH)$_6$SO$_4\cdot$5H$_2$O occurs on the surface of electrode during the electrochemical discharge/charge process in the aqueous ZnSO$_4$ electrolyte (this reaction mechanism will be discussed later in detail). Rietveld refinement was performed to gain detailed insight into the structural evolution occurring during the *operando* XRD experiment. As shown in **Figure 5.2C**, the refined unit cell volume of Zn$_4$(OH)$_6$SO$_4\cdot$5H$_2$O shows relatively stable values during discharge and charge over two cycles. The *a, b,* and *c*- lattice parameters of Zn$_4$(OH)$_6$SO$_4\cdot$5H$_2$O also show no significant change during battery cycling (**Figure S5.6**). However, small changes are observed in the evolution of the unit cell volume of the VO$_2$ crystallites, expanding by 6.5% upon discharge to 0.2 V, and returning to its original value

after recharge to 1.3 V. The *a, b, and c-* lattice parameters of the VO$_2$ crystallites increase by 2.8%, 2.7%, and 2.3%, respectively after discharge and, like the unit cell volume, decrease to their original values after charge (**Figure S5.7**). The first and second cycle show the same reversible evolution of cell volume and lattice parameter, confirming the reversibility of this process. The evolution of the lattice strain is practically stable for Zn$_4$(OH)$_6$SO$_4$·5H$_2$O (**Figure 5.2D**), whereas for the VO$_2$ crystallites it increases and decreases during discharge and charge, respectively. This can be correlated to proton insertion and extraction, that apparently not only results in the observed volume expansion and shrinkage of the VO$_2$ lattice but also introduces lattice strain. The slight increase in unit cell volume of VO$_2$ at the beginning of charge may be attributed to the decomposition of Zn$_4$(OH)$_6$SO$_4$·5H$_2$O leading to the exposure of more proton containing VO$_2$ crystallites on the electrode surface.
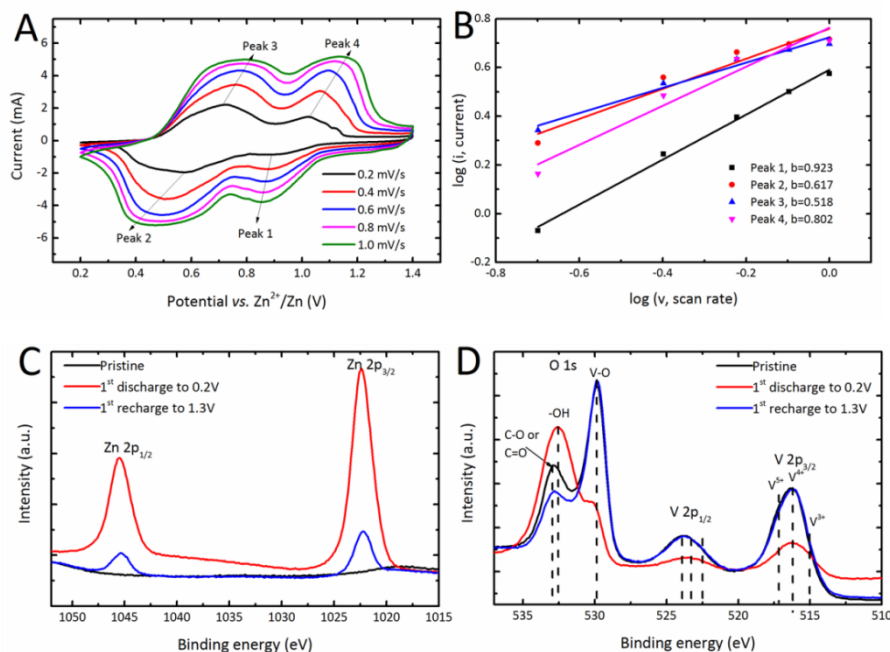
Figure 5.3. (A) CV curves of a Zn/VO$_2$ battery at different scan rates with a voltage window between 0.2 and 1.4 V. (B) Plots of log(i) versus log (v) at specific peak currents extracted from the CV scans. (C and D) XPS spectrum of the pristine VO$_2$ electrode, after the 1st discharge to 0.2 V, and after 1st recharge to 1.3 V respectively at a current density of 50 mA/g. (C) Zn 2p region of the XPS spectra. (D) O 1s and V 2p region of XPS spectra.

To verify the compounds present on the electrode after discharge and charge, neutron activation analysis (NAA) was carried out. This technique allows accurate quantification of the amounts of V and Zn as in VO$_2$ and Zn$_4$(OH)$_6$SO$_4$·H$_2$O through the

integrated element specific Gamma-ray spectra (**Figure S5.8**). During the 1st cycle, the V content in the VO$_2$ electrode (**Figure S5.8A**) decreases as the state of discharge progress and it recovers after the 1st recharge. The Zn content in the electrode (**Figure S5.8B**) exhibits the opposite trend. After the 5th cycle, the V and Zn contents of the VO$_2$ electrodes (**Figures S5.8C and D**) show similar amounts as in the 1st, indicating the electrochemical reaction is reversible. In addition, the exact amount of V and Zn in the electrodes based on the capacity associated with the formation of $Zn_4(OH)_6SO_4 \cdot H_2O$ agrees well with the NAA measured values (**Table S5.1**).

To further understand the kinetics of H$^+$ insertion/extraction in the VO$_2$ electrode, CV measurements at different scan rates are carried out as shown in **Figure 5.3A**. At a scan rate of 0.2 mV/s, two pairs of reduction and oxidation peaks appear at 0.89/0.57 and 0.72/1.02 V (**Figure 5.3A**), respectively. This confirms the redox reaction of VO$_2$ during discharge/charge, indicating at least two different H$^+$ insertion/extraction processes as the left oxidation/reduction pair (peaks 2 and 3) appears to consist of two peaks. On increasing the scan rate from 0.2 to 1.0 mV/s, the CV curves show a similar shape albeit with a gradual shift and broadening of the reduction and oxidation peaks. The peak currents and scan rates in the CV curves follow a relationship as given by:[36]

$$i = av^b$$

Where i and v represents the current and scan rate, respectively, and where a and b are adjustable parameters. The above equation can be also written as $\log(i) = b\log(v) + \log(a)$ where b is typically in the range of 0 - 1.[32] When b equals to 0.5, this indicates that the electrochemical process is governed by ionic diffusion, whereas b equals 1.0, indicates a capacitive storage process. As shown in **Figure 5.3B**, the b-value obtained from the slopes of the four redox peaks are 0.92, 0.62, 0.52, and 0.80 respectively, indicating the electrochemical process of Zn/VO$_2$ batteries is controlled by a combination of ionic diffusion and capacitive behavior. At the beginning of the discharge reaction (reduction peak 1), the H$^+$ insertion into VO$_2$ appears dominating, corresponding to a capacitive process (b=0.923). As the state of discharge goes deeper, more and more $Zn_4(OH)_6SO_4 \cdot 5H_2O$ covers the VO$_2$ surface, hindering proton insertion, and the process is controlled by ionic diffusion (peak 2, b=0.617). For the charge process, this is reversed: as the surface product is decomposed the electrochemistry is first dominated by ionic diffusion followed by more capacitive behaviour.

To further analyse the H$^+$ insertion and extraction process in the VO$_2$ electrode, X-ray photoelectron spectroscopy (XPS) analysis was performed to investigate the chemical
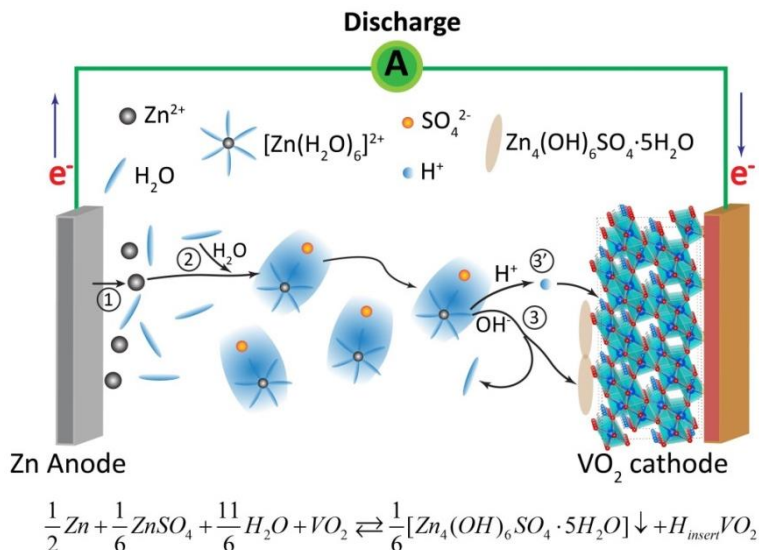
states of the pristine and the 1st discharged/charged electrodes (**Figure 5.3C and D**). The high resolution Zn 2p spectra demonstrates that there is no zinc component in the pristine electrode (**Figure 5.3C**, black line), and after the 1st discharge (**Figure 5.3C**, red line) two representative peaks located at 1045.4 (Zn 2p$_{1/2}$) and 1022.3 eV (Zn 2p$_{3/2}$)[12] are observed, which originate from the Zn$_4$(OH)$_6$SO$_4\cdot$H$_2$O surface compound. The same holds true for the electrode after the 100th discharge (**Figure S5.9A**). The smaller first charge capacity compared to the following cycles (**Figure 5.1D**), indicates that a small amount of the surface zinc compound is left after the 1st charge. This is observed through the relative weaker Zn 2p spectrum after the 1st charge (**Figure 5.3C**, blue line). However, the relative intensity of the irreversible surface Zn compound through the Zn 2p spectrum does not increase much even after the 100th charge (**Figure S5.9A**), suggesting that the first cycle is mainly responsible for the formation of the irreversible surface Zn compound. The high resolution O1s spectra (**Figure 5.3D**, from 535.5 to 527.5 eV) show a relatively complex pattern due to various associations of oxygen atoms with vanadium, zinc, and the surface adsorption groups,[18,32] therefore several possible peaks may coincide within a narrow region. As shown in **Figure 5.3D**, the marked peak positions at 532.8 and 529.8 eV for the pristine electrode (black line) can be assigned to the C-O/C=O (adsorption) and V-O bonds, respectively. After the 1st discharge, the O1s peaks located at 532.8, 532.6, and 529.8 eV (**Figure 5.3D**, red line) can be assigned to oxygen in the C-O/C=O bonds from adsorption groups, -OH bonds from Zn$_4$(OH)$_6$SO$_4\cdot$H$_2$O, V-O and Zn-O bonds from VO$_2$ and Zn$_4$(OH)$_6$SO$_4\cdot$H$_2$O, respectively.[18,33,34] After the 1st charge (**Figure 5.3D**, blue line), the O1s peaks mostly recover to the pristine state, indicating the removal of the formed zinc compounds during discharge. Similar results are also observed after the 100th discharge and charge respectively (**Figure S5.9B**).

The high resolution V2p region (**Figure 5.3D**, from 512.5 to 557.5 eV) contains a doublet peak corresponding to the V 2p$_{1/2}$ and V 2p$_{3/2}$ in VO$_2$. The marked peak positions located at 517.1, 516.3, and 515.0 eV for V $_{2p3/2}$ can be deconvoluted into three peaks, which can be assigned to the binding energy of V^{5+}, V^{4+}, and V^{3+}, respectively.[34,37] The V2p spectra of the pristine and charged electrode overlap well with each other, indicating a highly reversible structural change in VO$_2$ during the electrochemical reaction. Interestingly, the vanadium state of the discharged electrode shows a small shift to V^{3+} compared to the pristine electrode (as shown in **Figure S5.10A,** Supporting Information) when the intensities of XPS V2p spectra for three electrodes are normalized. Normally on zinc insertion in transition metal oxide cathodes, the elemental state of the host materials shows a significant change in the XPS spectra. However, VO$_2$ shows only a very small change after discharge which is in agreement with the *ex-situ* XRD results that indicate that the VO$_2$ structure is maintained. This makes an H$^+$ insertion mechanism more

plausible, since this can be expected to cause small structural changes as compared to Zn^{2+} insertion.

5.3 Mechanistic insights

$$\frac{1}{2}Zn + \frac{1}{6}ZnSO_4 + \frac{11}{6}H_2O + VO_2 \rightleftarrows \frac{1}{6}[Zn_4(OH)_6SO_4 \cdot 5H_2O]\downarrow + H_{insert}VO_2$$

Figure 5.4. Schematic cartoon of the electrochemical process in a Zn/VO$_2$ battery during discharge with a ZnSO$_4$ aqueous electrolyte. Process 1, Zn loses electrons and changes to Zn^{2+}; process 2, hydrolysis of Zn^{2+} ions; process 3 and 3', Zn$_4$(OH)$_6$SO$_4$·5H$_2$O deposition and H$^+$ insertion.

Recently, VO$_2$ has been explored as a cathode for aqueous Zn batteries in combination with various electrolytes. Several reports have proposed that VO$_2$ is able to reversibly store Zn^{2+} when an aqueous Zn(CF$_3$SO$_3$)$_2$ electrolyte is used, based on the pseudo-capacitive behaviour and ultrafast Zn^{2+} kinetics into the unique tunnels of VO$_2$ (B).[28,38,39] However, when an aqueous ZnSO$_4$ electrolyte is used, it appears to follow a very different mechanism. This can be attributed to the lower solvation of the large CF$_3$SO$_3^-$ anions which form a solvation shell around Zn^{2+} cations making it difficult for H$_2$O molecules to approach. In contrast, the smaller SO$_4^{2-}$ anions solvate easily, allowing the formation of hydration sphere around the Zn^{2+} cations.[21] This leads to the formation of zinc hydroxide sulphate compounds [11,17,18,32,40,41] on various cathodes in Zn aqueous batteries when the ZnSO$_4$ electrolyte is used. For instance, in Zn/MnO$_2$ aqueous batteries, ZnSO$_4$[Zn(OH)$_2$]$_3$·xH$_2$O is formed during discharge, leading to the generation of H$^+$ which further reacts with MnO$_2$ to form MnOOH and reversibly transforms back during charge.[11,19] Huang *et al.*[42] further proposed a H$^+$/Zn^{2+} co-insertion/extraction mechanism in

the layered MnO$_2$ cathode, which represents an electrolyte-involved generation/dissolution of flake like zinc hydroxide sulfate on the cathode surface. Park *et al.*[40] and Chen *et al.*[27] proposed a Zn^{2+} intercalation mechanism due to the open-structure of VO$_2$ in a ZnSO$_4$ aqueous electrolyte. However, based on their observation of Zn$_4$(OH)$_6$SO$_4$·5H$_2$O surface products and unchanged VO$_2$ phase after discharge, the presently proposed mechanism based on proton insertion appears more reasonable.

Here we propose that the reaction mechanism of zinc aqueous batteries is highly dependent on the anion and Zn^{2+} cation species present in the aqueous electrolytes. From the present results, we deduce that the H$^+$ insert/extract in/from the VO$_2$ lattice during discharge/charge, concurrent with the formation and decomposition of Zn$_4$(OH)$_6$SO$_4$·5H$_2$O products on the electrode surface in Zn/VO$_2$ batteries when a aqueous ZnSO$_4$ electrolyte is used. In ZnSO$_4$ aqueous solutions, Zn^{2+} ions are normally coordinated with H$_2$O molecules to form [Zn(H$_2$O)$_6$]$^{2+}$[17,43,44] (**Figure 5.4**, process 2) , followed by spontaneous hydrolysis because of the strong polarization induced by the high charge density of the central divalent cation as shown in the reaction below:[17]

$$[Zn(H_2O)_6]^{2+} + H_2O \rightleftarrows [Zn(H_2O)_{6-x}(OH)_x]^{(2-x)+} + xH_3O^+ \quad (1)$$

$$H_3O^+ \rightleftarrows H^+ + H_2O \quad (2)$$
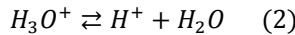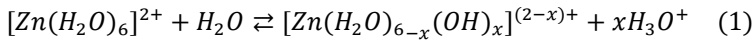
The degree of hydrolysis is strongly influenced by the equilibrium constant (K) and the pH of the solution. It is well known that an aqueous ZnSO$_4$ solution is a weakly acidic (pH ~ 4) at room temperature,[17,21] where x in the reaction (1) is estimated to be close to 2. During the discharge process of the Zn/VO$_2$ battery, H$^+$ is continuously inserted into VO$_2$ promoting the formation of [Zn(H$_2$O)$_4$(OH)$_2$] (**Figure 5.4**, process 3 and 3'), which we propose to result in the following reaction:

$$3[Zn(H_2O)_4(OH)_2] + ([Zn(H_2O)_6]^{2+} + SO_4{}^{2-})_{electrolyte} \rightarrow Zn_4(OH)_6SO_4 \cdot 5H_2O$$
$$\downarrow +13H_2O \quad (3)$$
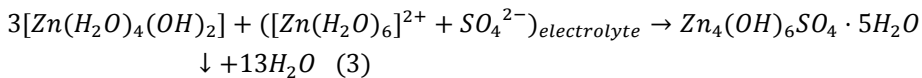
According to the discharge capacity, there is approximately 1 mol e$^-$ per VO$_2$ unit stored. As a result, about 1 molar H$^+$ is inserted into VO$_2$ to maintain charge neutrality. Summarizing, the proposed electrochemical reaction of the Zn/VO$_2$ battery in an aqueous ZnSO$_4$ electrolyte is proposed as follows:

Anode:
$$\frac{1}{2}Zn \rightleftarrows \frac{1}{2}Zn^{2+} + e^- \quad (4)$$

$$\frac{1}{2} Zn^{2+} + 3H_2O \rightleftarrows \frac{1}{2} [Zn(H_2O)_6]^{2+} \quad (5)$$

$Cathode$:

$$\frac{1}{2} [Zn(H_2O)_6]^{2+} + (\frac{1}{6} [Zn(H_2O)_6]^{2+} + \frac{1}{6} SO_4{}^{2-})_{electrolyte} \rightleftarrows \frac{1}{6} [Zn_4(OH)_6SO_4 \cdot 5H_2O] \downarrow$$
$$+ \frac{13}{6} H_2O + H^+ \quad (6)$$

$$H^+ + e^- + VO_2 \rightleftarrows H_{insert}VO_2 \quad (7)$$

$Overall$:
$$\frac{1}{2} Zn + \frac{1}{6} ZnSO_4 + \frac{11}{6} H_2O + VO_2 \rightleftarrows \frac{1}{6} [Zn_4(OH)_6SO_4 \cdot 5H_2O] + H_{insert}VO_2 \quad (8)$$
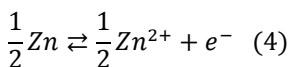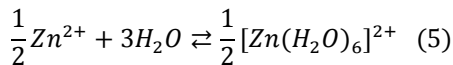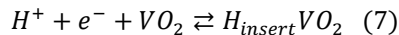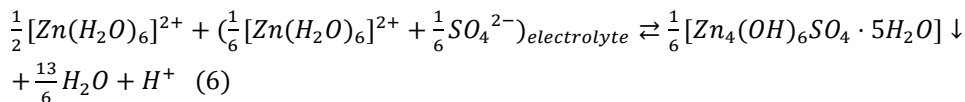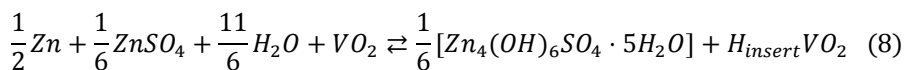
The proton insertion and the Zn₄(OH)₆SO₄·5H₂O formation are coupled through equations (6) and (7) and responsible for the discharge capacity. This mechanism indicates that the role of the VO₂ host is very different from those reported, where Zn-ions participate or even dominate the insertion reactions. The proposed proton insertion mechanism will lead to minimal structural distortion compared to Zn^{2+} insertion, which can be expected to be favourable for a long cycle life. The reversibility and rate performance of these ZIBs therefore relies on the reversible deposition and decomposition of the Zn₄(OH)₆SO₄·5H₂O product on the surface of the VO₂ nanorods. This requires the availability of sufficient VO₂ surface to prevent thick deposits that passivate the Zn storage reaction. It can be expected that a larger surface area allows a larger capacity of this deposition product, however limited by the maximum proton insertion capacity of the VO₂ electrode. Clearly, the SO₄$^{2-}$ anions in the Zn₄(OH)₆SO₄·5H₂O surface product originate from the electrolyte. Therefore, the capacity is limited by the available salt in the electrolyte, or by the amount of VO₂ as the V^{4+}/V^{3+} redox upon H$^+$ insertion is necessary to balance the Zn₄(OH)₆SO₄·5H₂O capacity. As the discharge is capacitive for the first half of the, representing proton insertion, and diffusion limited for the second half, representing proton diffusion through the thickening surface deposit, as discussed around **Figure 3**, the present mechanism involving VO₂ in a ZnSO₄ containing aqueous electrolyte takes the middle road possessing both fast kinetics and high practical capacities which we expect to be tuneable by the available VO₂ surface.
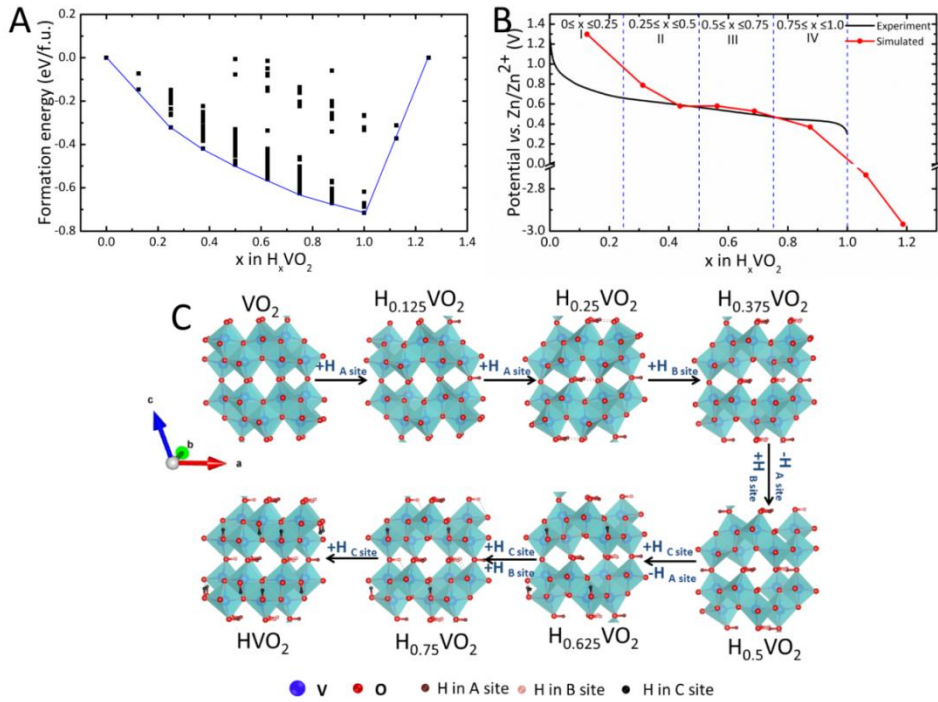
Figure 5.5. First-principle analysis of H Intercalation in VO_2. (A) Formation energies of H_xVO_2 ($0 \leq x \leq 1.25$) configurations per formula unit. The blue line represents the convex hull which comprises the most stable ground state structures determined in each case referenced to the VO_2 and $H_{1.25}VO_2$ endmembers. (B) Voltage determined for H^+ insertion into VO_2, from the total energies between consecutive points on the convex hull at 0 K (red line). The experimental voltage curve (black line) is shown for comparison. (C) Sequence of the lowest energy configurations corresponding to various H_xVO_2 ($0 \leq x \leq 1$) configurations, some of which fall on the convex hull, showing the sequential insertion of H^+ into the VO_2 lattice. The subscripts (A, B and C) for H indicate the preferred sites for H insertion in the corresponding composition range.

5.3.1 Energetics of H⁺ insertion

To validate our proposed H^+ insertion and $Zn_4(OH)_6SO_4 \cdot 5H_2O$ deposition mechanism (**Equation 8**), a detailed first-principle investigation is carried out to analyse energetics of H^+ insertion into the VO_2 lattice. Previous studies have demonstrated the possible insertion sites for Li, Mg and Zn ions in a VO_2 crystal.[30,31,40] Similar to lithium intercalation into VO_2[31] and TiO_2[45,46], the VO_2 lattice can potentially host 1.25 H per formula unit according to the calculated voltage as discussed below,[31] which is higher than the theoretical capacity assumed before. The VO_2 supercell used in our calculations, is constructed *via* a 2 fold repetition along the b-axis containing 8 formula units (**Figure**

S5.11A), and three different kinds of H insertion sites (A, B and C) are determined covering the composition range of $0 \leq x \leq 1.25$ in H$_x$VO$_2$ (**Figure S5.11B**). By determining the symmetrically inequivalent H$^+$/vacancy configurations in the concentration range of $0 \leq x \leq 1.25$ for H$_x$VO$_2$, the thermodynamics of this process can be investigated. The resulting formation enthalpies, defined per H$_x$VO$_2$ formula unit, of the 287 H$^+$/vacancy configurations are shown in **Figure 5.5A**. The detailed method including the formation enthalpy and voltage calculations are provided in the supporting information. The convex-hull (**Figure 5.5A**), connects the stable ground states at 0 K as a function of H-composition, which is indicative of the thermodynamic path that will be followed during the protonation of VO$_2$ assuming entropy contributions are small. From the consecutive points on the convex hull, the average voltage between these compositions is determined (**Figure 5.5B**, red curve).

To understand the protonation mechanism in VO$_2$ the lowest energy, H$^+$/vacancy configurations are shown in **Figure 5.5C**, for the concentration range $0 \leq x \leq 1.0$ in H$_x$VO$_2$. At low H concentrations (0 < x < 0.25), all the lowest energy configurations near the convex-hull show proton insertion at the A sites, implying a two phase transformation at the beginning of discharge. When the A sites are occupied, the protons are positioned at the centre of four O atoms that bridge the V$_4$O$_{10}$ bilayers (**Figure 5.5C**). At H$_{0.25}$VO$_2$, the vertical distance between the two V$_4$O$_{10}$ bilayers increases, and as a consequence, the protons occupying the A sites no longer align themselves in the middle of the b axis tunnel.[31] As the H concentration x increases from 0.25 to 0.5, the protons start to insert onto the B sites. Interestingly, at x=0.5 in the lowest energy configuration, protons occupy half each of the A and B sites, which also results in the largest geometrical change of the VO$_2$ structure. This may explain the observed nonlinear increase in unit cell volume during discharge as shown in **Figure 5.2C**. As the proton concentration x increases from 0.5 to 1.0, some C sites are occupied, and the A sites are fully filled. From the relaxed structures it can be seen that the *a, b,* and *c* – lattice parameters of the VO$_2$ crystallites continuously expand on increasing protonation by about 3.55%, 7.37%, and 4.12%, respectively (**Table S5.2**). This is agreement with the lattice parameter changes observed by *operando* XRD during discharge (**Figure 5.2B**). A comparison of the normalized lattice parameters and unit cell volume obtained from the Rietveld refinement (**Figure 5.2C** and **Figure S5.7**) and the from the lowest energy relaxed structures obtained from first principle simulations (**Table S5.2**) is provided in **Figure S5.12** in the supporting information. The evolution of the *a*- and *c*-lattice (**Figure S5.12 A** and **C**) parameters and unit cell volume (**Figure S5.12D**) of H$_x$VO$_2$ as a function of increasing H concentration are in good agreement. The deviation between the experimental and simulated values of the *b*- lattice parameter at H$_{0.375}$VO$_2$ and H$_{0.5}$VO$_2$ (**Figure S5.12B**) may occur because the large expansion along the b direction

results in very low formation energies at these proton concentrations, however, the inflection points are observed for the same concentration, both experimentally and computationally. At x=1.0, half of the C sites are occupied, and further insertion on the C sites is not possible as this leads to negative voltages versus Zn-metal (**Figure 5.5B**, red curve). Based on the structure and voltage evolution of VO$_2$ as a function of increasing proton concentration, four different regions can be observed (**Figure 5.5B**), similar to what has been observed for the insertion of Li-ions into VO$_2$ and TiO$_2$.[31,45,46] The simulated and experimental voltage profiles are compared in **Figure 5.5B**, indicating a good qualitative agreement. For $0 \leq x \leq 0.25$ a sloping solid-solution like phase plateau is observed corresponding to the H$^+$ insertion onto the A sites. When the H$^+$ concentration x increases from 0.25 to 0.5, a two phase transition (I to II, **Figure 5.5B**) occurs corresponding to proton insertion onto the B sites. Finally in the concentration range of $0.5 \leq x \leq 1.0$, the voltage shows a two-phase transition (II to III, and III to IV, **Figure 5.5B**) which corresponds to the H$^+$ rearrangement on the A and B sites and further H$^+$ insertion onto the C sites.

5.4 Conclusions

The electrochemical reaction in rechargeable aqueous ZIBs depends to a large extent on the combination of the electrode and electrolyte used. Research on MnO$_2$[10] and VO$_2$[28,38] cathodes for aqueous ZIBs have demonstrated multivalent Zn-ion intercalation reactions for Zn(CF$_3$SO$_3$)$_2$ electrolytes. However, when using an aqueous ZnSO$_4$ electrolyte, the zinc hydroxide sulphate compounds and H$^+$ are found to participate in the electrochemical process, and therefore contributing to the electrochemical energy storage.[11,13,19] Our *operando* XRD results confirm the reversible formation and decomposition of Zn$_4$(OH)$_6$SO$_4$·5H$_2$O during discharge and charge of Zn/VO$_2$ batteries when an aqueous ZnSO$_4$ electrolyte is used. However, to explain the voltage profile and storage capacity observed, we propose a concurrent H$^+$ insertion/extraction into the VO$_2$ lattice, corroborated experimentally and consistent with first-principle simulations. The minimal structural changes induced by H$^+$ insertion into VO$_2$ are anticipated to contribute to the long cycle life. The kinetics on discharge are, initially determined by the Zn$_4$(OH)$_6$SO$_4$·5H$_2$O deposition, and later by the proton insertion into VO$_2$, both of which are relatively fast, given the excellent rate performance of the (dis)charge reactions. We suggest a competition between H$^+$ and Zn^{2+} insertion, determined by the stability of the deposited compound as well as the H$^+$/Zn^{2+} energetics in the vanadium oxide host. These mechanistic insights will enable further development of appropriate salt and host materials, balancing the advantages and disadvantages of H$^+$ and Zn^{2+} insertion for aqueous metal-ion batteries with high performance, in particular suitable for safe and cheap stationary batteries.

References

1. Larcher, D.; Tarascon, J. M. *Nat. Chem.* **2014**, *7*, 19.

2. Goodenough, J. B.; Park, K. S. *J. Am. Chem. Soc.* **2013**, *135*, 1167.

3. Liu, B.; Zhang, J.-G.; Xu, W. *Joule* **2018**, *2*, 833.

4. Kim, H.; Hong, J.; Park, K.-Y.; Kim, H.; Kim, S.-W.; Kang, K. *Chem. Rev.* **2014**, *114*, 11788.

5. Malik, R. *Joule* **2017**, *1*, 17.

6. Cai, P.; Li, Y.; Chen, J.; Jia, J.; Wang, G.; Wen, Z. *ChemElectroChem* **2018**, *5*, 589.

7. Cai, P.; Peng, X.; Huang, J.; Jia, J.; Hu, X.; Wen, Z. *Sci. China Chem.* **2019**, *62,* 385.

8. Cai, P.; Li, Y.; Wang, G.; Wen, Z. *Angew. Chem. Int. Ed.* **2018**, *57*, 3910.

9. Parker, J. F.; Chervin, C. N.; Pala, I. R.; Machler, M.; Burz, M. F.; Long, J. W.; Rolison, D. R. *Science* **2017**, *356*, 415.

10. Zhang, N.; Cheng, F.; Liu, J.; Wang, L.; Long, X.; Liu, X.; Li, F.; Chen, J. *Nat. Commun.* **2017**, *8*, 405.

11. Pan, H.; Shao, Y.; Yan, P.; Cheng, Y.; Han, K. S.; Nie, Z.; Wang, C.; Yang, J.; Li, X.; Bhattacharya, P.; Mueller, K. T.; Liu, J. *Nat. Energy* **2016**, *1*, 16039.

12. Kundu, B. D.; Adams, D.; Duffort, V. S.; Vajargah, H.; Nazar, L. F. *Nat. Energy* **2016**, *1*, 16119.

13. Xu, C.; Li, B.; Du, H.; Kang, F. *Angew. Chem. Int. Ed.* **2012**, *51*, 933.

14. Alfaruqi,M. H.; Gim, J.; Kim, S.; Song, J.; Jo, J.; Kim, S.; Mathew, V.; Kim, J. *J. Power Sources* **2015**, *288*, 320.

15. Alfaruqi, M. H.; Gim, J.; Kim, S.; Song, J.; Pham, D. T.; Jo, J.; Xiu, Z.; Mathew, V.; Kim, J. *Electrochem. Commun.* **2015**, *60*, 121.

16. Alfaruqi, M. H.; Mathew, V.; Gim, J.; Kim, S.; Song, J.; Baboo, J. P.; Choi, S. H.; Kim, J. *Chem. Mater.* **2015**, *27*, 3609.

17. Lee, B.; Lee, H. R.; Kim, H.; Chung, K. Y.; Cho, B. W.; Oh, S. H. *Chem. Commun.* **2015**, *51*, 9265.

18. Islam, S.; Alfaruqi, M. H.; Mathew, V.; Song, J.; Kim, S.; Kim, S.; Jo, J.; Baboo, J. P.; Pham, D. T.; Putro, D. Y.; Sun, Y.-K.; Kim, J. *J. Mater. Chem. A* **2017**, *5*, 23299.

19. Sun, W.; Wang, F.; Hou, S.; Yang, C.; Fan, X.; Ma, Z.; Gao, T.; Han, F.; Hu, R.; Zhu, M.; Wang, C. *J. Am. Chem. Soc.* **2017**, *139*, 9775.

20. Lee, B.; Yoon, C. S.; Lee, H. R.; Chung, K. Y.; Cho, B. W.; Oh, S. H. *Sci. Rep.* **2014**, *4*, 6066.

21. Zhang, N.; Cheng, F.; Liu, Y.; Zhao, Q.; Lei, K.; Chen, C.; Liu, X.; Chen, J. *J. Am. Chem. Soc.* **2016**, *138*, 12894.

22. Senguttuvan, P.; Han, S.-D.; Kim, S.; Lipson, A. L.; Tepavcevic, S.; Fister, T. T.; Bloom, I. D.; Burrell, A. K.; Johnson, C. S. *Adv. Energy Mater.* **2016**, *6*, 1600826.

23. Alfaruqi, M. H.; Mathew, V.; Song, J.; Kim, S.; Islam, S.; Pham, D. T.; Jo, J.; Kim, S.; Baboo, J. P.; Xiu, Z.; Lee, K.-S.; Sun, Y.-K.; Kim, J. *Chem. Mater.* **2017**, *29*, 1684.

24. He, P.; Quan, Y.; Xu, X.; Yan, M.; Yang, W.; An, Q.; He, L.; Mai, L. *Small* **2017**, 13, 1702551.

25. He, P.; Yan, M.; Zhang, G.; Sun, R.; Chen, L.; An, Q.; Mai, L. *Adv. Energy Mater.* **2017**, *7*, 1601920.

26. Oberholzer, P.; Tervoort, E.; Bouzid, A.; Pasquarello, A.; Kundu, D. *ACS Appl. Mater. Interfaces* **2019**, *11*, 674.

27. Chen, L.; Ruan, Y.; Zhang, G.; Wei, Q.; Jiang, Y.; Xiong, T.; He, P.; Yang, W.; Yan, M.; An, Q.; Mai, L. *Chem. Mater.* **2019**, DOI: 10.1021/acs.chemmater.8b03409.

28. Ding, J.; Du, Z.; Gu, L.; Li, B.; Wang, L.; Wang, S.; Gong, Y.; Yang, S. *Adv. Mater.* **2018**, *30*, 1800762.

29. Moezzi, A.; Cortie, M. B.; McDonagh, A. M. *Dalton Trans.* **2013**, *42*, 14432.

30. Kulish, V. V.; Koch, D.; Manzhos, S. *Phys. Chem. Chem. Phys.* **2017**, *19*, 22538.

31. Li, S.; Liu, J.-B.; Wan, Q.; Xu, J.; Liu, B.-X. *Chem. Mater.* **2017**, *29*, 10075.

32. Wan, F.; Zhang, L.; Dai, X.; Wang, X.; Niu, Z.; Chen, J. *Nat. Commun.* **2018**, *9*, 1656.

33. Chen, Y.; Wang, Z.; Chen, S.; Ren, H.; Wang, L.; Zhang, G.; Lu, Y.; Jiang, J.; Zou, C.; Luo, Y. *Nat. Commun.* **2018**, *9*, 818.

34. Yoon, H.; Choi, M.; Lim, T.-W.; Kwon, H.; Ihm, K.; Kim, J. K.; Choi, S.-Y.; Son, J. *Nat. Mater.* **2016**, *15*, 1113.

35. Filinchuk, Y.; Tumanov, N. A.; Ban, V.; Ji, H.; Wei, J.; Swift, M. W.; Nevidomskyy, A. H.; Natelson, D. *J. Am. Chem. Soc.* **2014**, *136*, 8100.

36. Brezesinski, T.; Wang, J.; Tolbert, S. H.; Dunn, B. *Nat. Mater.* **2010**, *9*, 146.

37. Silversmit, G.; Depla, D.; Poelman, H.; Marin, G. B.; De Gryse, R. *J. Electron Spectros. Relat. Phenomena* **2004**, *135*, 167.

38. Wei, T.; Li, Q.; Yang, G.; Wang, C. *J. Mater. Chem. A* **2018**, *6*, 8006.

39. Dai, X.; Wan, F.; Zhang, L.; Cao, H.; Niu, Z. *Energy Storage Mater.* **2019**, *17,* 143.

40. Park, J.-S.; Jo, J. H.; Aniskevich, Y.; Bakavets, A.; Ragoisha, G.; Streltsov, E.; Kim, J.; Myung, S.-T. *Chem. Mater.* **2018**, *30*, 6777.

41. B. Sambandam, V. Soundharrajan, S. Kim, M. H. Alfaruqi, J. Jo, S. Kim, V. Mathew, Y.-K. Sun, J. Kim, *J. Mater. Chem. A* **2018**, *6*, 3850.

42. Huang, J.; Wang, Z.; Hou, M.; Dong, X.; Liu, Y.; Wang, Y.; Xia, Y. *Nat. Commun.* **2018**, *9*, 2906.

43. Zhao, Q.; Huang, W.; Luo, Z.; Liu, L.; Lu, Y.; Li, Y.; Li, L.; Hu, J.; Ma, H.; Chen, J. *Sci. Adv.* **2018**, *4*: eaao1761.

44. Nguyen-Trung, C.; J. Bryan, C.; Palmer, D. A. *Struc. Chem.* **2004**, *15*, 89.

45. Dalton, A. S.; Belak, A. A.; Van der Ven, A. *Chem. Mater.* **2012**, *24*, 1568.

46. Armstrong, A. R.; Arrouvel, C.; Gentili, V.; Parker, S. C.; Islam, M. S.; Bruce, P. G. *Chem. Mater.* **2010**, *22*, 6426.

Supporting Information for Chapter 5

Full experimental details and characterization, including computational method, and additional electrochemical performance, SEM images, XRD patterns, XPS spectra, neutron radiation analysis spectra and Rietveld refinement results.

Methods

Synthesis of VO$_2$ nanorods. VO$_2$ nanorods were fabricated by a hydrothermal method. In a typical synthesis, 1 g V$_2$O$_5$ powder was added into a 30 mL deionized water and ethylene glycol (EG) mixture solution with a volum ratio of 3:2. After vigorously stirring for 2 hours, the suspension mixture was transfered into a 45 mL Teflon-lined autoclave and maintained at 180 ˚C for 5 hours. The obtained products was collected by centrifugation, and washed with deionized water several times, then dried in a vacuum oven at 80 ˚C for 12 hours.

Charaterization. X-ray diffraction (XRD) measurements were performed by using a PANalytical X'Pert Pro PW3040/60 diffractometer with Cu Kα radiation operating at 45 kV and 40 mA in an angular 2θ ranging from 10 to 80˚. Scanning electron microscopy (SEM) images were obtained on JEOL JSM-6010LA microscope. X–ray photoelectron spectroscopy (XPS) measurements were carried out with a K–alpha Thermo Fisher Scientific spectrometer using a monochromatic Al Kα X–ray source. The measurements were taken by scanning one spot per sample at ambient temperature. A flood gun was used for charge compensation.

Electrode preparation. The electrodes used to test cycle performance were prepared by coating a slurry on carbon fibre paper (CFP). The slurry was prepared by blending the prpared VO$_2$ powder, Super P and carboxymethyl cellulose (CMC) in deionized water with a weight ratio of 7:2:1 to obtain a slurry. After drying at 80 ˚C for 24 hours in a vacuum oven, 1.266 cm^2 circle pieces were punched from the sheets. Self-supporting electrode for *ex-situ* XRD and XPS measurements were fabricated by blending VO$_2$ powder, carbon nanotubes (CNT) (purchased from Shenzhen Nanotech Port Co., Ltd., diameter 15-30 nm, length 5-15 um, >99.5%, 150–200 m^2/g), and polytetrafluoroethylene (PTFE) in a weight ratio of 7:2:1. After griding, this mixture was rolled into a paper-like sheet with a thickness of 0.3 mm. After drying at 80 ˚C, the sheet was also punched into 1.266 cm^2 circular pieces.

Neutron activation analysis (NAA). NAA is a method of qualitative and quantitative elemental analysis. The principle of this method is to measure the gamma rays that are emitted from the sample, which has been irradiated by neutrons in a nuclear reactor.[s5.1] In this work, NAA was performed to determine the concentrations of V and Zn in the samples

at different discharge and charge states. Each sample was irradiated in the core of the Hoger Onderwijs Reactor (HOR) for about 10 minutes, and then a high-resolution germanium detector was used to collect the gamma spectra.

Electrochemical test. The Zn/VO₂ battery, comprising the prepared electrode, a glass microfiber separator (Whatman) soaked with 1 M ZnSO4 electrolyte, and a Zn foil anode, was assembled in an ambient atmosphere. The assembled batteries were galvanostatically tested between 0.2 and 1.3 V using a MACCOR 4000 battery cycler. Cyclic voltammetry (CV) scanning was measured on a PGSTAT100N electrochemical workstation.

Computational method. Calculations were performed within the density functional theory (DFT) frameworks, as implemented in the Vienna Ab Initio Simulation Package (VASP) with the projector augmented wave (PAW) method due to its ability to accurately represent the lattice constants and the electronic properties. The Perdew-Burke-Ernzerhof (PBE) exchange-correlation function was used with Hubbard U corrections (PBE+U). Effective U value (U_{eff}) of 4.0 eV for vanadium was taken according to the reports. For all the calculations, a 24-atom (8 V atoms and 16 O atoms) supercell representing bulk VO₂, an energy cutoff of 310 eV, and a Γ-centered 3×10×6 k-point grid was employed. Ionic relaxation was performed until a 10^{-5} eV per formula unit difference in energy was obtained.

As shown in **Figure S5.9**, the H ions can potentially be intercalated into 3 different distinct sites, marked A, B, and C in the figure. Previous studies of Li-ion intercalation sites into VO₂ indicated that, when Li-ions are relatively dilute, A sites are most preferable for intercalation due to its perovskite-like cavity, which are the largest tunnels in VO₂ along the b axis.[S5.2] The B sites are introduced, probably because of the Li diffusion from A sites on further lithiation.[S5.2] The B sites are facing the second largest tunnels in VO₂ in the c direction.[2] We have determined that the H intercalation sites are similar to those used for the Li-ion intercalation into VO₂.

The formation energies of the various configurations are calculated according to the end members VO₂ and H₁.₂₅VO₂ using the following formula:

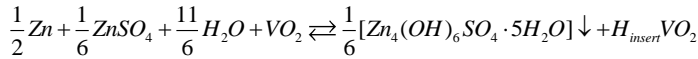$$E_f = E[H_x VO_2] - \frac{x}{1.25} E[H_{1.25} VO_2] - \frac{1.25 - x}{1.25} E[VO_2]$$

Where the E_f reflects the relative stability of each configuration with respect to phase separation into a fraction x of $H_{1.25} VO_2$ and a fraction of $(1.25 - x)$ of VO₂ (B). E is the

energy of a specific arrangement at a concentration x. The formation energies and the corresponding convex hull are exhibited in **Figure 5.5A**.

Based on total energies of the various configurations that fall on the convex-hull, the voltage profile for a VO₂ electrode at 0 K with proton intercalation can be determined by following equation:

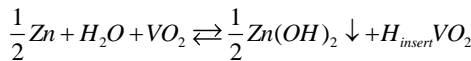$$\overline{V}_{(x_1, x_2)} = -\frac{E[H_{x_2}VO_2] - E[H_{x_1}VO_2] - (x_2 - x_1)E[H]}{(x_2 - x_1)e}$$

Where $\overline{V}(x_1, x_2)$ is the average voltage in the H concentration range of $x_1 \leq x \leq x_2$ and $E[H]$ is the energy of a single H atom, which is calculated from the relaxed H₂ structure. The voltage profile is depicted in **Figure S5.13** (blue line). Here, the simulated potential is versus standard hydrogen electrode, which should be translated towards the Zn/Zn²⁺ potential for comparison with the experiment data, which was referenced versus the Zn metal. This requires evaluation of the overall reaction (equation 8):

$$\frac{1}{2}Zn + \frac{1}{6}ZnSO_4 + \frac{11}{6}H_2O + VO_2 \rightleftarrows \frac{1}{6}[Zn_4(OH)_6SO_4 \cdot 5H_2O]\downarrow + H_{insert}VO_2$$

Here, Zn₄(OH)₆SO₄·5H₂O can be simplified by regarding it as a combination of compounds:

$$[Zn_4(OH)_6SO_4 \cdot 5H_2O] \rightarrow 3Zn(OH)_2 \cdot ZnSO_4 \cdot 5H_2O$$
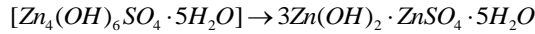
So, the overall reaction can be reduced to:

$$\frac{1}{2}Zn + H_2O + VO_2 \rightleftarrows \frac{1}{2}Zn(OH)_2 \downarrow + H_{insert}VO_2$$

The anodic reaction can be written as (Standard Reduction Potentials):

$$Zn \rightleftarrows Zn^{2+} + 2e^-; E_0 = -0.7618V$$
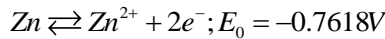
The cathodic reaction can be simplified as:

$$Zn^{2+} + 2OH^- \rightleftarrows Zn(OH)_2; E_0 = -1.246V$$
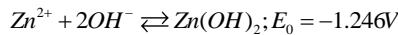
Based on this the calibration voltage between the hydrogen and Zn-metal potentials is:

$$\Delta E_0 = -1.246 - (-0.7618V) = -0.4842V$$

Therefore, the simulated voltage curve for H insertion into VO_2 versus standard hydrogen electrode can be corrected and given versus Zn/Zn^{2+} as:

$$E = E(H_xVO_2) - \Delta E_0 / 2$$

The corrected voltage for H insertion into VO_2 versus the Zn/Zn^{2+} electrode is shown in **Figure S5.13** (red line), which is in good agreement with the experimental discharge voltage curve. We should however notice that the Gibbs energy of $Zn_4(OH)_6SO_4 \cdot 5H_2O$ is most likely smaller capered to the $Zn(OH)_2$ and $ZnSO_4$ constituent compounds, which means the proposed correction voltage curve may be an underestimation.
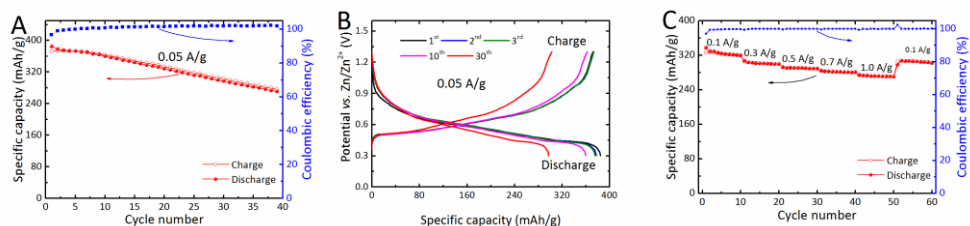
Figure S5.1. Electrochemical properties of Zn/VO$_2$ batteries in a 1M ZnSO$_4$ aqueous electrolyte. (A) Cycling performance and the corresponding coulombic efficiency at a current density of 0.05 A/g within a voltage window of 0.3 – 1.3 V. (B) Selected galvanostatic discharge and charge profiles at the current density of 0.05 A/g. (C) Rate capability performance and the corresponding coulombic efficiencies.
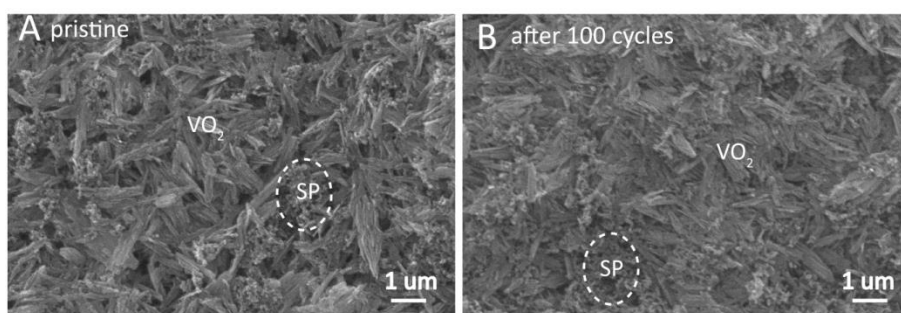
Figure S5.2. Scaning electron microscope (SEM) images of a VO$_2$ cathode surface. SEM images of the VO$_2$ electrode before (A) (prisitne) and after 100 cycles (B) in a battery cycled in a 1 M ZnSO$_4$ aqueous electrolyte at a current density of 1 A/g within a voltage window of 0.2 – 1.3 V.
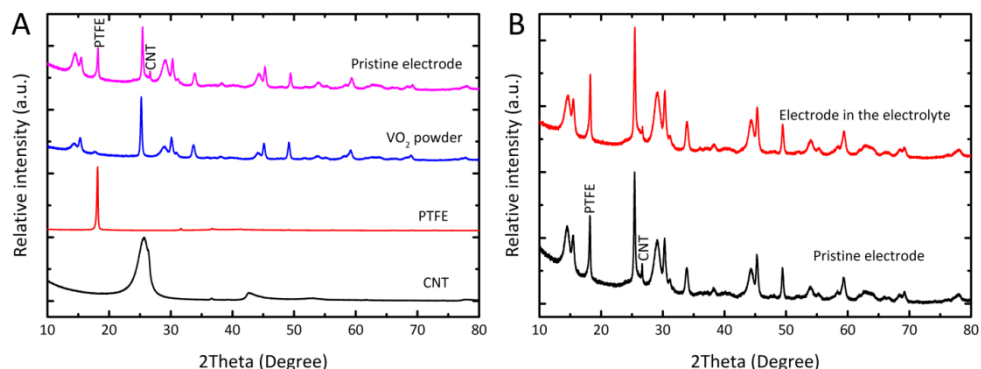
Figure S5.3. XRD patterns of VO$_2$ powder, PTFE binder, CNT, and the VO$_2$ electrode. (A) Comparison between the XRD patterns of CNT, PTFE and VO$_2$ powder. (B) Comparison between the XRD patterns of the pristine VO$_2$ electrode and the VO$_2$ electrode after soaking in 1 M ZnSO$_4$ electrolyte and its subsequent drying.
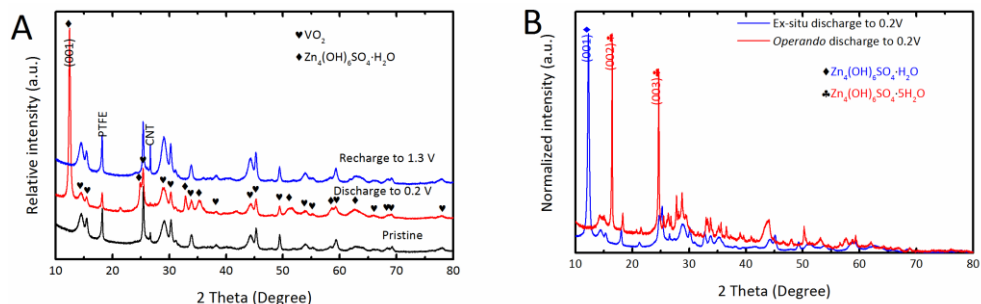
Figure S5.4. (A) Comparison between XRD patterns of discharged, recharged and pristine electrodes. (B) Comparison between XRD patterns from both *ex-situ* and *operando* measurement, each obtained at the end of discharge.
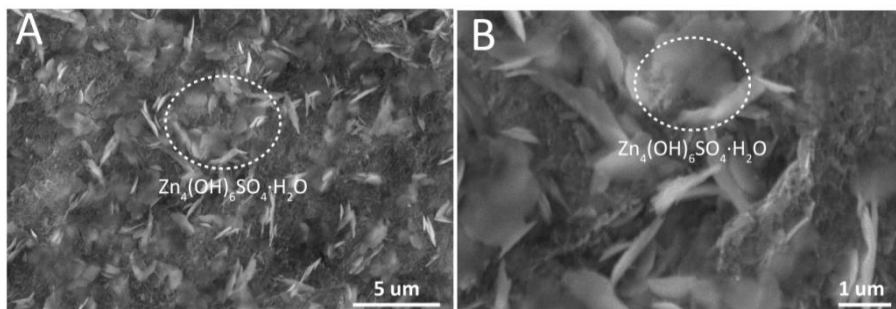
Figure S5.5. Scanning electron microscopy (SEM) images of the VO$_2$ electrode after discharge in a Zn/VO$_2$ battery with a 1 M ZnSO$_4$ electrolyte. The flake-like structure indicates the formation of Zn$_4$(OH)$_6$SO$_4$·H$_2$O crystallites after drying in an vacuum oven at 80 ˚C.
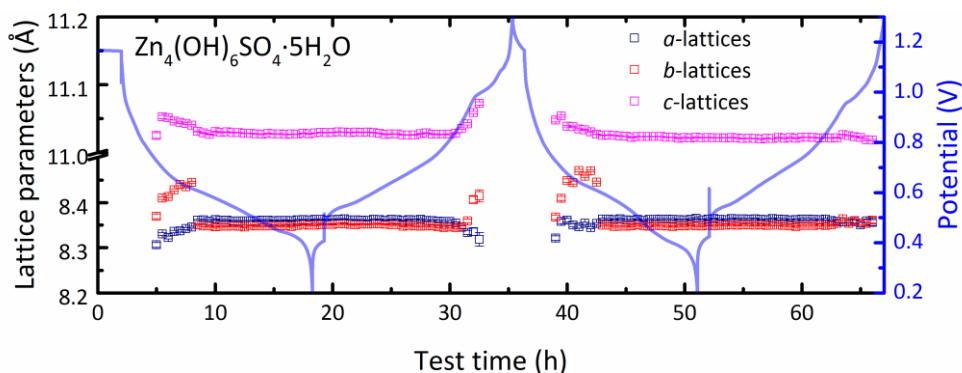
Figure S5.6. The evolution of lattice parameters of the Zn$_4$(OH)$_6$SO$_4$·5H$_2$O phase as a function of discharge/charge time obtained from the sequential Rietveld refinement of the *operando* XRD data (**Figure 2B**).
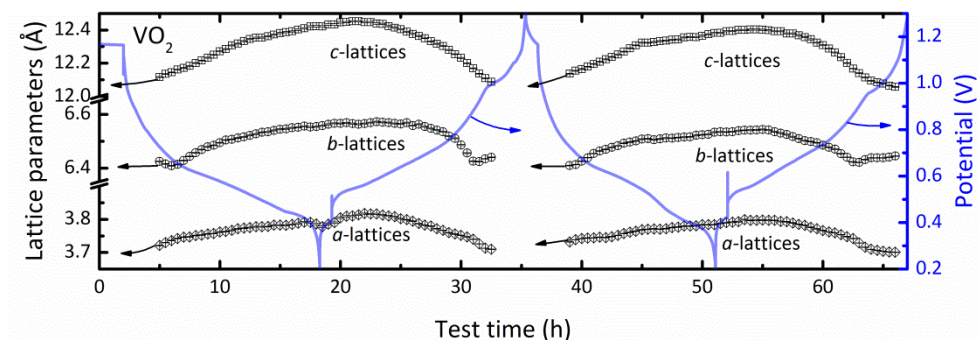
Figure S5.7. The evolution of lattice parameters of the VO$_2$ phase as a function of discharge/charge time obtained from the sequential Rietveld refinement of the *operando* XRD data (**Figure 2B**).
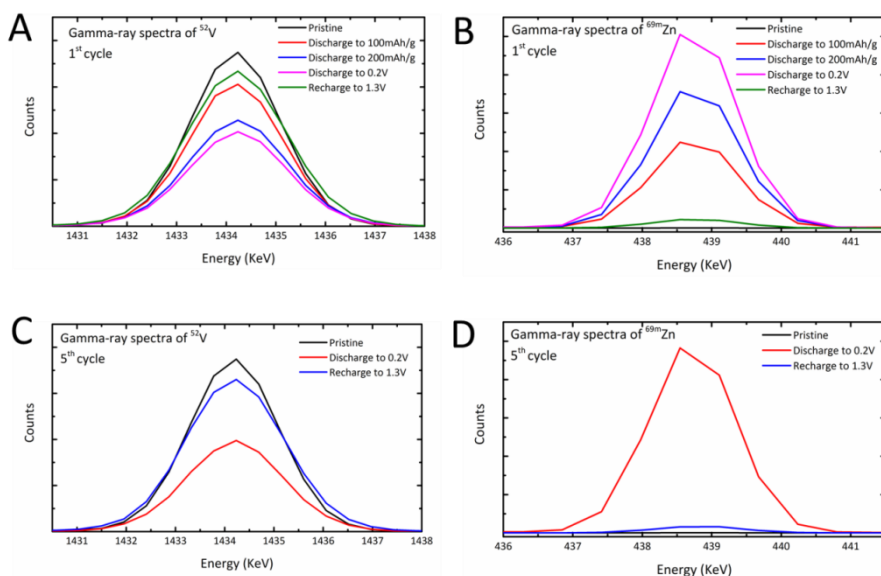
Figure S5.8. Selected regions of the measured Gamma-ray spectra showing the characteristic energies of the [52]V (**A and C**) and [69m]Zn (**B and D**) at 1434.0 KeV and 438.6 KeV, respectively. The counts were normalized by the mass and decay time of the samples. The samples were prepared as an electrode in a battery at different discharge and charge states for the 1st and 5th cycle. Then, the electrode was taken out from the battery and washed with deionized water several times. After, it was dried in the vacuum oven at 80 ˚C overnight before the NAA measurements.
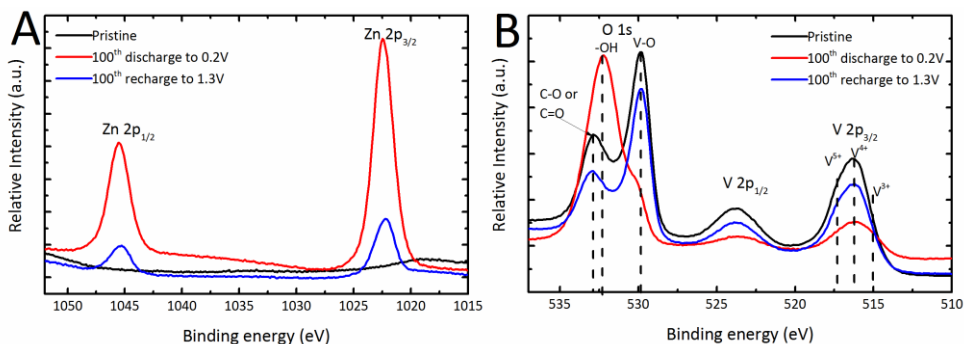
Figure S5.9. X-ray photoelectron spectroscopy (XPS) of the pristine VO₂ electrode, after 100th discharge to 0.2V and 100th recharge to 1.3 V at a current density of 1000 mA/g. (A) Zn 2p region of XPS spectra. (B) O 1s and V 2p region of XPS spectra.
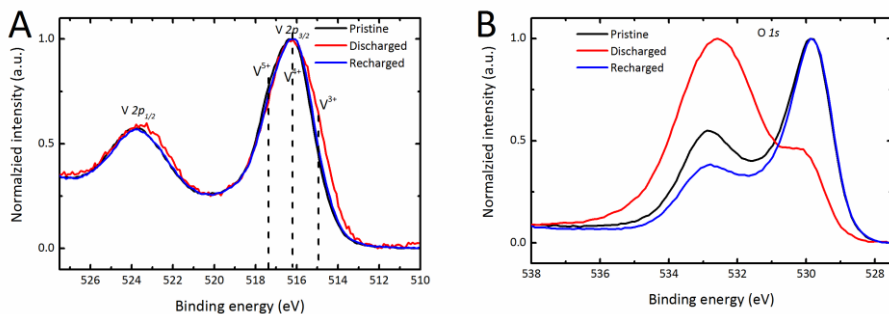
Figure S5.10. Intensity normalized XPS spectra according to **Figure 3B**. (A) Normalized V2p region of the XPS spectra. (B) Normalized O 1s region of the XPS spectra.
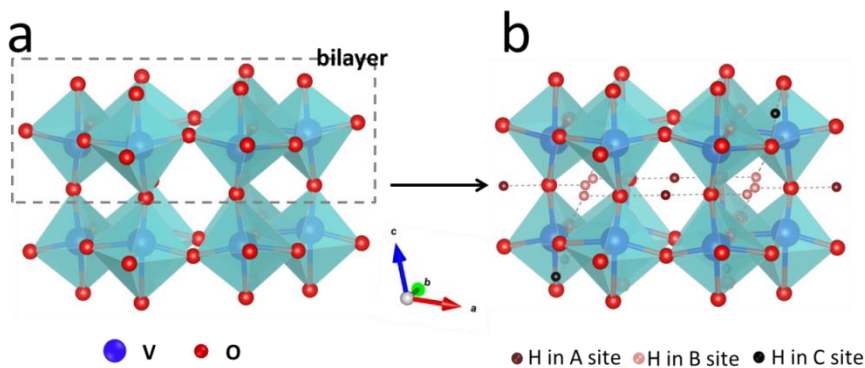
Figure S5.11. (A) Crystal structure of VO₂. (B) Spatial distribution of the possible H intercalation sites.
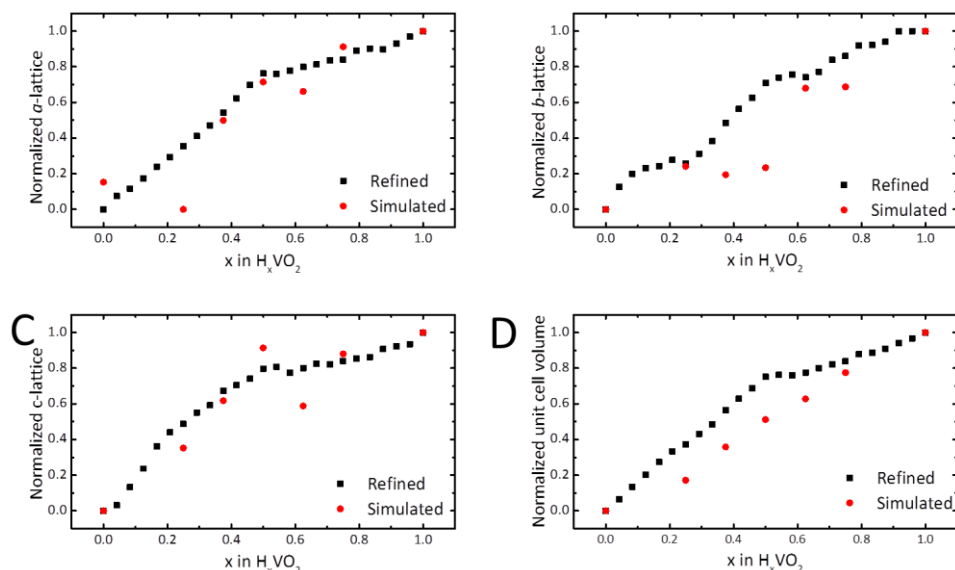
Figure S5.12. Comparison of the normalized lattice parameters and unit cell volume obtained from the refinement of the operando XRD data and those obtained from the first principle results as a function a H^+ concentration x in H_xVO_2.
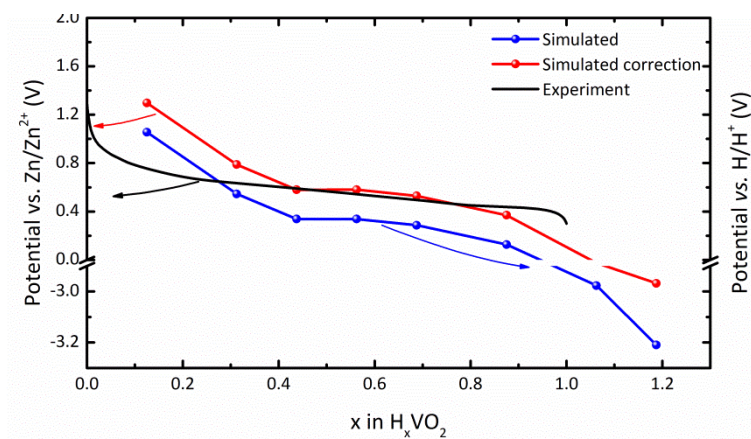
Figure S5.13. Black line represents the experimental voltage curve. Blue line represents the voltage determined for H^+ insertion into VO_2, from the total energies between consecutive points on the convex hull at 0 K, which is simulated from the standard hydrogen electrode. Red line indicates the corrected simulated voltage curve for a Zn/Zn^{2+} electrode.

Table S5.1. Comparison of the V and Zn elemental concentration in the VO_2 electrode between the estimated and NAA measured values at different electrochemical states.

Electrode state	Estimated content		Measured content	
	V (wt.%)	Zn (wt.%)	V (wt.%)	Zn (wt.%)
pristine	~43	0	41.3	0
1st discharge to 100m Ah/g	~36.5	~9.7	36.1	10.1
1st discharge to 200m Ah/g	~30.6	~19.4	27.8	16.4
1st discharge to 0.2V	~25.1	~22.3	24.2	23.1
1st recharge to 1.3V	~43.6	<1	40.1	0.097
5th discharge to 0.2V	~25.3	~20	23.1	22.6
5th recharge to 1.3V	~43	<1	40.4	0.074

Table S5.2. Lattice parameters of the various relaxed H_xVO_2 (0≤ x ≤1) structures obtained from the first-principle analysis.

X in H_xVO2	Lattice parameter (Å)			Unit cell volume($Å^3$)
	a	b	c	
0	12.192	3.773	6.476	289.976
0.25	12.114	3.840	6.570	297.773
0.375	12.369	3.827	6.641	306.265
0.5	12.479	3.838	6.720	313.248
0.625	12.452	3.962	6.633	318.550
0.75	12.580	3.964	6.711	325.235
1	12.625	4.051	6.743	335.463

References

S5.1 Greenberg, R. R.; Bode, P.; De Nadai Fernandes, E. A. *Spectrochim. Acta B* **2011**, *66*, 193.

S5.2 Li, S.; Liu, J.-B.; Wan, Q.; Xu, J.; Liu, B.-X. *Chem. Mater.* **2017**, *29*, 10075.

Summary

Current Li-ion batteries dominate the market but face great challenges with respect to safety, cost and the higher energy and power densit requirements of electrical vehicles and stationary energy storage. Relevant for mobile electrical transport, Li-O$_2$ batteries in theory offer the highest specific energy among all the lithium electrochemical energy storage systems. Research efforts have been made to address the challenges that impede the functioning of this battery, which include low round trip efficiency, low specific capacity and poor cycling stability. To understand the origin of these issues, attaining a deeper understanding of the mechanism behind the electrochemical reactions is of vital importance. This also forms the foundation for exploring ideal oxygen cathodes and better electrolytes. The aqueous zinc batteries are another potential candidate for large scale electric energy storage owing to its low-cost, high operational safety, and environmental benignity. However, it is not easy to find a suitable insertion cathode for ZIBs, because the electrostatic interaction between divalent Zn ions. The development of host materials for ZIBs is still in its infancy, and in-depth understanding of the electrochemical processes involved is paramount at this early stage. The focus of this thesis is on attaining mechanistic insight into the electrochemical processes occurring in working Li-O$_2$ and aqueous zinc batteries, which guides the choice/design of proper electrode materials for these next generation battery systems.

It has been demonstrated that the energy conversion process of Li-O$_2$ batteries is directly determined by the reversible formation and decomposition of discharge products, being either Li$_2$O$_2$ or LiOH. In **Chapter 2**, *operando* X-ray diffraction combined with Rietveld refinement is performed to investigate the structure evolution of Li$_2$O$_2$ and LiOH during the complete discharge/charge process employing a DME and DME/LiI electrolyte, respectively on a carbon cathode. The results show that Li$_2$O$_2$ forms and decomposes reversibly as platelet crystallites with the normal of the platelet in the direction of the *c*-lattice parameter. During discharge, anisotropic Li$_2$O$_2$ crystallites form initially, and more isotropic crystallites are formed as discharge progresses. Li$_2$O$_2$ undergoes decomposition during charge in two stages: first, an amorphous species and small Li$_2$O$_2$ crystallites present are oxidized, and secondly, the larger Li$_2$O$_2$ crystallites undergo decomposition. In the presence of the LiI redox mediator in the DME electrolyte, the product formed on the cathode appears to be LiOH which can be reversibly formed and decomposed over multiple electrochemical cycles. The LiOH forms according to a continuous particle-by-particles nucleation and growth mechanism in the *c*-lattice parameter direction, which is deduce from the evolution of the average LiOH crystallite size and shape during discharge.

On the basis of DFT calculation, the OH vacancies in LiOH are suggested to be formed as a consequence of the depletion of water in DME electrolyte. The decomposition of LiOH during charge is proposed to start with the smallest OH deficient LiOH crystallites, indicating that the decomposition of these particles is most facile. The analysis of the structural evolution of Li_2O_2 and LiOH in this chapter provides key information for understanding and improving the highly relevant $Li-O_2$ battery system, e.g. it is easier to decompose smaller size Li_2O_2 particle on charge, suggesting a catalyst may use to promote the formation of smaller size Li_2O_2 particle on discharge.

Understanding the Li_2O_2 formation and decomposition mechanism in the $Li-O_2$ battery during the electrochemical process, guides the choice of a surface catalyst on the cathode to control the size and morphology of Li_2O_2 crystals. In **Chapter 3**, the use of hexagonal NiO nano seed crystallites added to the active carbon cathode in $Li-O_2$ battery is presented, and the *operando* XRD result demonstrates the *equiaxed* growth of Li_2O_2 on the NiO nanoparticles. The electron microscopy energy-dispersive X-ray spectroscopy (SEM-EDX) elemental map also confirms the preferential formation of Li_2O_2 on the NiO surface. Furthermore, the first principle calculations predict a low interfacial energy for the $NiO-Li_2O_2$ interfaces. Unfortunately, the poor electrochemical performance of the battery appears to be a consequence of electrolyte side reaction and the cathode structure design, whereas it is known that a more porous cathode will facilitate faster and stable growth/decomposition of Li_2O_2. As a result, instead of bulk activated carbon, a carbon nanotube interpenetrating porous network structure, is presented in **Chapter 4** as a cathode, together with another seed crystal (nano-sized $\alpha-Fe_2O_3$) achieving excellent cycling stability on deep discharge/charge with high capacity retention. The initial capacity of Fe_2O_3/CNT electrode is 805 mAh/g (0.70 mAh/cm^2) at 0.2 mA/cm^2, while maintaining a capacity of 1098 mAh/g (0.95 mAh/cm^2) after 50 cycles. Owing to similar *d*-spacing of the *(100)* Li_2O_2 and *(104)* Fe_2O_3 planes, the Li_2O_2 crystallite is induced to *epitaxially* nucleate on the Fe_2O_3 surface resulting in larger Li_2O_2 primary crystallites and smaller secondary particles. Mechanistic insights into dual-functional materials that act both as stable host substrates and promote redox reactions in $Li-O_2$ batteries represent new opportunities for controlling the discharge product morphology, leading to high cycling stability and Coulombic efficiency.

The electrochemical reaction in rechargeable aqueous ZIBs depends to a large extent on the combination of electrodes and electrolytes used. Recently, vanadium oxides have been reported as promising Zn-ion host material, however, pending issues are potential proton co-insertion, sluggish Zn-ion transport and large structural changes upon Zn-ion insertion. In **Chapter 5**, a Zn/VO_2 aqueous battery using $ZnSO_4$ electrolyte was

investigated to understand the energy conversion mechanism. The *operando* XRD results confirmed the reversible formation and decomposition of $Zn_4(OH)_6SO_4 \cdot 5H_2O$ surface product on the cathode during discharge and charge, respectively. However, an extra H^+ is concurrently produced from the H_2O splitting reaction as the $Zn_4(OH)_6SO_4 \cdot 5H_2O$ formed during discharge. To achieve charge neutrality, H^+ is proposed to be inserted/extracted in/from the VO_2 lattice during discharge/charge, and this is corroborated experimentally and from first-principle simulations. The minimal structural changes induced by H^+ insertion into VO_2 are supposed to favour a long cycle life of these aqueous Zn/VO_2 batteries. The kinetics on discharge are, initially determined by the $Zn_4(OH)_6SO_4 \cdot 5H_2O$ deposition, and later by the proton insertion into VO_2, both of which are relatively fast, explaining the excellent rate performance of the present aqueous Zn/VO_2 batteries. These findings imply a competition between H^+ and Zn-ion insertion, determined by the stability of the deposited compound as well as the H^+/Zn-ion inserted vanadium dioxide, tailoring of which is brought forward as a promising strategy for ZIBs.

In summary, this thesis explores the basic electrochemical reaction mechanisms in next generation batteries namely the $Li-O_2$ and the aqueous zinc batteries. By using *operando* techniques, the structural evolution at the electrode (the structure change of the crystallites or the formation/decomposition of the surface products) in the batteries is monitored and analysed. With this information in combination with measured electrochemical data and first principle simulations, the reaction mechanism is deduced. From these fundamental findings, electrode and material design strategies were developed aiming to contribute to the understanding and development of next generation batteries.

Samenvatting

De hedendaagse Li-ion-accu's domineren de markt, maar staan voor grote uitdagingen met betrekking tot veiligheid, kosten en de hogere energie- en vermogensdichtheidsvereisten van elektrische voertuigen en stationaire energieopslag. Relevant voor mobiel elektrisch vervoer, bieden Li-O_2 batterijen in theorie de hoogste specifieke energie onder alle elektrochemische energieopslagsystemen met gebruik van lithium. Er zijn onderzoeksinspanningen gedaan om de uitdagingen op te pakken die de werking van deze batterij belemmeren, waaronder een lage efficiëntie van de ladingscyclus, een lage specifieke capaciteit en een slechte stabiliteit onder cycli. Om de oorsprong van deze problemen te begrijpen, is het van vitaal belang een beter begrip te krijgen van het mechanisme achter de elektrochemische reacties. Dit vormt ook de basis voor het verkennen van ideale zuurstofkathodes en betere elektrolyten. De waterige zinkbatterijen zijn een andere potentiële kandidaat voor grootschalige opslag van elektrische energie vanwege de lage kosten, hoge operationele veiligheid en milieuvriendelijkheid. Het is echter niet eenvoudig om een geschikte insertiekathode voor ZIB's te vinden vanwege de elektrostatische interactie tussen tweewaardige Zn-ionen. De ontwikkeling van gastheermaterialen voor ZIB's staat nog in de kinderschoenen en een diepgaand inzicht in de betrokken elektrochemische processen is in dit vroege stadium van het grootste belang. De focus van dit proefschrift ligt op het verkrijgen van mechanistisch inzicht in de elektrochemische processen die optreden in werkende Li-O_2 en waterige zinkbatterijen, dat leidend is in de keuze / ontwerp van de juiste elektrodematerialen voor deze batterijsystemen van de volgende generatie.

Er is aangetoond dat het energieconversieproces van Li-O_2 batterijen direct wordt bepaald door de reversibele vorming en afbraak van ontladingsproducten, hetzij Li_2O_2 dan wel LiOH. In **Hoofdstuk 2** wordt *in operando* röntgenverstrooiing gecombineerd met Rietveld-verfijning uitgevoerd om de evolutie van de structuur van Li_2O_2 en LiOH te onderzoeken tijdens het volledige ontladings- / ladingsproces met behulp van een DME en DME / LiI elektrolyt, respectievelijk op een koolstofkathode. De resultaten laten zien dat Li_2O_2 reversibel vormt en uiteenvalt als kristallieten in de vorm van plaatjes met de normaal van het plaatje in de richting van de c-roosterparameter. Tijdens de ontlading worden aanvankelijk plaatvormige Li_2O_2-kristallieten gevormd en worden meer bolvormige kristallieten gevormd naarmate de ontlading vordert. Li_2O_2 ontleedt tijdens lading in twee fasen: eerst worden een amorfe species en aanwezige kleine Li_2O_2-kristallieten geoxideerd en later ontleden de grotere Li_2O_2-kristallieten. In aanwezigheid van de LiI-redox-mediator in de DME-elektrolyt lijkt het op de kathode gevormde product

LiOH te zijn dat reversibel kan worden gevormd en uiteen kan vallen over meerdere elektrochemische cycli. Het LiOH vormt volgens een doorlopend deeltje-per-deeltje nucleatie en groeimechanisme in de c-roosterparameterrichting, wat af te leiden is uit de evolutie van de gemiddelde LiOH-kristallietgrootte en vorm tijdens ontlading. Op basis van DFT-berekening wordt gesuggereerd dat de OH-vacatures in LiOH worden gevormd als gevolg van de uitputting van water in de DME-elektrolyt. Voor de ontleding van LiOH tijdens lading wordt voorgesteld, dat die begint met de kleinste OH-deficiënte LiOH-kristallieten, wat aangeeft dat de ontleding van deze deeltjes het gemakkelijkst is. De analyse van de structurele evolutie van Li_2O_2 en LiOH in dit hoofdstuk biedt belangrijke informatie voor het begrijpen en verbeteren van het uiterst relevante $Li-O_2$-batterijsysteem, d.w.z. het is gemakkelijker om Li_2O_2-partikels met kleinere afmetingen te ontleden bij lading, wat suggereert dat een katalysator kan worden gebruikt om de vorming van Li_2O_2-deeltjes met kleinere afmetingen bij ontlading te bevorderen.

Inzicht in het Li_2O_2-formatie- en decompositiemechanisme in de $Li-O_2$-batterij tijdens het elektrochemische proces, stuurt de keuze van een oppervlaktekatalysator op de kathode om de grootte en morfologie van Li_2O_2-kristallen te regelen. In **Hoofdstuk 3** wordt het gebruik van hexagonale NiO-nanokristallieten die aan de actieve koolstofkathode in de $Li-O_2$-batterij worden toegevoegd, gepresenteerd en het *in operando* XRD-resultaat toont de gelijkassige groei van Li_2O_2 op de NiO-nanodeeltjes aan. De met elektronenmicroscopische energie-dispersieve röntgenspectroscopie (SEM-EDX) bepaalde kaart van de elementen bevestigt ook de preferentiële vorming van Li_2O_2 op het NiO-oppervlak. Bovendien voorspellen de *ab initio* berekeningen een lage grensvlakenergie voor de $NiO-Li_2O_2$-grensvlakken. Helaas lijkt de slechte elektrochemische prestatie van de batterij een gevolg te zijn van een elektrolyt-nevenreactie en het ontwerp van de kathodestructuur, terwijl het bekend is dat een meer poreuze kathode een snellere en stabiele groei / ontlending van Li_2O_2 zal vergemakkelijken. Dientengevolge wordt in **Hoofdstuk 4** in plaats van massieve actieve kool een poreuze netwerkstructuur van elkaar doordringende koolstofnanobuizen als kathode gepresenteerd, samen met een ander entkristal (α-Fe_2O_3 op nanogrootte), die uitstekende stabiliteit onder cycli bereikt bij diepe ontlading / lading met hoge capaciteitretentie. De initiële capaciteit van de Fe_2O_3 / CNT-elektrode is 805 mAh / g (0,70 mAh / cm^2) bij 0,2 mA / cm^2, terwijl een capaciteit van 1098 mAh / g (0,95 mAh / cm^2) na 50 cycli wordt behouden. Vanwege een vergelijkbare d-afstand tussen de (100) Li_2O_2- en (104) Fe_2O_3-vlakken wordt het Li_2O_2-kristalliet geïnduceerd epitaxiaal te nucleëren op het Fe_2O_3-oppervlak, wat resulteert in grotere primaire Li_2O_2-kristallieten en kleinere secundaire deeltjes. Mechanistische inzichten in bifunctionele materialen die zowel als stabiele gastheersubstraten werken als

redoxreacties in Li-O$_2$-batterijen bevorderen, bieden nieuwe mogelijkheden tot het beheersen van de morfologie van het ontladingsproduct, wat leidt tot hoge stabiliteit onder cycli en Coulomb-efficiëntie.

De elektrochemische reactie in oplaadbare waterige ZIB's hangt in hoge mate af van de combinatie van gebruikte elektroden en elektrolyten. Er zijn recente berichten over vanadiumoxides als veelbelovende Zn-ionen gastheermaterialen, maar open punten zijn potentiële proton co-insertie, traag Zn-ionentransport en grote structuurveranderingen na Zn-ioneninsertie. In **Hoofdstuk 5** werd een Zn / VO$_2$ waterige batterij met ZnSO$_4$-elektrolyt onderzocht om het mechanisme van de energieomzetting te begrijpen. De *in operando* XRD-resultaten bevestigden de reversibele vorming en afbraak van het Zn$_4$(OH)$_6$SO$_4$·5H$_2$O-oppervlakteproduct op de kathode tijdens respectievelijk ontlading en lading. Een extra H$^+$ wordt echter gelijktijdig geproduceerd met de H$_2$O-splitsingsreactie als Zn$_4$(OH)$_6$SO$_4$·5H$_2$O wordt gevormd tijdens ontlading. Om ladingsneutraliteit te bereiken, wordt voorgesteld dat H$^+$ wordt opgenomen / geëxtraheerd in/uit het VO$_2$-rooster tijdens ontlading / lading, en dit wordt experimenteel en door *ab initio* simulaties bevestigd. De minimale structuurveranderingen geïnduceerd door H$^+$ insertie in VO$_2$ zouden een lange levensduur van deze waterige Zn/VO$_2$-batterijen moeten bevorderen. De kinetica bij ontlading wordt aanvankelijk bepaald door de afzetting van Zn$_4$(OH)$_6$SO$_4$·5H$_2$O en vervolgens door de insertie van het proton in VO$_2$, die beide relatief snel zijn, hetgeen de uitstekende prestaties van de huidige waterige Zn/VO$_2$-batterijen verklaart. Deze bevindingen impliceren een competitie tussen H$^+$ en Zn-ion insertie, bepaald door de stabiliteit van de gedeponeerde verbinding en het vanadium dioxide met de H$^+$ / Zn-ionen, het aanpassen waarvan naar voren wordt gebracht als een veelbelovende strategie voor ZIB's.

Samenvattend verkent dit proefschrift de fundamentele elektrochemische reactiemechanismen in batterijen van de volgende generatie, namelijk de Li-O$_2$ en de waterige zinkbatterijen. Door *in operando*-technieken te gebruiken, wordt de structuurevolutie van de elektrode (de structuurverandering van de kristallieten of de vorming / afbraak van de oppervlakteproducten) in de batterijen gecontroleerd en geanalyseerd. Uit deze informatie in combinatie met gemeten elektrochemische gegevens en *ab initio* simulaties wordt het reactiemechanisme afgeleid. Uit deze fundamentele bevindingen zijn ontwerpstrategieën voor elektroden en materialen ontwikkeld met het doel bij te dragen tot het begrip en de ontwikkeling van batterijen van de volgende generatie.

Acknowledgements

In the end, I would like to take the opportunity to express my sincere appreciation to those who have contributed to this thesis and supported me in one way or the other during my PhD journey in the Netherlands.

First and foremost, I would like to thank my supervisor/promotor, Prof. Marnix Wagemaker and my daily supervisor, Dr. Swapna Ganapathy, who performs more than a mentor in my development career and life. Thanks for your constant encouragement and guidance tracking on my PhD journey, which moves forward me in doing research independent. Without your coherent and illuminating instruction, this thesis would not have reached its present form. I greatly appreciate your kindness and friendliness in my daily life. I am also indebted to my co-promotor Prof. Fokko Mulder for revising this thesis and helpful suggestions for my work. Your generosity has been one of the valuable contributions for this thesis.

I am also grateful to my Chinese supervisor Prof. Quanyao Zhu and Prof. Wen Chen from the Wuhan University of Technology. They inspired me on the way of my scientific research. Without their support I couldn't get the opportunity to start my PhD journey in the Delft University of Technology (TUD), which is a big turning point in my life. Big thanks once again go to all of my supervisors for your contributions, and I feel so lucky to meet all of you in my life.

Next, I would like to acknowledge the assistance of Jouke Heringa, Frans Ooms, Michel Steenvoorden, Kees Goubitz and the Demo group for their strong technical support in general lab facilities. Jouk is acknowledged for his kind help with many issues (the starting preparation in the group, software, and Dutch translation) in my research and life. Frans, Michel and Kees give me training, help me solve variety problems in the laboratory and assistant me design the experiment in the thesis. I also wish to thank the secretaries, Ilse van der Kraaij and Nicole Banga, who are always friendly to me and helpful with my administrative issues.

Very special thanks to Xuefei Miao and Yue Xiao, who introduce me to my supervisor Marnix. A Heartfelt thanks to my supportive wonderful friends Swapna Ganapathy, Xiaoyu Zhang, Yaolin Xu, Zhou Zhou, Ming Ma, Shasha Lv, Haixing Fang and Beien Wang, who company with me, trust me and inspire me in my PhD life. You have always been there whenever I meet the troubles. I still remember that it was you, Swapna receipted me and introduced everyone to me for the first time I came to the office. And then, I live through

my PhD period under your guidance. I also will never forget that, Haixing, you took me in your apartment when I landed in the Netherlands and got trouble with my rent room. Shasha, we always worked overtime together. Xiaoyu, Yaolin and Zhou, thanks for your trust, everlasting friendship and strong support in my life.

I extend my sincere thanks to all members of the Storage of Electrochemical Energy (SEE), Fundamental Aspects of Materials (FAME) and Neutron Positron Methods for Materials (NPM2) faculties in TUD who are great persons to work with and also nice friends in life. There are many names I would like to mention with great pleasure: Alexandros, Bei, Bo, Bowei, Carlo, Chandra, Chao, Chenglong, Chuang, Ekks, Erik, Elveline, Fengjiao, Fengqi, Guorei, Jiawei, Jun, Lambert, Kun, Martijn, Michael, Ming, Niek, Niels, Peter Paul, Qidi, Remco, Shiv, Swapna, Tiantian, Tomas, Violetta, Wenqin, Xinmin, Yifan, Zhimin, Zhou, Zhu and many more. I also owe thanks to some friends, Yamin, Linyin, Yang and Wen, who spend time together to visit the landscape and get use to the life in the Netherlands.

I still remember the happy cycling time after work with you, Niek and Tomas, especially the memorable cycling journey of our team (Niek, Tomas, Martijn, and Peter-Paul) to Belgium. Another unforgettable thing is the barbecue group activity in SEE group which along with us during the whole summer every year. Thanks for all of you make my life pleasant outside the PhD work.

I would also like to thank people in LeydenJar B.V., Christian Rood, Arjen Didden, and Gabriel de Scheemaker, who teach me how to work and communicate in a company and link my research field to the realistic application of batteries. Thanks to the group members, Frans Ooms, Klaus Brandt, Marinaro Mario, Soppe Wim, Loffler Jochen, and Carly Wantzing for sharing your knowledge, which help me to gain a deep understanding of batteries in industry field.

Last but not the least, I would like to deeply thank my family for their warm caring and selfless love. I am greatly indebted to my beloved parents, brother, and my wife (Dan Luo).

List of Publications

Publications related to this thesis

1. **Z. Li**, S. Ganapathy, Y. Xu, Z. Zhou, M. Sarilar, M. Wagemaker, *Mechanistic Insight into the Electrochemical Performance of Zn/VO$_2$ Batteries with an Aqueous ZnSO$_4$ Electrolyte, **Advanced Energy Materials,** 2019, 9, 1900237.*

2. **Z. Li,** S. Ganapathy, Y. Xu, Q. Zhu, W. Chen, I. Kochetkov, C. George, L.F. Nazar, M. Wagemaker, *Fe$_2$O$_3$ Nanoparticle Seed Catalysts Enhance Cyclability on Deep (Dis)charge in Aprotic Li-O$_2$ Batteries, **Advanced Energy Materials,** 2018, 8, 1703513.*

3. S. Ganapathy, **Z. Li,** M. S. Anastasaki, S. Basak, X.-F. Miao, K. Goubitz, H. W. Zandbergen, F.M. Mulder, M. Wagemaker, *Use of Nano Seed Crystals To Control Peroxide Morphology in a Nonaqueous Li–O$_2$ Battery.* **The Journal of Physical Chemistry C,** 2016, 120, 18421-18427.

4. **Z. Li,** S. Ganapathy, Y. Xu, J. R. Heringa, Q. Zhu, W. Chen, , M. Wagemaker, *Understanding the Electrochemical Formation and Decomposition of Li$_2$O$_2$ and LiOH with Operando X-ray Diffraction*, **Chemistry of Materials** 2017, 29, (4), 1577-1586.

Other Publications

5. S. Lv, T. Verhallen, A. Vasileiadis, F. Ooms, Y. Xu, **Z. Li**, Z. Li, M. Wagemaker, *Operando Monitoring the Lithium Spatial Distribution of Lithium Metal Anodes, **Nature Communications,** 2018, 9, 2152.*

6. C. Yu, S. Ganapathy, E.R. van Eck, H. Wang, S. Basak, **Z. Li**, M. Wagemaker, *Accessing the Bottleneck in All-Solid State Batteries, Lithium-ion Transport over the Solid-Electrolyte-Electrode Interface, **Nature Communications,** 2017, 8, 1086.*

7. S. Ganapathy, J.R. Heringa, M.S. Anastasaki, B.D. Adams, M. van Hulzen, S. Basak, **Z. Li**, J.P. Wright, L.F. Nazar, N.H. van Dijk, M. Wagemaker, *Operando Nanobeam Diffraction to Follow the Decomposition of Individual Li$_2$O$_2$ Grains in a Nonaqueous Li–O$_2$ Battery, **The Journal of Physical Chemistry Letters,** 2016, 7, 3388-3394.*

8. **Z. Li,** Q. Zhu, S. Huang, S. Jiang, S. Lu, W. Chen, G.S. Zakharova, *Interpenetrating Network V$_2$O$_5$ Nanosheets/Carbon Nanotubes Nanocomposite for Fast Lithium Storage, **RSC Advances,** 2014; 4(87): 46624-46630.*

9. **Z. Li,** H. Sun, J. Xu, Q. Zhu, W. Chen, G.S. Zakharova. *The Synthesis, Characterization and Electrochemical Properties of $V_3O_7·H_2O$/CNT Nanocomposite,* **Solid State Ionics,** **2014. 262:30–34.**

10. J. Xu, H. Sun, **Z. Li,** S. Lu, X. Zhang, S. Jiang, Q. Zhu, G.S. Zakharova, *Synthesis and Electrochemical Properties of Graphene/V_2O_5 Xerogels Nanocomposites as Supercapacitor Electrodes,* **Solid State Ionics,** **2014, 262: 234-237.**

11. S. Jiang, **Z. Li**, S. Huang, S. Lu, Y. Yu, G. Mou, J. Xu, Q. Zhu, X. Tan, X. Zhu, G.S. Zakharova, *Synthesis and Electrochromic Characterization of the Graphene/Poly (ethylene oxide)/$V_2O_5·nH_2O$ Ternary Nanocomposite Films,* **Journal of The Electrochemical Society,** **2014, 161(10): H684-H688.**

12. **Z. Li**, X. Zhang, J. Xu, S. Huang, Q. Zhu, W. Chen, G.S. Zakharova, *Carbon Nanotube-Induced Formation of Vanadium Oxide Nanorods and Nanotubes,* **Journal of Materials Research,** **2013, 28(04):627-634.**

13. Q. Zhu, Z. Li, S. Huang, X. Zhang, W. Chen, G.S. Zakharova, *Research on the Electrochemical Performance of Nanocomposites of Vanadium Oxide and Carbon Nanotubes as Cathode materials,* **Electrochimica Acta,** **2012, 81: 25–30.**

Curriculum Vitae

Zhaolong Li was born on 23 March 1988 in Hubei, China. He got his Bachelor's degree in Material Science and Engineering at Wuhan Institute of Technology by June 2010. After, he moved to Wuhan University of Technology to pursue his Master of Engineering degree majored in Composite Materials and graduated in June, 2013.

In 2013, he started a PhD study at Wuhan University of Technology, after which in 2014 he obtained a China Scholarship Council (CSC) scholarship, and moved his PhD study in the group of Storage of Electrochemical Energy (SEE) at Delft University of Technology. Under the supervised and financial supported by Prof. Dr. Ir. Marnix Wagemaker, he worked his PhD project on understanding the electrochemical reaction mechanism of next generation battery systems. Meanwhile, he also works as an employee in LeydenJar B.V. to explore the commercialized application of Si anode in Li-ion batteries from May 2018 until now.